

**LEARNING BASED CONTROL COMPENSATION
FOR MULTI-AXIS GIMBAL SYSTEMS USING
INVERSE AND FORWARD DYNAMICS**

A THESIS SUBMITTED TO
THE GRADUATE SCHOOL OF ENGINEERING AND SCIENCE
OF BILKENT UNIVERSITY
IN PARTIAL FULFILLMENT OF THE REQUIREMENTS
FOR
THE DEGREE OF
MASTER OF SCIENCE
IN
MECHANICAL ENGINEERING

By

Damla Leblebicioğlu

September 2021

LEARNING BASED CONTROL COMPENSATION FOR MULTI-AXIS
GIMBAL SYSTEMS USING INVERSE AND FORWARD DYNAMICS

By Damla Leblebiciođlu

September 2021

We certify that we have read this thesis and that in our opinion it is fully adequate,
in scope and in quality, as a thesis for the degree of Master of Science.

Melih akmakcı (Advisor)

Özgür Ateşođlu (Co-Advisor)

Omer Morgöl

Halit Ergezer

Approved for the Graduate School of Engineering and Science:

 Ezhan Karaşan

Director of the Graduate School

ABSTRACT

LEARNING BASED CONTROL COMPENSATION FOR MULTI-AXIS GIMBAL USING INVERSE AND FORWARD GIMBAL DYNAMICS

Damla Leblebiciođlu

M.S in Mechanical Engineering

Advisor(s): Melih akmakcı, zgür Ateőođlu

September 2021

Unmanned aerospace vehicles (such as rockets, drones, and satellites) usually carry sensors as their primary payload. These sensors (i.e., electro-optical and/or infrared imaging cameras) are used for image processing, target tracking, surveillance, mapping, and providing high-resolution imagery for environmental surveys. It is crucial to obtain a steady image in all of those applications. This is typically accomplished by using multi-axis gimbal systems.

This study concentrates on the modeling and control of a multi-axis gimbal system that will be mounted on a surface-to-surface tactical missile. A novel and fully detailed procedure is proposed to derive the nonlinear and highly coupled EOMs (Equations of Motion) of the two-axis gimbal system. Different from the existing works, *Forward Dynamics* of the two-axis gimbal system is modeled using multi-body dynamics modeling techniques. In addition to *Forward Dynamics* model,

Inverse Dynamics model is generated to estimate the complementary torques associated with the state and mechanism-dependent, complex disturbances acting on the system. *Forward* and *Inverse Dynamics* models are used in *Monte Carlo Simulations (MCSs)* for *Sensitivity Analysis*. A multilayer perceptron (MLP) structure based disturbance compensator is implemented to cope with external and internal disturbances and parameter uncertainties through torque input channel. Comparisons with well known controllers such as cascaded PID, ADRC (Active Disturbance Rejection Control), Inverse Dynamics based controllers show that the NN (neural network)-based controller is more successful in the full operational range without requiring any tuning or adjustment.

Implementation of MLP assisted closed-loop control with simulations using Simulink® are performed. Finally, proposed control algorithms are tested on the physical system by using Simulink® Real-Time (xPC Target). Comparative results are presented in figures and tables in the thesis.

Keywords: multi-axis gimbal system, real-time control, neural network, multi-body dynamics modeling, ADRC, inverse dynamics, disturbance torque compensation, Monte Carlo simulations

ÖZET

ÇOK EKSENLİ GİMBAL SİSTEMLERİ İÇİN İLERİ VE GERİ DİNAMİKLERİ KULLANAN ÖĞRENME TABANLI KONTROL DENGELEYİCİSİ

Damla Leblebicioğlu

Makine Mühendisliği, Yüksek Lisans

Tez Danışmanları: Melih Çakmakcı, Özgür Ateşoğlu

Eylül 2021

İnsansız hava araçlarının (örnek olarak roketler, dronlar ve uydular) genellikle temel yükleri çeşitli alıcılardır. Bu alıcılar (elektro-optik ve/veya kızılötesi görüntüleme kameraları) görüntü işleme, hedef takibi, gözetleme, haritalama ve yüksek çözünürlüğe sahip çevresel görüntüleme gibi çalışmalar için kullanılır. Bu uygulamalarda, oynamayan bir görüntü elde etmek (ki bu da çok eksenli gimbal sistemleri ile başarılabilir) çok önemlidir. Çok eksenli gimbal sistemleri, kameranın görüş hattı vektörünün, istenilen hedef veya noktayı takip ederken kararlı ve sabit olmasını garantiler.

Bu çalışma, karadan karaya atılan taktik bir füzeye takılacak olan çok eksenli bir gimbal sisteminin modelleme ve kontrolü üzerine odaklanmıştır. Öncelikle, çok eksenli gimbal sisteminin doğrusal olmayan ve çok detaylı denklemlere sahip, özgün bir matematiksel modeli elde edilmiştir. Önceki yapılan çalışmalardan farklı olarak,

çoklu cisim dinamiği yöntemleri ile çok eksenli gimbal sisteminin *İleri Dinamik* modeli çıkartılmıştır. *İleri Dinamik* modeline ek olarak, sisteme etki eden, durum ve mekanizmayla bağlantılı, karmaşık bozunum momentlerini tahmin edebilmek için *Ters Dinamik* model elde edilmiştir. Daha sonra, *İleri* ve *Geri Dinamik* modeller *Monte Carlo benzetimlerinde* kullanılarak *Duyarlılık Analizi* yapılmıştır.

Dış ve iç bozunumları, model belirsizliklerini moment yoluyla telafi edebilmek için çok katmanlı bir yapay sinir ağı yapısı önerilmiştir. Çok katmanlı PID, ADRC, *Geri Dinamik* tabanlı kontrolcüler ile yapılan karşılaştırmalar, önerilen yapay sinir ağı tabanlı yapının tüm çalışma bölgesi içerisinde herhangi bir düzeltme ya da ayarlama gerektirmeden daha başarılı olduğunu göstermiştir.

Çok katmanlı yapay sinir ağı yapısına dayalı, kapalı döngü benzetimler, Simulink® yazılımı ile gerçekleştirilmiştir. Son olarak, önerilen kontrol algoritmaları Simulink® Real-Time (xPC Target) kullanılarak fiziksel sistem üzerinde denenmiştir. Karşılaştırmalı sonuçlar, tablo ve grafikler ile tezde verilmiştir.

Anahtar Kelimeler: Çok eksenli gimbal sistemi, gerçek zamanlı kontrol, yapay sinir ağı, çoklu cisim dinamiği, ADRC, geri dinamik, bozunum momenti telafisi, Monte Carlo benzetimleri

*I dedicate this thesis to my dear mother and father, Ayşe and Kemal.
Without them, none of these achievements could have been possible.*

ACKNOWLEDGMENTS

I would like to express my deepest gratitude to my supervisor Assist. Prof. Dr. Melih akmaccı and co-supervisor Dr. zgr Ateřođlu for their guidance, advice, criticism, encouragements and insight throughout the research. It has been such a great experience for me to work with them. I would also like to thank, Prof. Dr. mer Morgl and Assist. Prof. Dr. Halit Ergezer for their comments in the defense jury.

I would like to thank to my company, ROKETSAN Missiles Inc., for giving me a chance to work on this project and to perform my real-time experiments with the physical set-up.

I sincerely appreciate Bilkent University, Mechanical Engineering Department for the education I received.

The biggest thanks go to my colleague, Anıl Erdem Derinz for his endless and precious support that motivates me at every stage of this work. He always answered my questions kindly and helped me to understand the concepts related with multi-axis gimbal systems and mechanical design of seekers. I am extremely lucky to have met and worked with someone like him. He taught me to believe in myself and to question what other people are trying to impose on me. Anıl made me a better engineer and I will be always grateful to him for that.

My colleagues and friends, Meltem Dirim Turan, Sinan Arda, Arda Karabey, İtir Aylı and İpek Erdil, thank you for your support and friendship throughout my thesis. My uncle Prof. Dr. Abdullah Tansel, my aunt Aysel Tansel and my lovely grandmother Fatma Tansel are always there for me whenever I need.

My greatest thanks go to my father, Prof. Dr. Mehmet Kemal Leblebiciođlu and my mother, Ayře Leblebiciođlu for their support, guidance and inspiration all through my life. I love them more than anything in the world.

TABLE OF CONTENTS

ABSTRACT.....	iii
ÖZET	v
ACKNOWLEDGMENTS	viii
TABLE OF CONTENTS.....	ix
LIST OF TABLES	xii
LIST OF FIGURES	xv
1 Introduction.....	1
1.1 Motivation of the Thesis	2
1.2 Literature Survey about Modeling	3
1.3 Literature Survey about Control	5
1.4 Primary Contributions of the Thesis	9
1.5 Organization of the Thesis	10
2 Mathematical Model of the System.....	11
2.1 Kinematic Equations for the Rotational Motion of the Two-Axis Gimbal	13
2.2 Kinematic Equations for the Translational Motion of the Two-Axis Gimbal ..	16

2.3	Dynamics Equations for the Translational and Rotational Motion of the Two-Axis Gimbal	21
2.4	Implementation and Simulation of Forward and Inverse Dynamics Models ..	28
3	Test Set-Up and Experimental Data Collection	35
3.1	Implementation of Inverse Dynamics Model in the Experimental Set-Up.....	38
4	Parameter Sensitivity Analysis	44
4.1	First MCS: Effects of Distance Parameters	46
4.2	Second MCS: Effects of Viscous Friction Coefficients	51
4.3	Third MCS: Effects of Off-Diagonal Inertia Terms	53
5	Disturbance Torque Estimation Study Using the Experimental Set-Up ..	57
5.1	Approach 1: Disturbance Torque (Trimming Torque) Estimation by Using the Stabilization Loop	58
5.2	Approach 2: Disturbance Torque Estimation by Using Ideal Inverse Dynamics-Real Plant-Ideal Inverse Dynamics.....	69
6	MLP-Assisted Control Structure.....	76
6.1	Method 1: NN Based Control Structure with Inverse Gimbal Dynamics (NNX)	
	77	
6.2	Method 2: NN Based Control Structure with Inverse and Forward Gimbal Dynamics (Torque Compensation)	82

6.3 ADRC with ESO Implementation for Inverse and Forward Gimbal Dynamics	93
6.4 Implementation of Method 2 for Real-Time Experiments	108
6.5 Method 3: NN Based Control Structure with Inverse and Forward Gimbal Dynamics (Acceleration Compensation)	113
7 Conclusion	117
BIBLIOGRAPHY	121
APPENDIX A	126
APPENDIX B	133
APPENDIX C	135

LIST OF TABLES

Table 3.1: Distances of the gimbal platform.....	37
Table 3.2: Parameters of the yaw gimbal.....	37
Table 3.3: Parameters of the pitch gimbal	38
Table 3.4: Azimuth and elevation gimbal Reference Sets used in Chapter 3	41
Table 4.1: Significant correlation coefficients related with am_x	47
Table 4.2: Significant correlation coefficients related with Gm_z	48
Table 4.3: Significant correlation coefficients related with Ga_y	49
Table 4.4: Significant correlation coefficients related with Gm_x	49
Table 4.5: Significant correlation coefficients related with b_a and b_e	52
Table 4.6: Significant correlation coefficients related with $Jmxz, Jmzx$	54
Table 4.7: Significant correlation coefficients related with $Jmyz, Jmzy$	55
Table 4.8: Significant correlation coefficients related with $Jaxz, Jazx$	55

Table 5.1: Details regarding DataSets (constant velocity data with simple disturbance function).....	66
Table 5.2: Details regarding DataSets (sinusoidal data with complex disturbance function).....	73
Table 6.1: Azimuth and elevation gimbal Reference Sets used in Section 6.2.....	87
Table 6.2: Azimuth and elevation gimbal Reference Sets used in Section 6.3.....	98
Table 6.3: Percent improvement (azimuth) wrt. PID controller for Reference Set 1	100
Table 6.4: Percent improvement (azimuth) wrt. PID controller for Reference Set 3	101
Table 6.5: Percent improvement (azimuth) wrt. PID controller for Reference Set 5	101
Table 6.6: Percent improvement (azimuth) wrt. PID controller for Reference Set 6	103
Table 6.7: Percent improvement (azimuth) wrt. PID controller for Reference Set 7	103
Table 6.8: Percent improvement (azimuth) wrt. PID controller for Reference Set 10	104
Table 6.9: Disturbed model parameters	105

Table 6.10: Azimuth and elevation gimbal Reference Sets used for Example 2.. 111

Table 6.11: Azimuth and elevation gimbal Reference Sets used in Section 6.5 .. 115

Table 6.12: Mean track error improvement wrt. PID controller for Reference Set 1
..... 116

LIST OF FIGURES

Figure 1.1: Field of View (FOV) is the angular area that a camera can observe at any given time when the gimbal system is stationary. Aim of the gimbal system is to hold the image of the target at the center of the FOV plane by aligning LOS vector with the l' vector and minimizing the error (ε) between them while the vehicle is moving 2

Figure 1.2: Experimental set-up of the multi-axis gimbal system 3

Figure 1.3: Block diagram of a possible three-loop control structure is shown for a physical single-axis gimbal system. R, L and K_b are the parameters of the DC motor, V_b is the back-emf voltage and V_c is the input of the real plant. Commanded tracking, rate and current references are r_c, \dot{r}_c and i_c . Measured states of the real system from sensors are r, \dot{r} and i 7

Figure 2.1: Two-axis gimbal system..... 12

Figure 2.2: Euler angles between reference frames $(\bar{u}_1^{(i)}, \bar{u}_2^{(i)}, \bar{u}_3^{(i)})$ are the unit vectors along x_i, y_i, z_i directions for reference frames $i = b, a, m$ 13

Figure 2.3: The position vector from the Center of Gravity (CoG) of the base platform to the outer ring revolute joint..... 17

Figure 2.4: The Position vector from the outer ring revolute joint to the CoG of the yaw gimbal, $\vec{r}_{Ga/a}$, the position vector from the inner ring revolute joint to the CoG

of the pitch gimbal, $\vec{r}_{Gm/m}$, and the position vector from the outer ring revolute joint to the inner ring revolute joint, $\vec{r}_{m/a}$ 18

Figure 2.5: The position vectors $\vec{r}_{m'/a}$, $\vec{r}_{Ga'/a}$ and $\vec{r}_{Gm'/m}$ for disturbed cases 18

Figure 2.6: Block diagram shows the *Forward Dynamics* of the two-axis gimbal system 26

Figure 2.7: Block diagram shows the *Inverse Dynamics* of the two-axis gimbal system 26

Figure 2.8: Block diagram shows the *Inverse* and *Forward Dynamics* of the two-axis gimbal system 27

Figure 2.9: Base platform disturbance data (p, q, r, a_x, a_y, a_z) 29

Figure 2.10: Yaw gimbal's commanded position input for the *Inverse Dynamics*, ψ_{ac} , and the position output from the *Forward Dynamics*, ψ_a 29

Figure 2.11: Yaw gimbal's commanded velocity input for the *Inverse Dynamics*, $\dot{\psi}_{ac}$, and the velocity output from the *Forward Dynamics*, $\dot{\psi}_a$ 31

Figure 2.12: Yaw gimbal's commanded acceleration input for the *Inverse Dynamics*, $\ddot{\psi}_{ac}$, and the acceleration output from the *Forward Dynamics*, $\ddot{\psi}_a$ 31

Figure 2.13: z-component of $\bar{M}_{a/m}^{(a)}$ calculated from *Inverse* and *Forward Dynamics* model 32

Figure 2.14: x-component of $\bar{F}_{a/b}^{(a)}$ calculated from Inverse and Forward Dynamics model.....	33
Figure 2.15: Yaw gimbal's commanded position input for the <i>Inverse Dynamics</i> , ψ_{ac} , and the position output from the <i>Forward Dynamics</i> , ψ_a under different disturbances.....	33
Figure 2.16: Plot showing the difference between ψ_a and r_m plotted for the position command of <i>Inverse Dynamics</i> , $20^\circ@4\text{Hz}$	34
Figure 3.1: The experimental set-up of the two-axis gimbal system.....	36
Figure 3.2: Open loop block diagram used in xPC Target for obtaining <i>Real Plant</i> outputs.....	40
Figure 3.3: Block diagram representation of the <i>Motor Dynamics</i> used in xPC Target (Torque to Voltage conversion).....	40
Figure 3.4: Open loop response of the system for Reference Set 1.....	41
Figure 3.5: Open loop response of the system for Reference Set 2.....	42
Figure 3.6: Open loop response of the system for Reference Set 3.....	42
Figure 3.7: Open loop response of the System for Reference Set 4.....	43
Figure 4.1: Block diagram of the <i>Inverse Gimbal Dynamics</i> used for nominal outputs.....	46

Figure 4.2: Block diagram of the <i>Inverse Gimbal Dynamics</i> in the first MCS	47
Figure 4.3: Distribution of T_e wrt. changes in distance parameters.....	50
Figure 4.4: Distribution of F_{amx} wrt. changes in distance parameters	50
Figure 4.5: Distribution of M_{amz} wrt. changes in distance parameters	51
Figure 4.6: Block diagram of the <i>Inverse Gimbal Dynamics</i> in the second MCS..	52
Figure 4.7: Distribution of T_a wrt. changes in friction coefficients.....	53
Figure 4.8: Block diagram of the <i>Inverse Gimbal Dynamics</i> in the third MCS	54
Figure 4.9: Distribution of T_e wrt. changes in inertia parameters and the QQ Plot	55
Figure 4.10: Distribution of M_{amx} wrt. changes in inertia parameters and the QQ Plot	56
Figure 4.11: Distribution of M_{aby} wrt. changes in inertia parameters.....	56
Figure 5.1: The disturbance torque-velocity graph of the azimuth gimbal from the experimental data	60
Figure 5.2: The disturbance torque-velocity graph of the elevation gimbal from the experimental data	60
Figure 5.3: The disturbance torque-position graph of the azimuth gimbal from the experimental data	61

Figure 5.4: The disturbance torque-position graph of the elevation gimbal from the experimental data	61
Figure 5.5: The position-time and disturbance torque-time graphs of the elevation gimbal from the experimental data under pulse input	63
Figure 5.6: The disturbance torque graph of the elevation gimbal for different azimuth gimbal velocities	64
Figure 5.7: The estimated disturbance torque-real disturbance torque graph for DataSet 1 plotted both for azimuth and elevation gimbals with the coefficient set of DataSet 1	67
Figure 5.8: The estimated disturbance torque-real disturbance torque graph for DataSet 5 plotted both for azimuth and elevation gimbals with the coefficient set of DataSet 1	68
Figure 5.9: The estimated disturbance torque-real disturbance torque graph for DataSet 4 plotted both for azimuth and elevation gimbals with the coefficient set of DataSet 1	68
Figure 5.10: Open loop block diagram used in xPC Target for calculating T_{da} and T_{dm}	70
Figure 5.11: T_{ac} , T_{ma} and T_{da} plotted for the $10^\circ@2\text{ Hz}$ commanded position input of the azimuth gimbal	71
Figure 5.12: T_{ac} , T_{ma} and T_{da} plotted for the $3^\circ@5\text{ Hz}$ commanded position input of the azimuth gimbal.....	72

Figure 5.13: T_{ac} , T_{ma} and T_{da} plotted for the $5^\circ@4\text{ Hz}$ commanded position input of the azimuth gimbal.....	72
Figure 5.14: The estimated disturbance torque-real disturbance torque graph for DataSet 6, plotted both for azimuth and elevation gimbals with the coefficient set of DataSet 6.....	74
Figure 5.15: The estimated disturbance torque-real disturbance torque graph for DataSet 7, plotted both for azimuth and elevation gimbals with the coefficient set of DataSet 6.....	74
Figure 6.1: Training method for NNX (Neural Network X).....	78
Figure 6.2: Input-output relationship of NNX	78
Figure 6.3: Block diagram implementation of NNX in open loop structure	79
Figure 6.4: NNX training input for azimuth and elevation axes.....	80
Figure 6.5: Azimuth and elevation gimbal position with NNX structure	81
Figure 6.6: Training structure used in Simulink® for Method 2.....	83
Figure 6.7: <i>Motor Dynamics</i> block in Simulink® ($T2V$ and $V2T$ conversions)	83
Figure 6.8: Input-output relationship of the NN	84
Figure 6.9: Block diagram implementation of NN with cascaded PID controllers in Simulink®.....	85

Figure 6.10: NN training input for azimuth and elevation axes.....	86
Figure 6.11: An image from MATLAB® Neural Network Toolbox	86
Figure 6.12: Response of the azimuth and elevation gimbals for the pulse input ..	87
Figure 6.13: Azimuth gimbal position for the sinusoidal input with PID set 1 (15° and 1 Hz).....	88
Figure 6.14: Elevation gimbal position for the sinusoidal input with PID set 1 (8° and 1 Hz).....	89
Figure 6.15: Azimuth gimbal position for the sinusoidal input with PID set 2 (15° and 1 Hz).....	90
Figure 6.16: Azimuth gimbal position for the sinusoidal input with PID set 2 (8° and 1 Hz).....	90
Figure 6.17: Azimuth gimbal response corresponding to chirp signal	91
Figure 6.18: Elevation gimbal response corresponding to chirp signal.....	91
Figure 6.19: Azimuth and elevation gimbal's response for the Reference Set 2....	92
Figure 6.20: Block diagram implementation of <i>Transient Profile Generator</i> and <i>Nonlinear Weighted Sum</i> with <i>Inverse</i> and <i>Forward Gimbal Dynamics</i> in Simulink®	94
Figure 6.21: Block diagram implementation of ADRC with <i>Inverse</i> and <i>Forward Gimbal Dynamics</i> in Simulink®	96

Figure 6.22: Block diagram implementation of cascaded PID controllers with <i>Inverse Dynamics</i> based compensation in Simulink®	97
Figure 6.23: Response of the azimuth and elevation gimbals for the pulse train input with ADRC	98
Figure 6.24: Response of the azimuth gimbal for Reference Set 1	100
Figure 6.25: Response of the azimuth gimbal for Reference Set 3	100
Figure 6.26: Response of the azimuth gimbal for Reference Set 5	101
Figure 6.27: Mean tracking and peak errors (azimuth) of each controller for Reference Sets 1-5	102
Figure 6.28: Response of the azimuth gimbal for Reference Set 6	102
Figure 6.29: Response of the azimuth gimbal for Reference Set 7	103
Figure 6.30: Response of the azimuth gimbal for Reference Set 10	104
Figure 6.31: Mean tracking and peak errors (azimuth) of each controller for Reference Sets 6-10	105
Figure 6.32: Response of the azimuth gimbal for Reference Set 2 under model parameter disturbances.....	106
Figure 6.33: Changes in the mean tracking error of the azimuth gimbal for Reference Set 2: orange columns represent the mean tracking error for the experiment performed with disturbed model parameters	107

Figure 6.34: Reference Sets used with the physical gimbal for Example 1	109
Figure 6.35: Response of the azimuth gimbal for the training input ($5^\circ@3\text{Hz}$) with NN based controller	110
Figure 6.36: Response of the azimuth and elevation gimbals for the reference input ($6^\circ@2\text{Hz}$) with NN based controller	110
Figure 6.37: Elevation gimbal response corresponding to chirp signal in xPC Target with PID controllers	111
Figure 6.38: Elevation gimbal response corresponding to Reference Set 1 with NN based controller	112
Figure 6.39: Training structure used in Simulink® for Method 3	113
Figure 6.40: Input-output relationship of the NN used with Method 3	114
Figure 6.41: Block diagram implementation of the proposed NN in Simulink® (Method 3)	114
Figure 6.42: Response of the azimuth gimbal and elevation gimbals for Reference Set 1	115
Figure 6.43: Response of the azimuth gimbal with PID and NN based controllers (Method 3) for the Reference Set 2.....	116

Chapter 1

Introduction

In past few decades, civil and military applications of unmanned aerospace vehicles have been steadily increasing. Unmanned aerospace vehicles (such as rockets, drones, and satellites) usually carry sensors as their primary payload. Hence, electro-optical and/or infrared imaging cameras are used for image processing, target tracking, surveillance, mapping, and providing high-resolution imagery for environmental surveys [1].

As expected, it is crucial to obtain a steady image in all of those applications, which is typically accomplished by using multi-axis gimbal systems. They ensure the line-of-sight (LOS) of the camera payload stays stable and stationary when aligned onto a desired target or point of interest. This provision should also be robust to disturbances originated by the motion of the host vehicle (Fig. 1.1). Furthermore, in coordination with the tracking algorithm, the gimbal system steers the LOS vector onto the target and provides information to estimate its relative angular position [1, 2]. With that information, the vehicle is guided along the desired trajectory or onto the target.

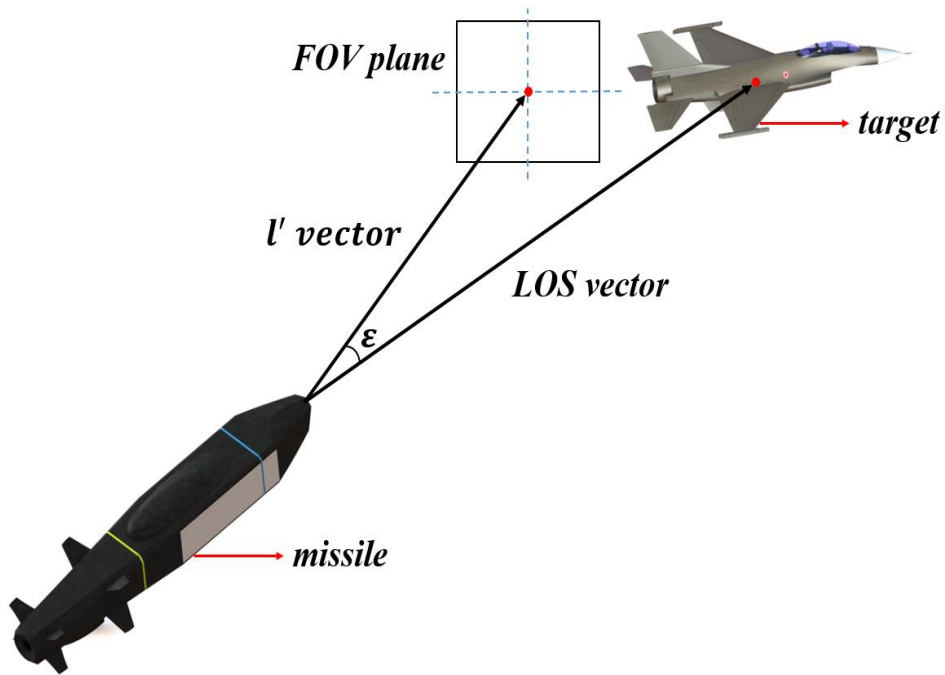
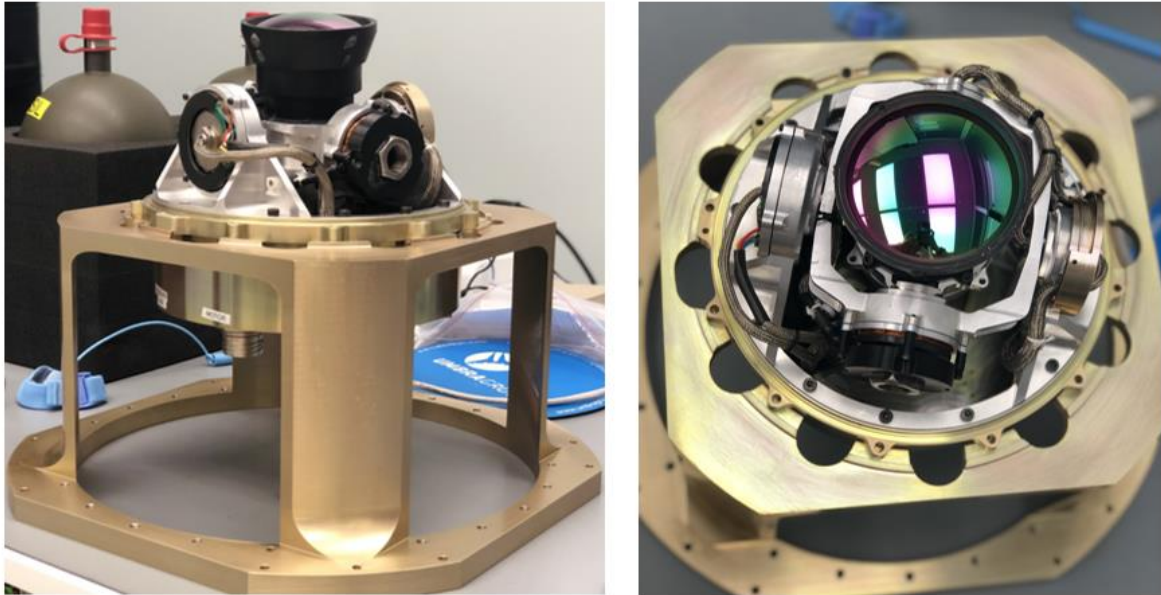


Figure 1.1: Field of View (FOV) is the angular area that a camera can observe at any given time when the gimbal system is stationary. Aim of the gimbal system is to hold the image of the target at the center of the FOV plane by aligning LOS vector with the l' vector and minimizing the error (ϵ) between them while the vehicle is moving

1.1 Motivation of the Thesis

Multi-axis gimbal systems are used as IIR seekers in missiles. This study concentrates on the modeling and control of the multi-axis gimbal system that will be mounted on an unmanned aerial vehicle (i.e., a surface-to-surface tactical missile). Pictures of the multi-axis gimbal system that this study is based on are given in Fig. 1.2. First objective of this thesis is to develop the detailed mathematical model of the real set-up (shown with Fig. 1.2). Second objective is to improve the tracking performance of the system that is currently working with conventional cascaded PID controllers by adding a coupled, neural network based disturbance torque compensation mechanism. Neural network estimates the nonlinear disturbances

present in the system by learning the torque required to achieve the reference motion. This enables the seeker to align with the LOS vector better.



(a) Side-view

(b) Top-view

Figure 1.2: Experimental set-up of the multi-axis gimbal system

1.2 Literature Survey about Modeling

A two-axis gimbal system used in imaging applications is given in Figure 2.1. The two-axis gimbal system is a two-degrees of freedom (2-DoF) chain mechanism in which revolute joints connect the inner gimbal to the outer gimbal and the outer gimbal to the base platform. The differential equations that define the motion of that multi-body system (by its physical nature) are nonlinear, highly coupled and therefore, difficult to model with high fidelity.

So far, the research that focuses on mathematical modeling of gimbal platforms usually uses various assumptions to simplify the equations of motion (EOM).

Mathematical models of gimbals can be obtained by following either the Newton-Euler formulation or the Lagrangian approach [4, 6]. In [4], it is assumed that rotation axes of inner and outer gimbals coincide at a single point and the center of gravity (CoG) of the whole mechanism is located at that same pivot point. In [6], it is considered that there is an offset between the center of gravity of the whole system and that pivot point, but it is still assumed that rotation axes of inner and outer gimbals coincide. Some research papers present plant dynamics using only mass moment of inertia terms [10, 11, 12, 13 and 23]. In [7, 8 and 25], researchers have simplified their gimbal models by neglecting dynamical mass unbalance (which implies that the inertia tensors of the inner and outer gimbals contain off-diagonal terms) and reduced the effect of cross-coupling. In [9, 22], the impact of dynamical mass unbalance is included, but the center of gravity offsets, rotation axes misalignments and disturbance forces/moments are not explicitly modeled. In [14, 15], the cross-coupling terms, friction forces/moments on the joints and other sources of model uncertainties, external disturbances are counted together to generate collective disturbance torques, acting on the gimbal joints.

The two-axis gimbal platform model used in [16] and [17] includes joint reaction moments on azimuth and elevation gimbals. However, the inertia matrices are composed only of diagonal terms and no information on the center of gravity offsets or, rotation axes misalignments is provided. The two-axis gimbal model proposed in [18] includes mass unbalance as a disturbance torque for both inner and outer gimbals, but this does not explicitly mention the dynamical mass unbalance generated by the off-diagonal terms of the moment of inertia matrices of the inner and outer gimbals. [18], rather defines joint reaction forces as unbalance torques.

Contributions of this study regarding modeling are explained below:

Considering the related literature and references, [1], [19] and [20] present the most sophisticated and fundamental models, regarding their contribution on the design principles of multi-axis gimbal systems, derivation of detailed kinematic and

dynamic equations, expressions on cross-coupling effects, reaction moments and disturbance torques. However, those articles do not consider the misalignments between rotation axes of gimbals, the offsets between the center of gravity of the gimbals and the rotation axes, the implications of having a 3D system dynamics on the mathematical model (the moment of inertia matrices of the gimbals that contain off-diagonal terms), the disturbances on the joints arising from friction or some other restraining elements of the whole gimbal system (such as cables, wires, pipes) and the reaction forces and moments on the connection joints of the gimbal system in detail.

In this study, different from the existing works [1, 4, 6-20, 22-25]; a two-axis gimbal system is modeled using multi-body dynamics modeling techniques. Thus, we outline a novel and fully detailed procedure to derive the EOM of a two-axis gimbal system by using Newton-Euler formulation. Furthermore, the proposed model is simulated with MATLAB® 2020b, [21], for a representative two-axis gimbal model of the real system (details regarding the real system are given in Chapter 3) with the corresponding forward and inverse dynamic models.

1.3 Literature Survey about Control

As mentioned earlier, a two-axis gimbal is a MIMO (multiple-input and multiple-output) complex nonlinear system that is susceptible to the influence of unknown frictional torques, external disturbances and system uncertainties. Thus, various control strategies have been developed to satisfy the accurate positioning requirements during target tracking. Controller of a two-axis gimbal system is generally implemented by a three loop structure (Fig. 1.3). The outer loop is the tracking loop and it is the position controller. Tracking loop minimizes the error between the LOS vector and the l' vector (Fig. 1.1). The middle loop is the stabilization loop and it is the rate controller. Stabilization loop eliminates base disturbances after the host vehicle locks-on to the target. The inner loop controls the

current produced by the motor. Traditional and straightforward control approaches such as proportional-integral-derivative (PID) controller, cascaded PID controller or proportional-integral (PI) controller [4, 6] are used in tracking and stabilization loops, over the past decade. Many researchers also worked on more advanced control structures that can adjust to the environmental changes. They tried to develop controllers that show nearly the same performance for every reference input in the operation range. When nonlinear frictional effects are significant, classical controllers are insufficient for compensation due to their limited capability, [2, 7, 8, 15, 18, 22, and 23]. In [24], H_∞ , Linear Quadratic Gaussian/Loop Transfer Recovery (LQG/LTR) and μ -synthesis controllers are designed for the stabilization loop by using the gimbal model proposed in [20]. Elimination of dynamical mass unbalance and cross-coupling terms from the equations proposed in [20], enables the controller design to be performed in a much simpler mathematical model. Active Disturbance Rejection Control (ADRC) theory, has been implemented in [5, 7, 23]. In [13], the LuGre model is used to represent the nonlinear friction behavior present in the inertially stabilized platform (ISP). Friction model parameters are identified and an backstepping integral adaptive compensator is designed to compensate for this disturbance in [13]. Sliding Mode Control (SMC) and improved strategies that enhance the disturbance rejection rate of SMC have been used in [2, 8, 14, 17, 18, 22]. A hybrid control strategy that combines incomplete derivative PID controller (IDPID) and a disturbance observer (DOB) for disturbance compensation and estimation is proposed in [15]. A friction compensator is designed to compensate for the loss due to friction torque which is represented by the Stribeck model. A robust adaptive integral backstepping controller (RAIB) with friction compensation is designed and implemented with a DOB in [12]. It estimates the nonlinear friction torque introduced by the LuGre model and external disturbances in the gimbal system. Aforementioned control structures are complex and have various parameters to adjust during the analytical design phase, [6, 18, 23]. ADRC theory has been one of the popular and useful methods in the area of controller design for gimbal systems since its proposal by J. Han in [35]. Even though ADRC implementation with linear

extended state observer (ESO) has less parameters to tune compared to nonlinear ESO design, two different ESOs will be designed for a two-axis gimbal system. SISO (single-input and single-output) ADRC controller is designed for each channel. Neural network-based control schemes [8, 11, 25] are another outstanding trend in the adaptive gimbal control field. Radial Basis Function Neural Network (RBFNN) is used with SMC in [8] and with state feedback control in [25]. A neural network based adaptive technique is employed for dead-zone effect compensation caused by the limitations of actuators in [11]. Neural networks (NNs) are effective tools for representing complex behaviors, possibly originating from parameter uncertainties, unmodeled dynamics and disturbance effects in nonlinear systems, [26]. Furthermore, they can also be used to enhance the closed-loop control performance of readily existing, and previously designed, legacy controllers, [27].

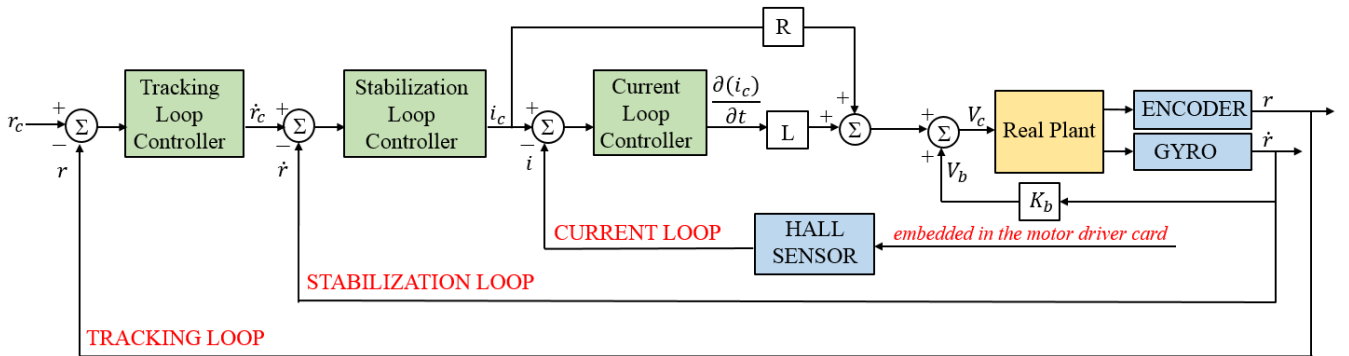


Figure 1.3: Block diagram of a possible three-loop control structure is shown for a physical single-axis gimbal system. R, L and K_b are the parameters of the DC motor, V_b is the back-emf voltage and V_c is the input of the real plant. Commanded tracking, rate and current references are r_c, \dot{r}_c and i_c . Measured states of the real system from sensors are r, \dot{r} and i

Contributions of this study regarding control are explained below:

In this study, we use a neural network structure, i.e., a multilayer perceptron (MLP) for supplementary compensation of external and internal disturbances and parameter uncertainties, through torque input channel. The mentioned disturbances primarily caused by nonlinear friction on the revolute joints connecting the inner gimbal to outer gimbal and the outer gimbal to the base platform. In addition to the nonlinear friction torque in the revolute joints, there are internal disturbances that are caused by model uncertainties. These mainly refer to disturbances as a result of CoG and rotation axis-offsets and off-diagonal terms in the mass moment of inertia matrices. Furthermore, electrical cables of motors, encoders/resolvers, gyroscope and cooling pipes of sensor system generate, gimbal pose and state dependent, time varying additional disturbances. Hence, it is very hard to accurately represent the disturbances in all operation regimes with a single model, [31]. Well-known frictional torque models such as LuGre, Dahl or Stribeck, are usually not satisfactory enough in modeling the disturbances. Most mechanical systems are under the impact of position dependent friction models whose parameters can vary according to velocity and environment of the system, material properties and payload characteristics, [32, 33, 34]. Moreover, overall disturbance torque acting on the system (including frictional torque and additional disturbances), cannot be represented by only using a model-based friction formulation. In literature [12, 13, 15], parameters of well-known friction models are identified by assuming the gimbal system as a rotating inertia rather than a mechanism with linkages. This assumption leads to the conclusion that all disturbances in the system can be modeled as nonlinear frictional torque. Internal disturbance torques caused by model uncertainties are neglected or treated as friction.

In our approach, we also used the multilayer perceptron (MLP) structure to support and enhance the control performance, by increasing the equivalent bandwidth of the closed-loop system and by decreasing the time delay in the response, of a previously designed simple PID controller. This structure enables rapid prototyping design with its ease of implementation and performs MIMO-based compensation for a cross-

coupled system. Proposed method, also improves the response of the system in almost all ranges in the FOR limits of the set-up without requiring any tuning or adjustment. Different from the existing articles in literature [1-20, 22-29], inverse and forward gimbal dynamics of a two-axis gimbal system are used together both in the cascaded PID control and NN-based control structures. By using inverse and forward gimbal dynamics consecutively, a new procedure for collecting the training data of a NN is developed.

1.4 Primary Contributions of the Thesis

As a summary, the primary contributions of this study are; (i) the gimbals are modeled as separate rigid bodies that can make 6-DoF yet constrained motion (since the gimbals are connected to each other and base platform by 1-DoF revolute joints), (ii) besides the customary rotational motion of the gimbals, the translational motion is also modeled, (iii) the offsets between the center of gravity of the gimbals and the rotation axes, the off-diagonal terms of the moment of inertia matrices, the disturbances on the joints and the reaction forces and moments on the connection joints of the gimbal system are all taken into account, (iv) in addition to the forward dynamics model, the inverse dynamics model is also generated to estimate the complementary torque values to compensate the gimbal pose dependent, time varying disturbances, (v) a multilayer perceptron (MLP) structure based disturbance compensator is implemented to cope with external and internal disturbances and parameter uncertainties through torque input channel. Moreover, the MLP structure is used to enhance the control performance of a previously designed simple PID controller, as shown in simulated and real-time experiments, (vi) a new method for collecting training data for the MLP and calculating disturbance torque in the system is developed by using ideal inverse dynamics and forward dynamics (real plant) together in a successive manner.

1.5 Organization of the Thesis

The rest of this thesis is outlined as follows: In Chapter 2, an extensive mathematical model of a two-axis gimbal system is presented. Chapter 3, introduces the gimbal test set-up, experimental data collection and hardware implementation. Chapter 4, presents the sensitivity analysis carried out to discover the effects of parameters that causes non-idealities in the proposed model on reaction forces, moments and driving torques. Disturbance torque identification from the data obtained from the experimental set-up is given in Chapter 5. The construction of the MLP structure and the performance of the proposed MLP structure in terms of disturbance suppression and closed-loop command tracking is presented by simulations and experimental data in Chapter 6. In Chapter 7, the results, discussions and propositions for future work are mentioned.

Chapter 2

Mathematical Model of the System

In this section, the mathematical model of a typical two-axis gimbal system, shown in Figure 2.1, is presented. Ateşoğlu et al. initially presented the modeling approach pursued in this thesis in [28]. In this study, the mathematical model is re-visited and supported with the definitions of *Forward* and *Inverse Gimbal Dynamics*. Then, proposed modeling is implemented on MATLAB® in order to present the use and interaction between *Forward* and *Inverse Gimbal Dynamics* models. The utilization of *Forward* and *Inverse Dynamics* models are populated in Chapter 4, for sensitivity analysis, in Chapter 5, for disturbance torque calculation from the real system and in Chapter 6, for implementation of MLP assisted closed-loop control with simulations using Simulink® and real time experiments with Simulink® Real-Time, [29].

The mechanical structure of the two-axis gimbal system is composed of three interconnected rigid bodies, the inner ring, the outer ring and the base platform. The

primary task of the two-axis gimbal system is to rotate the payload, i.e., the camera mounted on the inner ring, with respect to the base platform. For that purpose, the mechanical design is conducted in such a way that the outer ring performs the azimuth and the inner ring performs the elevation motion. Hence, the outer and inner rings are defined as the yaw and pitch gimbals, respectively. The pitch gimbal is connected to the yaw gimbal. Both gimbals are connected to the base platform with revolute joints. The two-axis gimbal system is assembled to a moving vehicle, which translates and rotates with respect to a chosen inertial reference frame. Hence, the translational acceleration and the angular velocity of the vehicle is directly responsible for the base disturbance on the two-axis gimbal system.

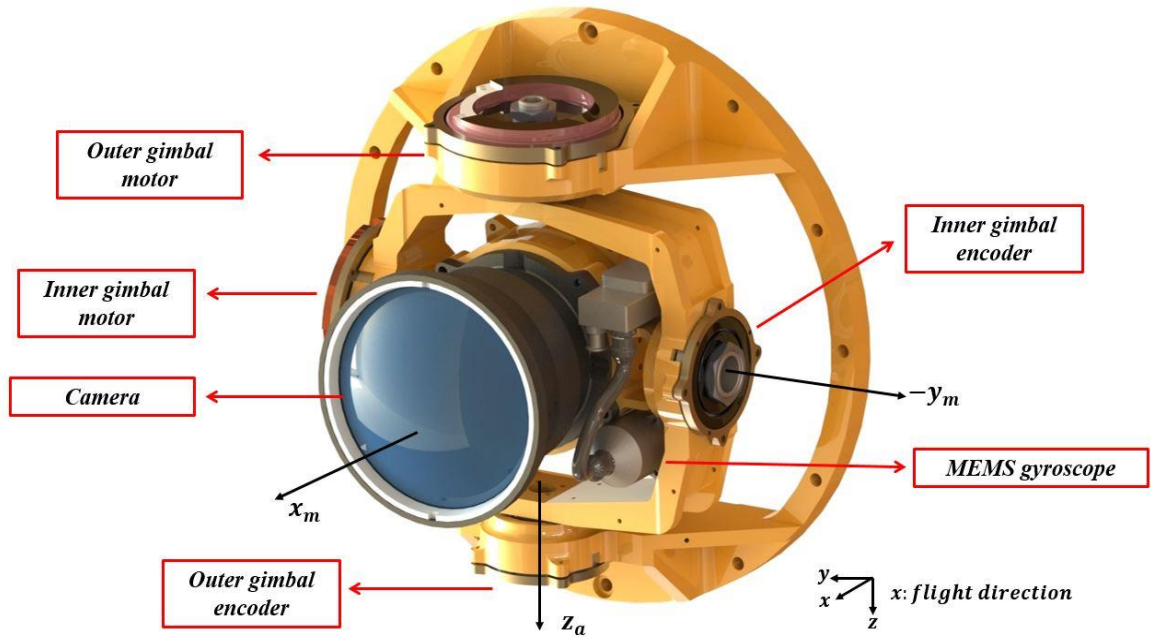


Figure 2.1: Two-axis gimbal system

Two brushless direct current (DC) motors actuate the inner and outer rings of the two-axis gimbal system. Angular position pick-ups are performed by two absolute encoders mounted within the revolute joints, which are joining the yaw gimbal to the base platform and joining the pitch gimbal to the yaw gimbal, respectively. Thus,

they measure the relative angular position of the yaw gimbal with respect to the base platform and the relative angular position of the pitch gimbal with respect to the yaw gimbal. Furthermore, a micro-electromechanical system (MEMS) gyroscope is installed on the pitch gimbal to measure the angular velocity of the pitch gimbal with respect to a chosen inertial reference frame.

2.1 Kinematic Equations for the Rotational Motion of the Two-Axis Gimbal

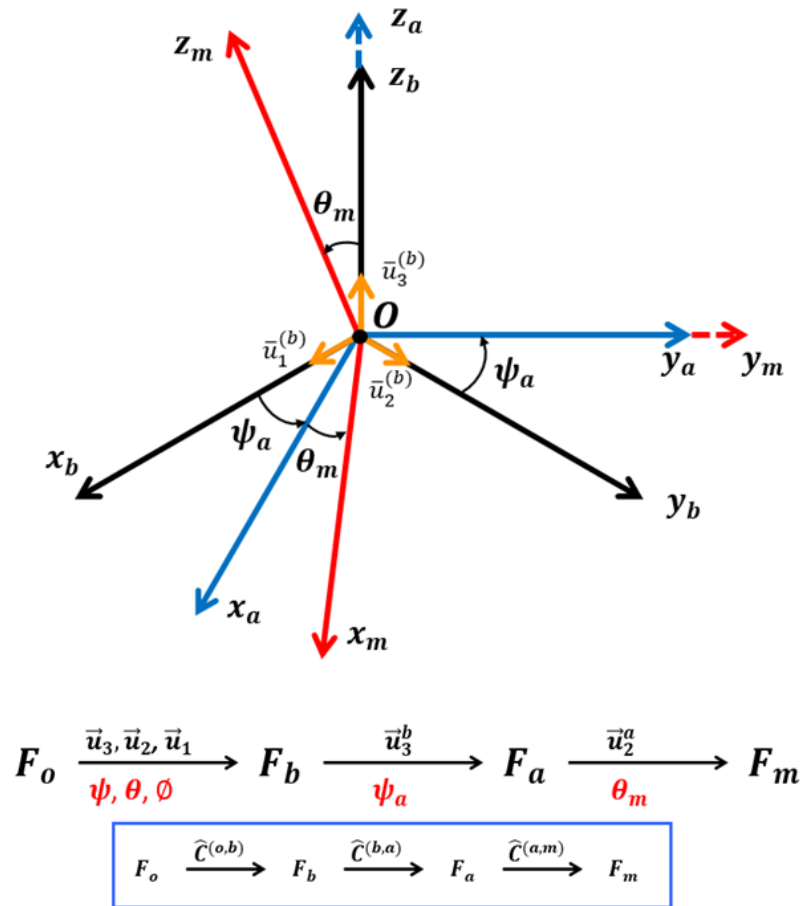


Figure 2.2: Euler angles between reference frames $(\vec{u}_1^{(i)}, \vec{u}_2^{(i)}, \vec{u}_3^{(i)})$ are the unit vectors along x_i, y_i, z_i directions for reference frames $i = b, a, m$)

The rotation between the inertial reference frame F_o (with axes x_o, y_o, z_o) and the base platform reference frame F_b (with axes x_b, y_b, z_b) is defined as a widely used 3-2-1 (yaw-pitch-roll) rotation sequence (Fig. 2.2). Here, first rotation is around the z-axis of the inertial reference frame with angle (ψ), the second rotation is around the y-axis of the rotated consecutive reference frame with angle (θ) and the third rotation is around the x-axis of the last rotated consecutive reference frame with an angle (ϕ). Hence, the corresponding transformation matrix between the base platform reference frame and the inertial reference frame is given below.

$$\mathcal{C}^{(o,b)} = \hat{R}_3(\psi)\hat{R}_2(\theta)\hat{R}_1(\phi) \quad (2.1)$$

Here, \hat{R}_i ($i = 1,2,3$) is the basic rotation matrix used to define the basic rotation (around only one axis) between two consecutive reference frames.

The rotation between the base platform reference frame F_b (with axes x_b, y_b, z_b) and the pitch gimbal (with the camera and the MEMS gyroscope mounted on) reference frame F_m (with axes x_m, y_m, z_m) is defined with a 3-2 (yaw-pitch) rotation sequence. Here, two consecutive rotations should be conducted. First rotation is around the z-axis of the base platform reference frame with angle (ψ_a), the second rotation is around the y-axis of the rotated reference frame, i.e., the outer gimbal reference frame F_a (with axes x_a, y_a, z_a), with angle (θ_m). Hence, the corresponding transformation matrix, between the outer gimbal reference frame and the base platform reference frame is given below.

$$\hat{\mathcal{C}}^{(b,m)} = \hat{\mathcal{C}}^{(b,a)}\hat{\mathcal{C}}^{(a,m)} = \hat{R}_3(\psi_a)\hat{R}_2(\theta_m) \quad (2.2)$$

By using Eqn. 2.1 and Eqn. 2.2, the transformation matrix, between the outer gimbal reference frame and the inertial reference frame can be constructed as follows.

$$\hat{\mathcal{C}}^{(o,m)} = \hat{R}_3(\psi)\hat{R}_2(\theta)\hat{R}_1(\phi)\hat{R}_3(\psi_a)\hat{R}_2(\theta_m) \quad (2.3)$$

The angular velocity ($\bar{\omega}_{b/o}^{(b)}$) and angular acceleration ($\bar{\alpha}_{b/o}^{(b)}$) of the base platform with respect to a chosen inertial reference frame, expressed in the base reference frame and denoted in column matrix representation are given as:

$$\bar{\omega}_{b/o}^{(b)} = [p \ q \ r]^T, \bar{\alpha}_{b/o}^{(b)} = [\dot{p} \ \dot{q} \ \dot{r}]^T \quad (2.4)$$

The angular velocity ($\bar{\omega}_{a/o}^{(a)}$) and angular acceleration of the outer gimbal ($\bar{\alpha}_{a/o}^{(a)}$) with respect to a chosen inertial reference frame expressed in the outer gimbal reference frame is also presented below.

$$\bar{\omega}_{a/o}^{(a)} = \dot{\psi}_a \bar{u}_3^{(a)} + \hat{R}_3(-\psi_a) \bar{\omega}_{b/o}^{(b)} \quad (2.5)$$

$$\bar{\alpha}_{a/o}^{(a)} = \ddot{\psi}_a \bar{u}_3^{(a)} + D \bar{\alpha}_{a/o}^{(a)} \quad (2.6)$$

$$\text{where, } D \bar{\alpha}_{a/o}^{(a)} = \hat{R}_3(-\psi_a) \bar{\alpha}_{b/o}^{(b)} - \dot{\psi}_a \tilde{u}_3 \hat{R}_3(-\psi_a) \bar{\omega}_{b/o}^{(b)} \quad (2.7)$$

Here, $\bar{u}_i^{(i)}$ ($i = 1,2,3$) is the unit vector of the reference frame denoted with $(.)$. Also, the *Tilde* operator (\sim) constructs the skew symmetric matrix form of the column matrix representation of a vector. Furthermore, $D \bar{\alpha}_{a/o}^{(a)}$ in Eqn. 2.7 is used to shorten the expression for $\bar{\alpha}_{a/o}^{(a)}$ in Eqn. 2.6.

The angular velocity ($\bar{\omega}_{m/o}^{(m)}$) and angular acceleration of the pitch gimbal ($\bar{\alpha}_{m/o}^{(m)}$) with respect to a chosen inertial reference frame expressed in the inner gimbal reference frame is presented below.

$$\bar{\omega}_{m/o}^{(m)} = \dot{\theta}_m \bar{u}_2^{(m)} + \dot{\psi}_a \hat{R}_2(-\theta_m) \bar{u}_3^{(a)} + \hat{R}_2(-\theta_m) \hat{R}_3(-\psi_a) \bar{\omega}_{b/o}^{(b)} \quad (2.8)$$

$$\bar{\alpha}_{m/o}^{(m)} = \ddot{\theta}_m \bar{u}_2^{(m)} + \ddot{\psi}_a D_1 \bar{\alpha}_{m/o}^{(m)} + D_2 \bar{\alpha}_{m/o}^{(m)} \quad (2.9)$$

$$\text{where, } D_1 \bar{\alpha}_{m/o}^{(m)} = \hat{R}_2(-\theta_m) \bar{u}_3^{(a)} \quad (2.10)$$

where,

$$\begin{aligned} D_2 \bar{\alpha}_{m/o}^{(m)} = & \hat{R}_2(-\theta_m) \hat{R}_3(-\psi_a) \bar{\alpha}_{b/o}^{(b)} - \\ & \dot{\psi}_a \hat{R}_2(-\theta_m) \hat{R}_3(-\psi_a) \bar{\omega}_{b/o}^{(b)} - \dot{\theta}_m \dot{\psi}_a \tilde{u}_2 \hat{R}_2(-\theta_m) \bar{u}_3^{(a)} - \\ & \dot{\theta}_m \tilde{u}_2 \hat{R}_2(-\theta_m) \hat{R}_3(-\psi_a) \bar{\omega}_{b/o}^{(b)} \end{aligned} \quad (2.11)$$

Here, $D_1 \bar{\alpha}_{m/o}^{(m)}$ and $D_2 \bar{\alpha}_{m/o}^{(m)}$ (Eqn. 2.10 and Eqn. 2.11) are used to shorten the expression for $\bar{\alpha}_{m/o}^{(m)}$.

2.2 Kinematic Equations for the Translational Motion of the Two-Axis Gimbal

A kinematical chain of separate bodies, connected to each other by using mechanical joints, is called a multi-body system. In such a kinematical chain of multi-body system, the mass properties of each bodies are considered separately [30]. In addition, the distances in between consecutive mechanical joints and the distances in between the center of gravity locations and the corresponding mechanical joints of each bodies play important role to construct the equations that represent the translational motion.

The definition of the position vectors, which are used in the translational kinematic equations of motion of the two-axis gimbal system are shown in Figs. 2.3 and 2.4. Here, note that, ideally, the CoG of the yaw gimbal is on the rotation axis of the outer ring and the CoG of the pitch gimbal (with the camera and the MEMS gyroscope mounted on) is on the rotation axis of the inner ring. Also, the pivot point is the intersection point of the rotation axis of the outer ring and the rotation axis of the inner ring. In Figure 2.5, offset between rotation axes of inner and outer gimbals and some cases of displaced CoG points of the inner and outer gimbals from rotation axes are shown.

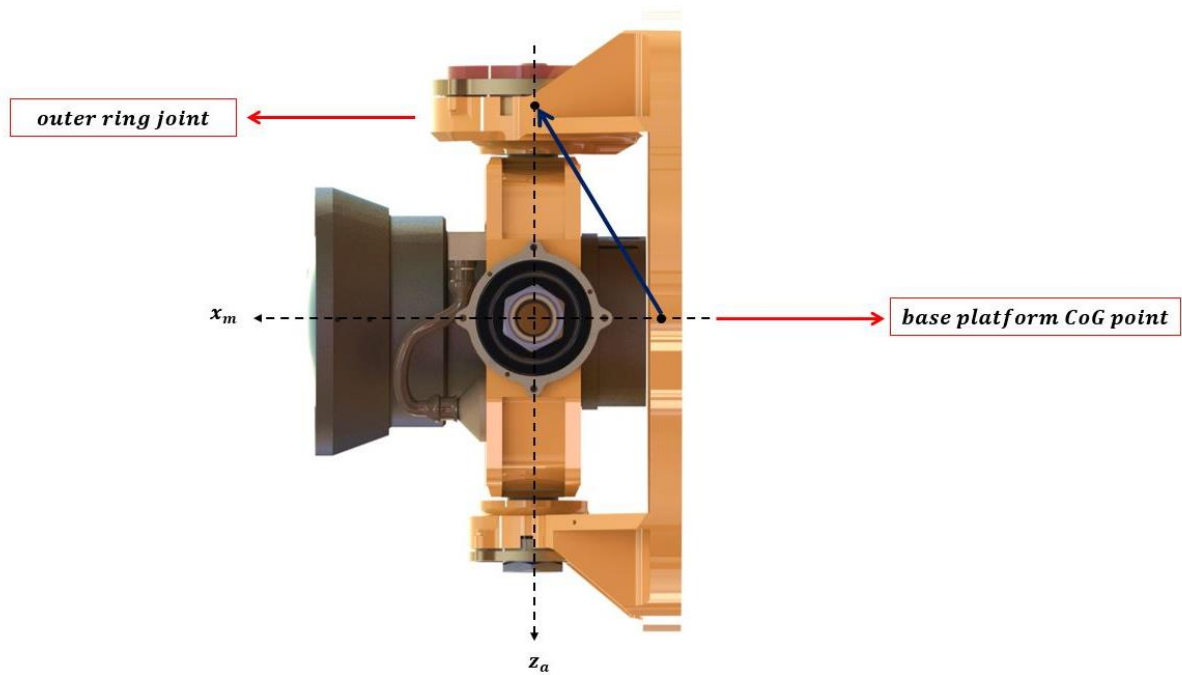


Figure 2.3: The position vector from the Center of Gravity (CoG) of the base platform to the outer ring revolute joint

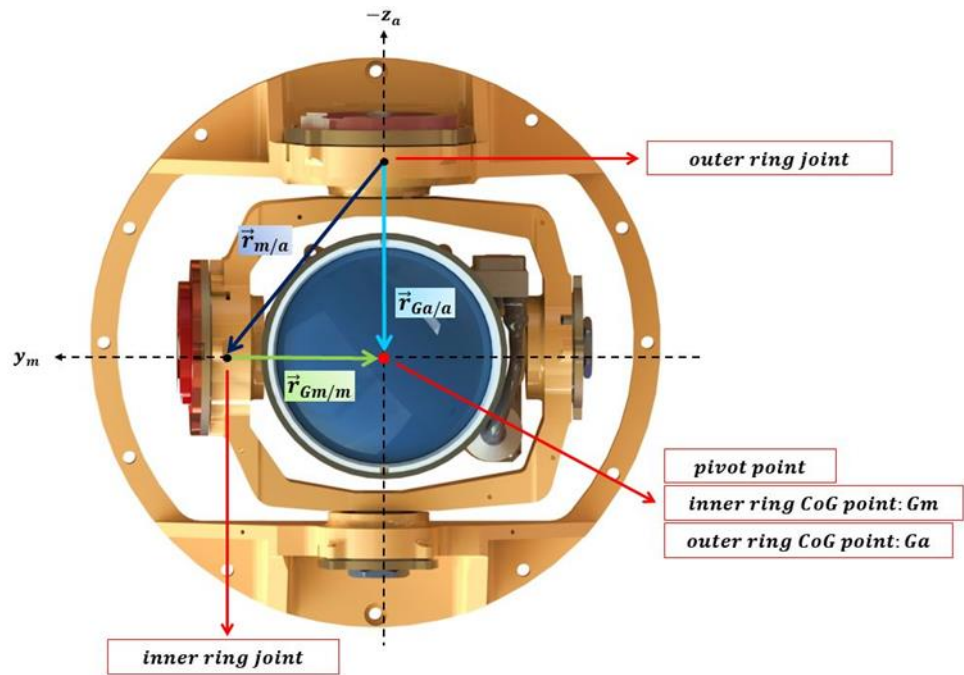


Figure 2.4: The Position vector from the outer ring revolute joint to the CoG of the yaw gimbal, $\vec{r}_{Ga/a}$, the position vector from the inner ring revolute joint to the CoG of the pitch gimbal, $\vec{r}_{Gm/m}$, and the position vector from the outer ring revolute joint to the inner ring revolute joint, $\vec{r}_{m/a}$

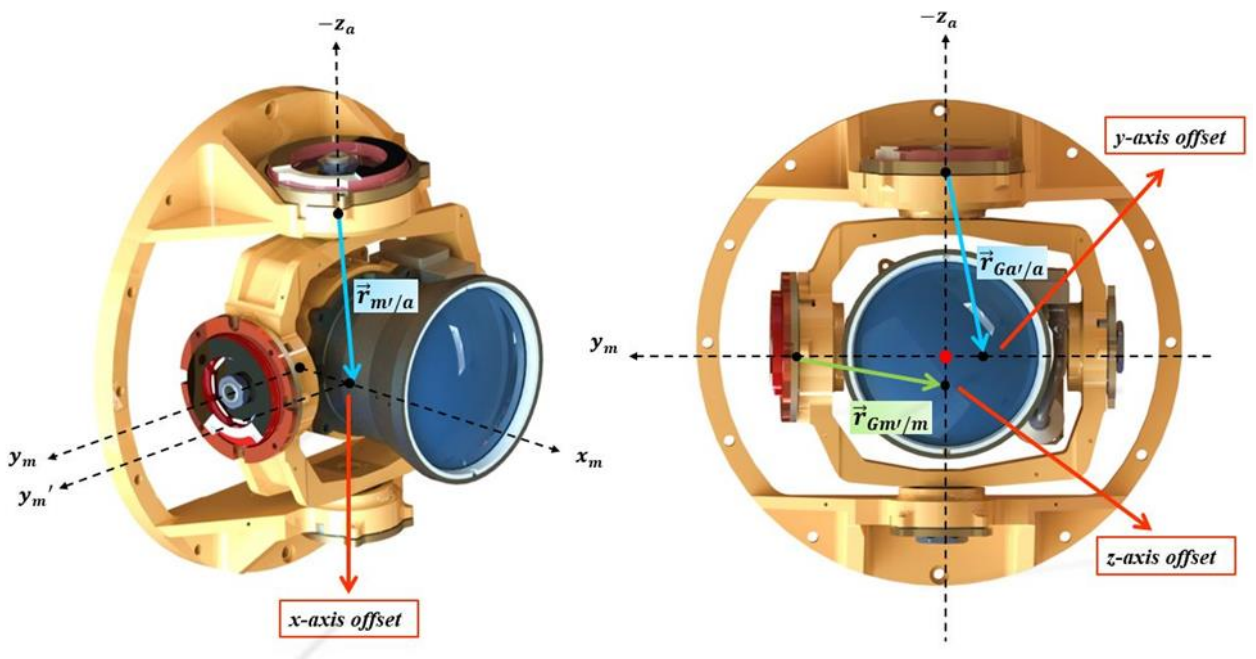


Figure 2.5: The position vectors $\vec{r}_{m'/a}$, $\vec{r}_{Ga'/a}$ and $\vec{r}_{Gm'/m}$ for disturbed cases

The position vector defining the CoG of the yaw gimbal with respect to a chosen inertial frame ($\vec{r}_{Ga/o}$) is the sum of three position vectors: the position vector of the CoG of the base platform with respect to a chosen inertial frame ($\vec{r}_{b/o}$), the vector defining the position of the outer ring revolute joint with respect to the CoG of the base platform ($\vec{r}_{a/b}$) and the position vector of the CoG of the yaw gimbal with respect to the outer ring revolute joint ($\vec{r}_{Ga/a}$).

$$\vec{r}_{Ga/o} = \vec{r}_{Ga/a} + \vec{r}_{a/b} + \vec{r}_{b/o} \quad (2.12)$$

In column matrix notation, we can write the same equation as shown below. Here, the components of the vectors are expressed at F_a :

$$\vec{r}_{Ga/o}^{(a)} = \vec{r}_{Ga/a}^{(a)} + \hat{R}_3(-\psi_a)\vec{r}_{a/b}^{(b)} + \hat{R}_3(-\psi_a)\vec{r}_{b/o}^{(b)} \quad (2.13)$$

By taking the time derivative of both sides of Eqn. 2.13 twice with respect to the inertial reference frame and assuming that the base platform and the yaw gimbal are rigid bodies, we end up with the expression for the translational acceleration of the CoG of the yaw gimbal, with respect to the inertial reference frame.

$$\bar{a}_{Ga/o}^{(a)} = \ddot{\psi}_a \tilde{u}_3 \vec{r}_{Ga/a}^{(a)} + \bar{D} a_{Ga}^{(a)} \quad (2.14)$$

$$\begin{aligned} \bar{D} a_{Ga}^{(a)} = & [D \widetilde{\alpha}_{a/o}^{(a)} + (\widetilde{\omega}_{a/o}^{(a)})^2] \vec{r}_{Ga/a}^{(a)} + \hat{R}_3(-\psi_a) [\widetilde{\alpha}_{b/o}^{(b)} \\ & + (\widetilde{\omega}_{b/o}^{(b)})^2] \vec{r}_{a/b}^{(b)} + \hat{R}_3(-\psi_a) \bar{a}_{b/o}^{(b)} \end{aligned} \quad (2.15)$$

Here, note that, since the base platform and the yaw gimbal are assumed as rigid bodies, first and second time derivatives of $\vec{r}_{a/b}^{(b)}$ and $\vec{r}_{Ga/a}^{(a)}$ are $\bar{0}$. On the other hand, the translational acceleration of the base platform with respect to the inertial

reference frame is defined as $\bar{a}_{b/o}^{(b)} = [a_x \ a_y \ a_z]^T$. Also, $\bar{D}a_{Ga}^{(a)}$ (Eqn. 2.15) is used to shorten the expression of $\bar{a}_{Ga/o}^{(a)}$ in Eqn. 2.14.

In a similar manner, the position vector defining the CoG of the pitch gimbal with respect to a chosen inertial reference frame ($\vec{r}_{Gm/o}$) is the sum of four position vectors.

$$\vec{r}_{Gm/o} = \vec{r}_{Gm/m} + \vec{r}_{m/a} + \vec{r}_{a/b} + \vec{r}_{b/o} \quad (2.16)$$

Here, $\vec{r}_{Gm/m}$ is the position of the CoG of the pitch gimbal with respect to the inner ring revolute joint and $\vec{r}_{m/a}$ is the position of the inner ring revolute joint with respect to the outer ring revolute joint.

In column matrix notation, we can write the same equation as shown below. Here, the components of the vectors are expressed at F_m :

$$\begin{aligned} \bar{r}_{Gm/o}^{(m)} = & \bar{r}_{Gm/m}^{(m)} + \hat{R}_2(-\theta_m)\bar{r}_{m/a}^{(a)} + \hat{R}_2(-\theta_m)\hat{R}_3(-\psi_a)\bar{r}_{a/b}^{(b)} \\ & + \hat{R}_2(-\theta_m)\hat{R}_3(-\psi_a)\bar{r}_{b/o}^{(b)} \end{aligned} \quad (2.17)$$

By taking the time derivative of both sides of Eqn. 2.17 twice with respect to the inertial reference frame and assuming that the yaw and pitch gimbals are rigid bodies, we end up with the expression for the translational acceleration of the CoG of the pitch gimbal, with respect to the inertial reference frame.

$$\bar{a}_{Gm/o}^{(m)} = \ddot{\psi}_a[\hat{R}_2(-\theta_m)\tilde{u}_3\bar{r}_{m/a}^{(a)} + D_1\bar{a}_{m/o}^{(m)}\bar{r}_{Gm/m}^{(m)}] + \ddot{\theta}_m\tilde{u}_2\bar{r}_{Gm/m}^{(m)} + \bar{D}a_{Gm}^{(m)} \quad (2.18)$$

$$\begin{aligned}
\bar{D}a_{Gm}^{(m)} = & [D_2\widetilde{\alpha}_{m/o}^{(m)} + (\widetilde{w}_{m/o}^{(m)})^2]\bar{r}_{Gm/m}^{(m)} + \hat{R}_2(-\theta_m)\hat{R}_3(-\psi_a)[\widetilde{\alpha}_{b/o}^{(b)} \\
& + (\widetilde{w}_{b/o}^{(b)})^2]\bar{r}_{a/b}^{(b)} + \hat{R}_2(-\theta_m)\hat{R}_3(-\psi_a)\bar{a}_{b/o}^{(b)} \\
& + \hat{R}_2(-\theta_m)[D_2\widetilde{\alpha}_{a/o}^{(a)} + (\widetilde{w}_{a/o}^{(a)})^2]\bar{r}_{m/a}^{(a)}
\end{aligned} \tag{2.19}$$

Here note that, since the yaw and pitch gimbals are assumed as rigid bodies, first and second time derivatives of $\bar{r}_{m/a}^{(a)}$ and $\bar{r}_{Gm/m}^{(m)}$ are $\bar{0}$. Also, $\bar{D}a_{Gm}^{(m)}$ (Eqn. 2.19) is used to shorten the expression of $\bar{a}_{Gm/o}^{(m)}$ in Eqn. 2.18. Introduction of distance vectors, $\vec{r}_{a/b}, \vec{r}_{m/a}, \vec{r}_{Ga/a}$ and $\vec{r}_{Gm/m}$, in the mathematical model is an implication of existence of static mass unbalance.

2.3 Dynamics Equations for the Translational and Rotational Motion of the Two-Axis Gimbal

Following the first principles, or namely the Newton-Euler approach, the mathematical model for the translational and rotational dynamics of the yaw gimbal is derived. Here, \hat{J}_a is the moment of inertia matrix of the yaw gimbal. \hat{J}_m is the moment of inertia matrix of the pitch gimbal. There are cross-axis diagonal terms in both \hat{J}_a and \hat{J}_m matrices, implying that dynamical mass unbalance is not neglected (Eqn. 2.20).

$$\hat{J}_a = \begin{bmatrix} J_{axx} & J_{axy} & J_{axz} \\ J_{ayx} & J_{ayy} & J_{ayz} \\ J_{azx} & J_{azy} & J_{azz} \end{bmatrix}, \hat{J}_m = \begin{bmatrix} J_{mxx} & J_{mxy} & J_{mxz} \\ J_{myx} & J_{myy} & J_{myz} \\ J_{mzx} & J_{mzy} & J_{mzz} \end{bmatrix} \tag{2.20}$$

$$m_a(\bar{a}_{Ga/o}^{(a)} - \bar{g}_a) = \bar{F}_{a/m}^{(a)} + \bar{F}_{a/b}^{(a)} \quad (2.21)$$

$$\hat{J}_a \bar{\alpha}_{a/o}^{(a)} + \hat{\omega}_{a/o}^{(a)} \hat{J}_a \bar{\omega}_{a/o}^{(a)} = \bar{M}_{a/m}^{(a)} + \bar{M}_{a/b}^{(a)} + \tilde{r}_{a/m}^{(a)} \bar{F}_{a/m}^{(a)} + \tilde{r}_{a/b}^{(a)} \bar{F}_{a/b}^{(a)} \quad (2.22)$$

In Eqn. 2.21, \bar{g}_a is the gravitational acceleration vector represented at the yaw gimbal reference frame. Also, $\tilde{r}_{a/m}^{(a)} = -\tilde{r}_{m/a}^{(a)}$, $\tilde{r}_{a/b}^{(a)} = \hat{R}_3(-\psi_a) \tilde{r}_{a/b}^{(b)}$ in Eqn. 2.22.

Furthermore, in Eqn. 2.22, $\bar{F}_{a/m}^{(a)} = [F_{amx} \ F_{amy} \ F_{amz}]^T$ is the reaction force on the revolute joint in between the yaw and pitch gimbals, and $\bar{F}_{a/b}^{(a)} = [F_{abx} \ F_{aby} \ F_{abz}]^T$ is the reaction force on the revolute joint in between the yaw gimbal and base platform. $\bar{M}_{a/m}^{(a)} = [M_{amx} \ M_{amy} \ M_{amz}]^T$ is the total moment on the revolute joint in between the yaw and pitch gimbals, and $\bar{M}_{a/b}^{(a)} = [M_{abx} \ M_{aby} \ M_{abz}]^T$ is the total moment on the revolute joint in between the yaw gimbal and base platform.

In $\bar{M}_{a/b}^{(a)}$, $M_{abz} = T_a - T_{fra}$, where T_a is the driving torque applied on the yaw gimbal by the brushless DC motor installed in between the yaw gimbal and the base platform, and T_{fra} is the disturbance torque on the revolute joint in between the outer ring and the base platform.

Similarly, in $\bar{M}_{a/m}^{(a)}$, $M_{amy} = T_e - T_{frm}$, where T_e is the driving torque applied on the pitch gimbal by the brushless DC motor installed in between the pitch gimbal and the yaw gimbal, and T_{frm} is the disturbance torque on the revolute joint between the inner and outer rings of the two-axis gimbal system.

The mathematical model for the translational and rotational dynamics of the pitch gimbal is also derived by applying the Newton-Euler approach.

$$m_m(\bar{a}_{Gm/o}^{(m)} - \bar{g}_m) = \bar{F}_{m/a}^{(m)} \quad (2.23)$$

$$\hat{J}_m \bar{\alpha}_{m/o}^{(m)} + \tilde{\omega}_{m/o}^{(m)} \hat{J}_m \bar{\omega}_{m/o}^{(m)} = \bar{M}_{m/a}^{(m)} + \tilde{r}_{m/a}^{(m)} \bar{F}_{m/a}^{(m)} \quad (2.24)$$

In Eqn. 2.23, \bar{g}_m is the gravitational acceleration vector represented at the pitch gimbal reference frame.

Also, $\tilde{r}_{m/a}^{(m)} = \hat{R}_2(-\theta_m) \tilde{r}_{m/a}^{(a)}$, $\bar{F}_{m/a}^{(m)} = -\hat{R}_2(-\theta_m) \bar{F}_{a/m}^{(a)}$, $\bar{M}_{m/a}^{(m)} = -\hat{R}_2(-\theta_m) \bar{M}_{a/m}^{(a)}$, in Eqn. 2.24.

By careful arrangement of Eqns. 2.21-2.24, the resultant dynamical equations for the multibody dynamics of the two-axis gimbal system is composed in matrix equation form as shown in Eqn. 2.25.

$$\hat{F}_{12 \times 2} \begin{bmatrix} \ddot{\psi}_a \\ \ddot{\theta}_m \end{bmatrix}_{2 \times 1} + \hat{R}_{12 \times 10} \begin{bmatrix} \bar{F}_{a/m}^{(a)} \\ \bar{F}_{a/b}^{(a)} \\ M_{amx} \\ M_{amz} \\ M_{abx} \\ M_{aby} \end{bmatrix}_{10 \times 1} = \hat{D}_{12 \times 1} + \hat{G}_{12 \times 2} \begin{bmatrix} T_a \\ T_e \end{bmatrix}_{2 \times 1} \quad (2.25)$$

Eqn. 2.25 is the compact form of the nonlinear, and coupled, differential equations that represent the *Forward Dynamics* of the two-axis gimbal system. Given the driving, or the control torques, T_a , T_e , the relative angular accelerations of the yaw and pitch gimbals, $\ddot{\psi}_a$, $\ddot{\theta}_m$, can be calculated (Fig. 2.6). Also, thanks to the Newton-Euler mechanization approach, the reaction forces ($\bar{F}_{a/m}^{(a)}$, $\bar{F}_{a/b}^{(a)}$) and the constraining components of reaction moments can also be calculated here as by-products.

The matrices, \hat{F} , \hat{R} , \hat{D} and \hat{G} (in Eqn. 2.25) are presented below.

$$\hat{F} = \begin{bmatrix} m_a \tilde{u}_3 \bar{r}_{Ga/a}^{(a)} & \bar{0} \\ \hat{J}_a \bar{u}_3 & \bar{0} \\ m_m [\hat{R}_2(-\theta_m) \tilde{u}_3 \bar{r}_{m/a}^{(a)} + D_1 \bar{\alpha}_{m/o}^{(m)} \bar{r}_{Gm/m}^{(m)}] & m_m \tilde{u}_2 \bar{r}_{Gm/m}^{(m)} \\ \hat{J}_m D_1 \bar{\alpha}_{m/o}^{(m)} & \hat{J}_m \bar{u}_2 \end{bmatrix} \quad (2.26)$$

$$\hat{R} = \begin{bmatrix} -\hat{I}_{3x3} & -\hat{I}_{3x3} & \hat{O}_{3x2} & \hat{O}_{3x2} \\ -\tilde{r}_{a/m}^{(a)} & -\tilde{r}_{a/b}^{(a)} & -\begin{bmatrix} 1 & 0 \\ 0 & 0 \\ 0 & 1 \end{bmatrix} & -\begin{bmatrix} 1 & 0 \\ 0 & 1 \\ 0 & 0 \end{bmatrix} \\ \hat{R}_2(-\theta_m) & \hat{O}_{3x3} & \hat{O}_{3x2} & \hat{O}_{3x2} \\ \tilde{r}_{m/a}^{(m)} \hat{R}_2(-\theta_m) & \hat{O}_{3x3} & \hat{R}_2(-\theta_m) \begin{bmatrix} 1 & 0 \\ 0 & 0 \\ 0 & 1 \end{bmatrix} & \hat{O}_{3x2} \end{bmatrix} \quad (2.27)$$

$$\hat{D} = \begin{bmatrix} -m_a \bar{D} a_{Ga}^{(a)} + m_a \bar{g}_a \\ -\hat{J}_a D \bar{\alpha}_{a/o}^{(a)} - \tilde{\omega}_{a/o}^{(a)} \hat{J}_a \bar{\omega}_{a/o}^{(a)} + \begin{bmatrix} 0 \\ -T_{frm} \\ -T_{fra} \end{bmatrix} \\ -m_m \bar{D} a_{Gm}^{(m)} + m_m \bar{g}_m \\ -\hat{J}_m D_2 \bar{\alpha}_{m/o}^{(m)} - \tilde{\omega}_{m/o}^{(m)} \hat{J}_m \bar{\omega}_{m/o}^{(m)} - \hat{R}_2(-\theta_m) \begin{bmatrix} 0 \\ -T_{frm} \\ 0 \end{bmatrix} \end{bmatrix} \quad (2.28)$$

$$\hat{G} = \begin{bmatrix} \hat{O}_{3x2} \\ \begin{bmatrix} 0 & 0 \\ 0 & 1 \\ 1 & 0 \end{bmatrix} \\ \hat{O}_{3x2} \\ -\hat{R}_2(-\theta_m) \begin{bmatrix} 0 & 0 \\ 0 & 1 \\ 0 & 0 \end{bmatrix} \end{bmatrix} \quad (2.29)$$

Using Eqn. 2.25, a compact equation representing the *Inverse Dynamics* of the two-axis gimbal system can also be given as in Eqns. 2.30 and 2.31. These equations are used to calculate the commanded torques, T_{ac} , T_{ec} , when the reference values of angular accelerations, $\ddot{\psi}_{ac}$, $\ddot{\theta}_{mc}$, angular velocities, $\dot{\psi}_{ac}$, $\dot{\theta}_{mc}$, and angular positions, ψ_{ac} , θ_{mc} , of the yaw and pitch gimbals are available. The reaction forces and moments, X_i , can again be calculated as by-products of the inverse model (Fig. 2.7).

$$-\hat{G}_{12 \times 2} \begin{bmatrix} T_{ac} \\ T_{ec} \end{bmatrix}_{2 \times 1} + \hat{R}_{12 \times 10} \begin{bmatrix} \bar{F}_{a/m}^{(a)} \\ \bar{F}_{a/b}^{(a)} \\ M_{amx} \\ M_{amz} \\ M_{abx} \\ M_{aby} \end{bmatrix}_{10 \times 1} = -\hat{F}_{12 \times 2} \begin{bmatrix} \ddot{\psi}_{ac} \\ \ddot{\theta}_{mc} \end{bmatrix}_{2 \times 1} + \hat{D}_{12 \times 1} \quad (2.30)$$

$$[-\hat{G}_{12 \times 2} : \hat{R}_{12 \times 10}] \begin{bmatrix} T_{ac} \\ T_{ec} \\ \bar{F}_{a/m}^{(a)} \\ \bar{F}_{a/b}^{(a)} \\ M_{amx} \\ M_{amz} \\ M_{abx} \\ M_{aby} \end{bmatrix}_{12 \times 1} = -\hat{F}_{12 \times 2} \begin{bmatrix} \ddot{\psi}_{ac} \\ \ddot{\theta}_{mc} \end{bmatrix}_{2 \times 1} + \hat{D}_{12 \times 1} \quad (2.31)$$

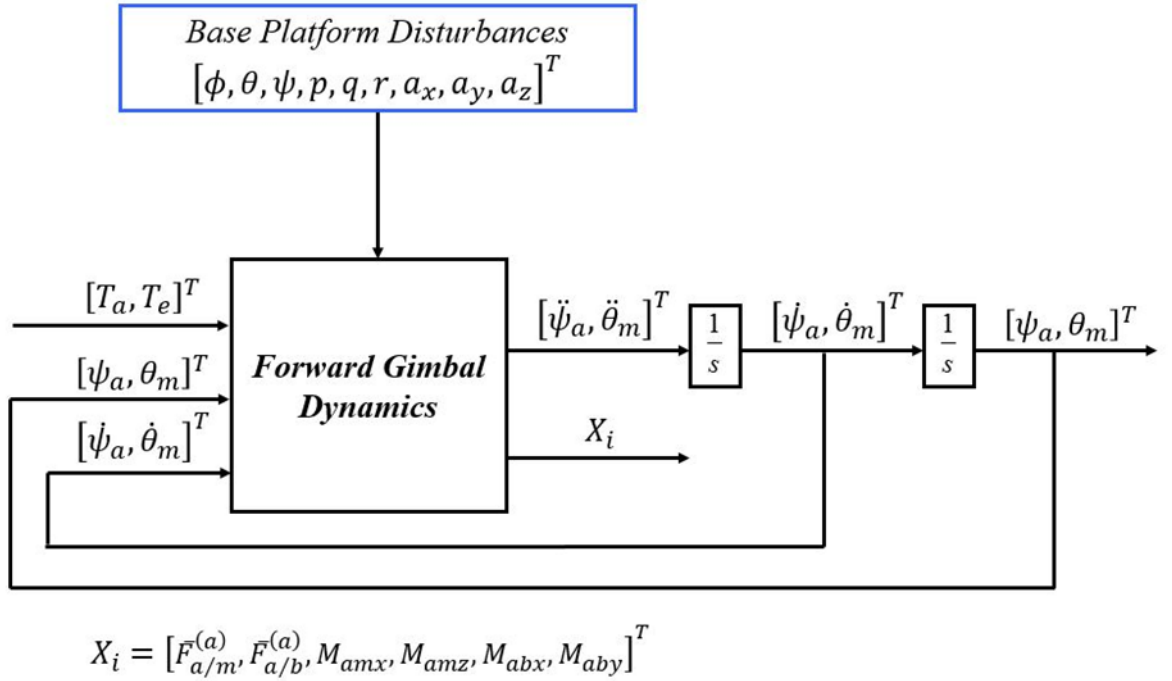


Figure 2.6: Block diagram shows the *Forward Dynamics* of the two-axis gimbal system

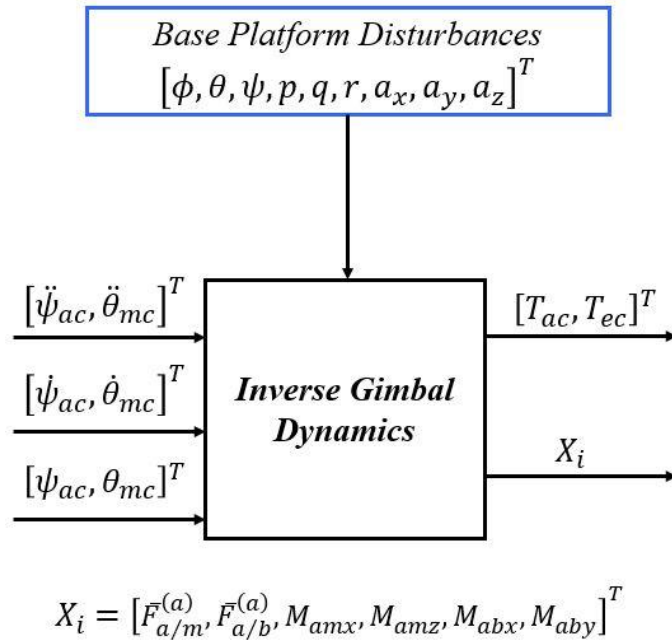


Figure 2.7: Block diagram shows the *Inverse Dynamics* of the two-axis gimbal system

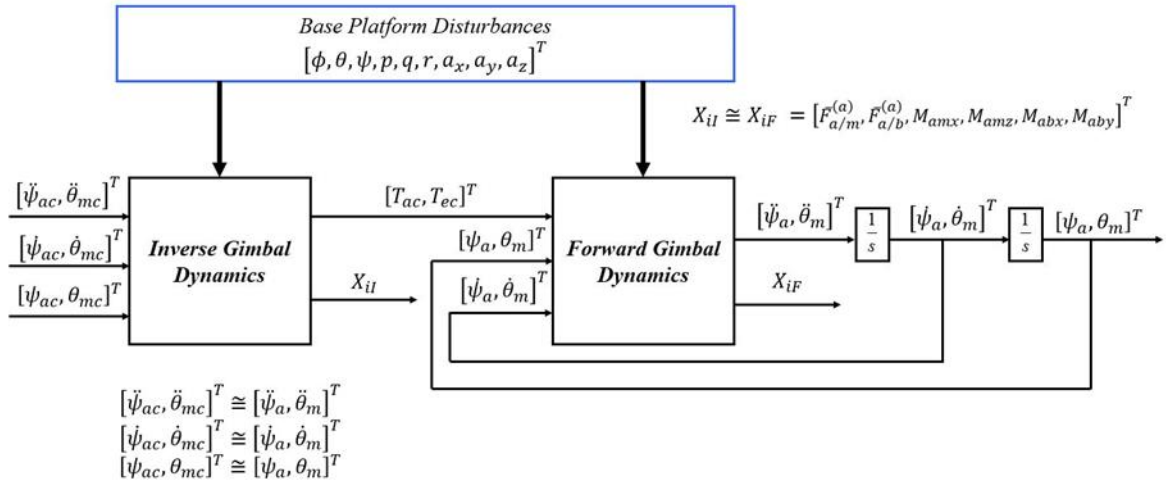


Figure 2.8: Block diagram shows the *Inverse* and *Forward Dynamics* of the two-axis gimbal system

Here, in Fig. 2.8, the outputs of the *Inverse Dynamics* model are the inputs of the *Forward Dynamics* model. Hence, by using the *Inverse Dynamics* model, it is possible to calculate the values of the required torque commands needed to achieve the prescribed reference values of angular accelerations, velocities and positions of the yaw and pitch gimbals. Moreover, the reaction forces and moments, X_{iI} , calculated from the inverse model and X_{iF} , calculated from the forward model are equal to each other. Note that, position, velocity and acceleration outputs of the *Forward Dynamics* model are the same as the input position, velocity and acceleration commanded for the *Inverse Dynamics* model. In Fig. 2.8, commanded position and velocity states given as reference to *Inverse Dynamics* model are not provided from the states of *Forward Dynamics* model. Together with the accumulation of errors in numerical integration, this situation may lead to negligible differences in reaction forces and moments calculated from *Inverse* and *Forward Dynamics* models (X_{iI} and X_{iF}). Commanded values and calculated values of angular accelerations, velocities and positions may also differ slightly. This is the reason of \cong sign in Fig. 2.8.

2.4 Implementation and Simulation of Forward and Inverse Dynamics Models

The proposed gimbal model including *Inverse* and *Forward Dynamics* with Eqns. (2.1-2.31) is implemented on the simulation environment by using MATLAB® and Simulink® software. Equations are programmed as MATLAB® Function blocks. The sampling period of the simulated system is 0.001 seconds and ode4 (Runge-Katta) solver is used for dealing with the coupled nonlinear differential equations used in the proposed model. Properties of the simulated two-axis gimbal system will be provided in Chapter 3 (Test Set-Up and Experimental Data Collection). *Inverse Dynamics* enables to perform sensitivity analysis (Chapter 4). Using *Inverse* and *Forward Dynamics* consecutively, NN-based control structure is implemented and NN training is performed (Chapter 6). Sequential use of *Inverse* and *Forward Dynamics* blocks, is very important for calculating the disturbance torque (including mainly the friction torque and the disturbance torque resulting as a consequence of model non-idealities, i.e., off-diagonal inertia terms, rotation axis and CoG offsets) in the real experimental set-up (Chapter 5).

In order to check the implementation of the cascaded structure of the *Inverse* and *Forward Dynamics* model, the following test-case is investigated. The inverse model is excited with $2^\circ @ 4 \text{ Hz}$ sinusoidal position commands both for the pitch and yaw gimbals under given base platform disturbance data, i.e., p, q, r, a_x, a_y, a_z , which is already obtained from a real-time flight of the carrier vehicle (Fig. 2.9).

The simulation results are given in Fig. 2.10 for the commanded yaw gimbal position, in Fig. 2.11 for the commanded yaw gimbal velocity and in Fig. 2.12 for the commanded yaw gimbal acceleration from the inverse model and the output of the forward model.

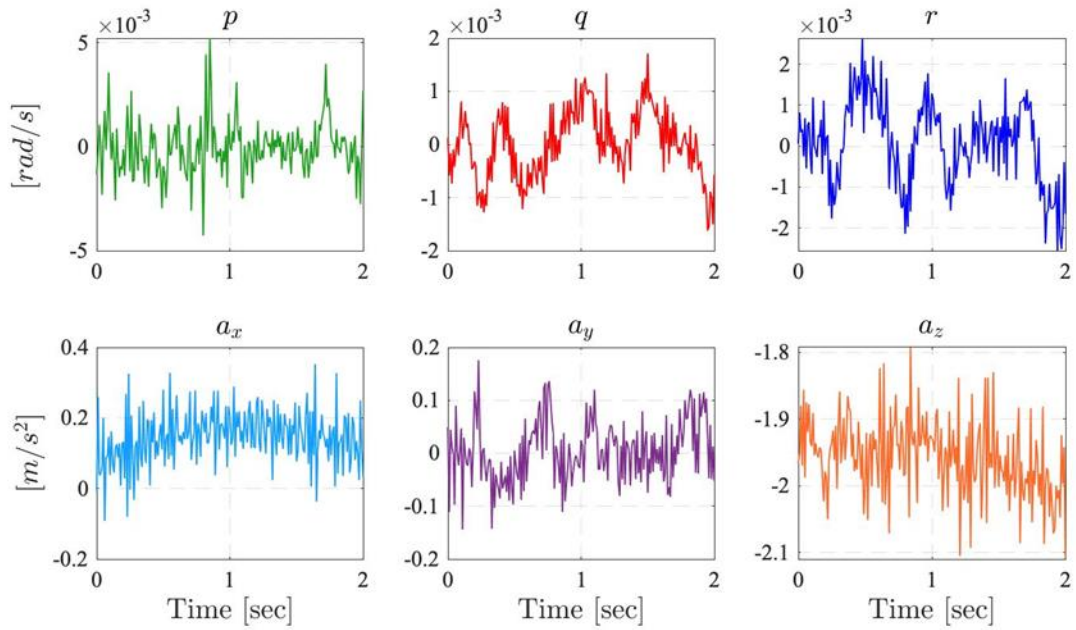


Figure 2.9: Base platform disturbance data (p, q, r, a_x, a_y, a_z)

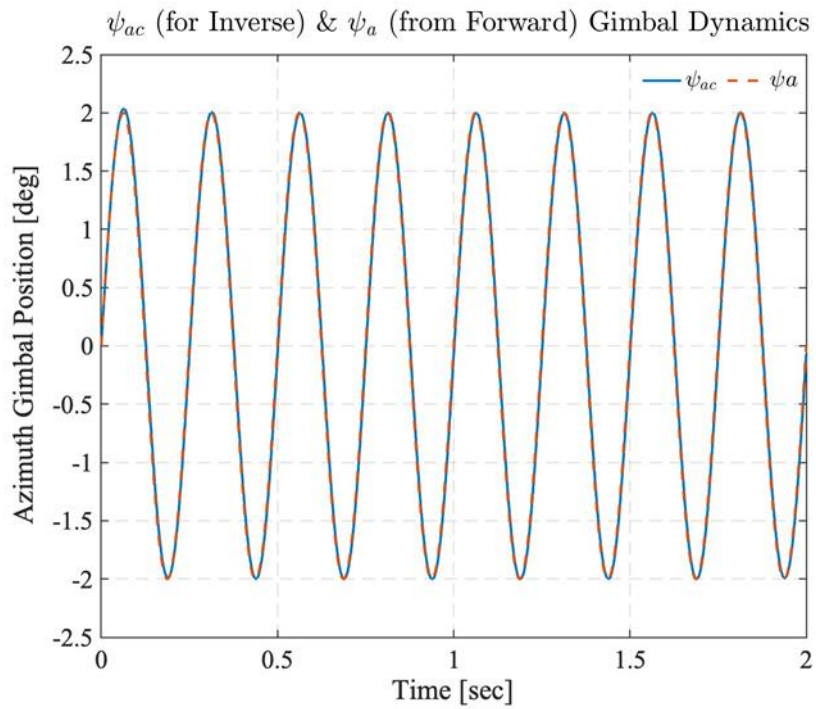


Figure 2.10: Yaw gimbal's commanded position input for the *Inverse Dynamics*, ψ_{ac} , and the position output from the *Forward Dynamics*, ψ_a

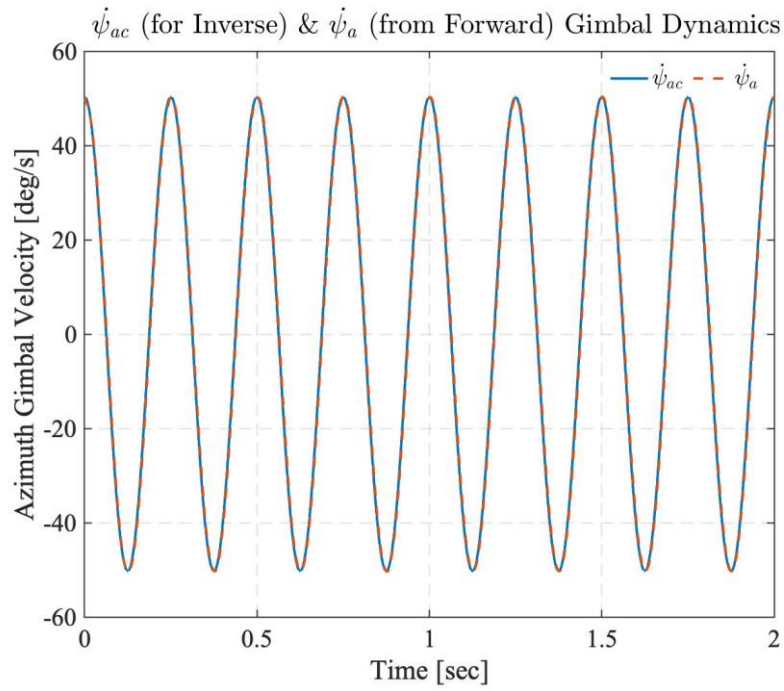


Figure 2.11: Yaw gimbal's commanded velocity input for the *Inverse Dynamics*, $\dot{\psi}_{ac}$, and the velocity output from the *Forward Dynamics*, $\dot{\psi}_a$

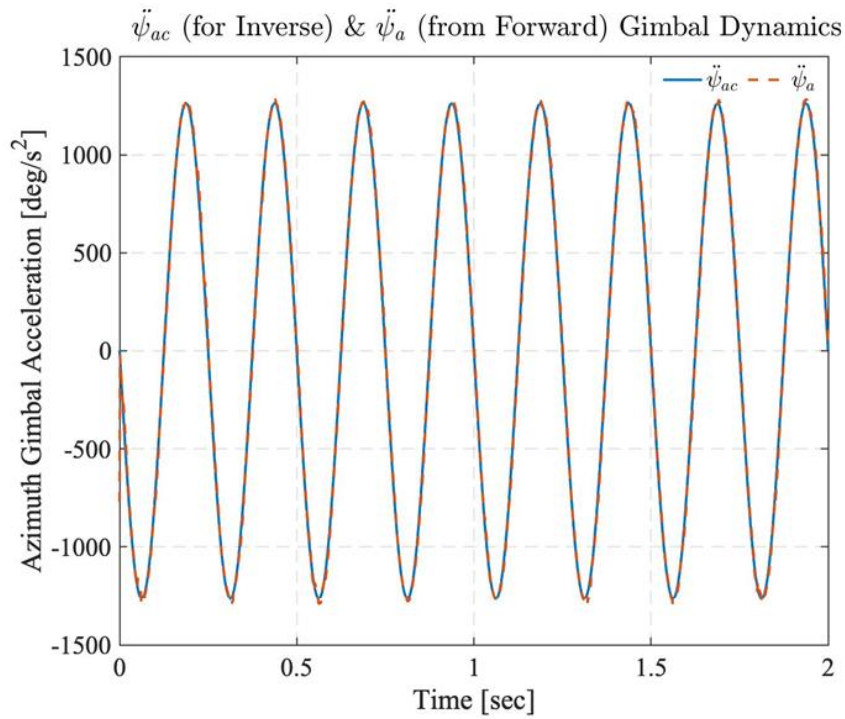


Figure 2.12: Yaw gimbal's commanded acceleration input for the *Inverse Dynamics*, $\ddot{\psi}_{ac}$, and the acceleration output from the *Forward Dynamics*, $\ddot{\psi}_a$

In Fig. 2.13 simulation results are given for the z-component of the reaction moment on the revolute joint in between the inner and the outer gimbals of the two-axis gimbal, i.e., M_{amz} , generated from *Inverse* and *Forward Dynamics* models. In Fig. 2.14, simulation results are given for the x-component of the reaction force on the revolute joint in between base platform and the outer gimbal of the system, i.e., F_{abx} , generated from *Inverse* and *Forward Dynamics* models.

The structure given in Fig. 2.8 is the representation of a **double integral plant**. If there exist different disturbances in *Inverse* and *Forward Dynamics*, (in terms of base platform motion, friction torque, model parameter uncertainties), **double integral structure** no longer exists. The inputs of the *Inverse Dynamics* and the outputs of the *Forward Dynamics*, reaction forces and moments calculated from *Inverse* and *Forward Dynamics* will not be the same anymore (Fig. 2.15).

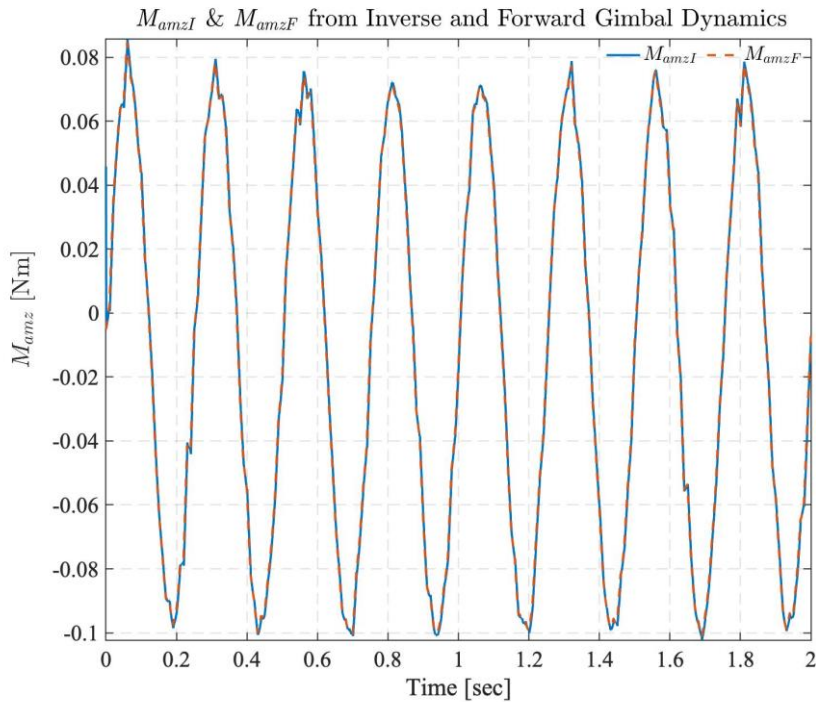


Figure 2.13: z-component of $\bar{M}_{a/m}^{(a)}$ calculated from *Inverse* and *Forward Dynamics* model

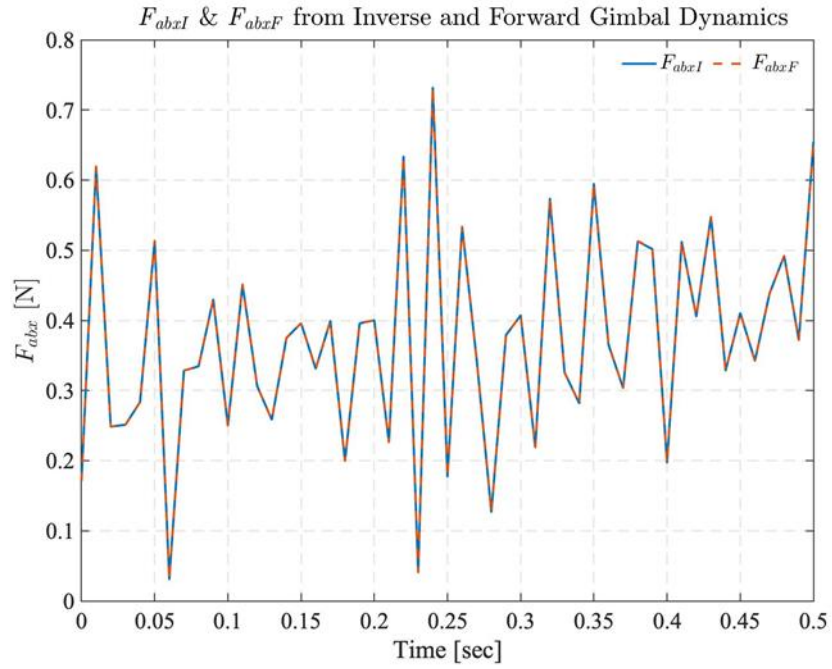


Figure 2.14: x-component of $\bar{F}_{a/b}^{(a)}$ calculated from *Inverse* and *Forward Dynamics* model

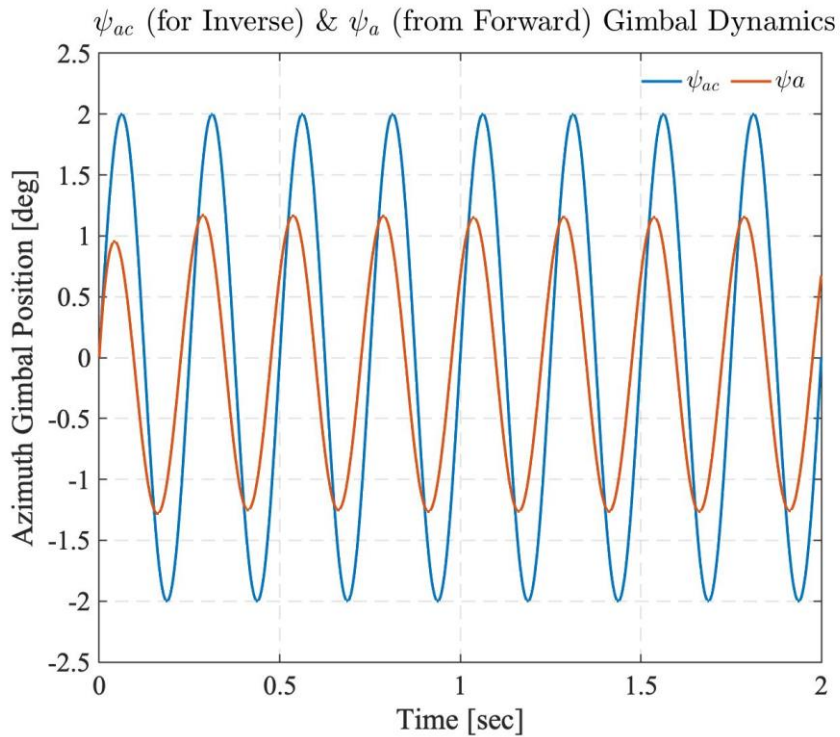


Figure 2.15: Yaw gimbal's commanded position input for the *Inverse Dynamics*, ψ_{ac} , and the position output from the *Forward Dynamics*, ψ_a under different disturbances

MEMS gyroscope installed in the inner ring, measures the velocity of the elevation gimbal ($\bar{\omega}_{m/o}^{(m)}$) in two directions, y and z axes, (corresponding velocities are q_m and r_m) with respect to inertial reference frame, F_o . q_m and r_m are defined as task velocities, $\dot{\theta}_m$ and $\dot{\psi}_a$ are defined as joint velocities. Conversions between joint-to-task velocities are given in Eqns. 2.32 and 2.33. When there is no base disturbance, q_m is equal to $\dot{\theta}_m$. However, r_m is not equal to $\dot{\psi}_a$. There needs to be a kinematic conversion in order to reach $\dot{\psi}_a$ from r_m . Since the difference between $\dot{\psi}_a$ and r_m is very small even for large values of θ_m (Fig. 2.16), r_m is treated as $\dot{\psi}_a$ in most of the applications. In this thesis, during experimental studies, r_m is used as $\dot{\psi}_a$.

$$q_m = -\sin(\psi_a) p + \sin(\psi_a) q + \dot{\theta}_m \quad (2.32)$$

$$r_m = \sin(\theta_m) [\cos(\psi_a) p + \sin(\psi_a) q] + \cos(\theta_m)[r + \dot{\psi}_a] \quad (2.33)$$

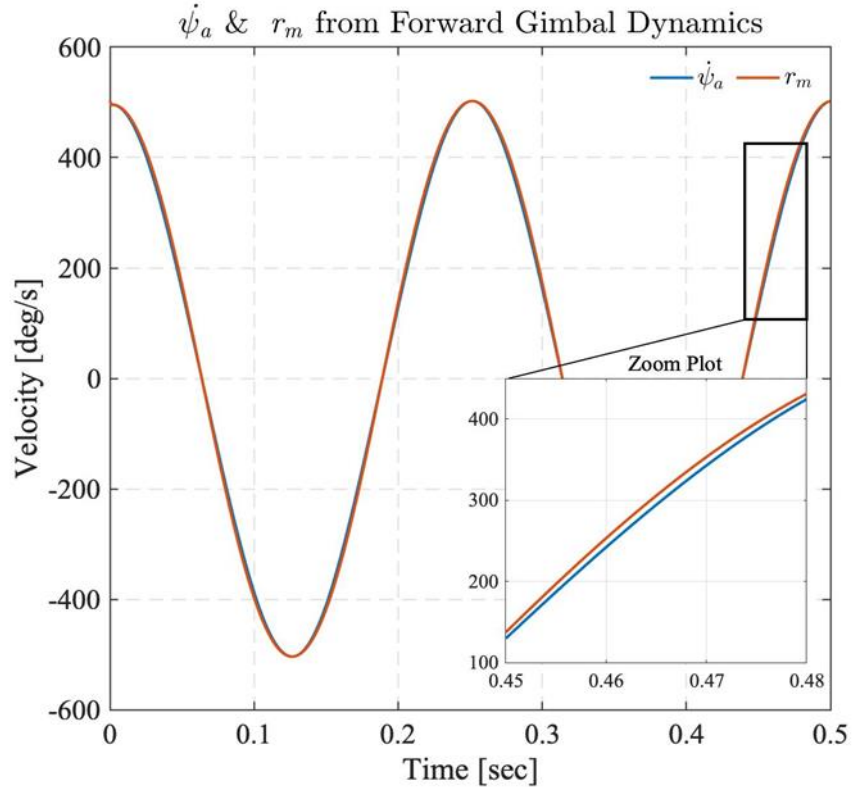


Figure 2.16: Plot showing the difference between $\dot{\psi}_a$ and r_m plotted for the position command of *Inverse Dynamics*, 20° @4Hz

Chapter 3

Test Set-Up and Experimental Data Collection

The experimental set-up is shown in Figure 3.1. It is composed of a 2-DoF gimbal that is mounted on a Stewart platform with the red fixture, a data acquisition (DAQ) system (xPC Target and Simulink®), a host PC, gimbal electronic card box (including power, gimbal motor driving and image processing cards) and a power supply. Host PC and target PC communicate via the ethernet communication protocol.

During the experiments, torque inputs T_{ac} and T_{ec} (i.e., voltage inputs of motors) are provided to the gimbal at a rate of 1kHz. The output of the quartz MEMS gyroscope (r_m, q_m) and of the encoders (ψ_a, θ_m) are measured at 1 kHz rate. The algorithm embedded in the gimbal driver runs at 5kHz. The output vector is $\bar{y} = [\psi_a, \theta_m, r_m, q_m]^T$. Base platform is hold stationary to simplify the experimental studies. Distance parameters, mass and inertia matrices are obtained from the 3D CAD drawing in Catia v5-3DX, R2021, [36]. The values of the distances are given

in Table 3.1. The parameters associated with the gimbal platform are given in Tables 3.2 and 3.3 for azimuth and elevation gimbals, respectively. While calculating inertia and mass values, inner and outer gimbals are taken as separate rigid bodies. Motor parameters are taken from the datasheets of inner and outer gimbal motors.

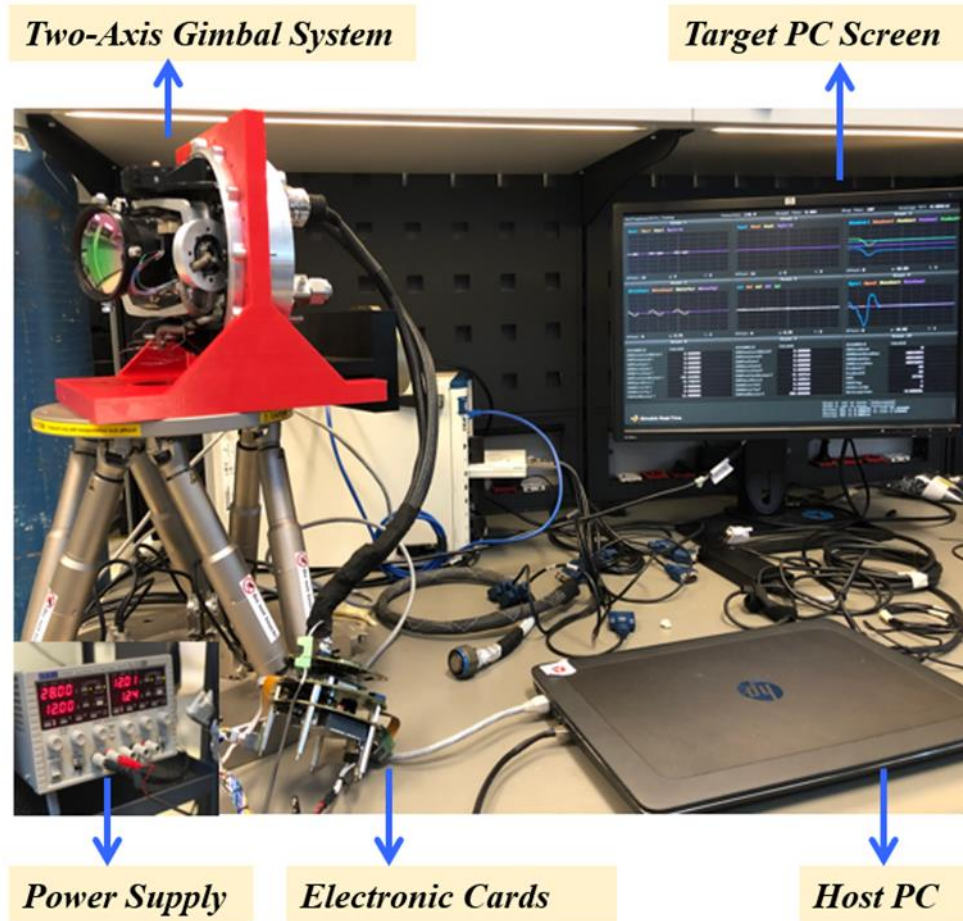


Figure 3.1: The experimental set-up of the two-axis gimbal system

Table 3.1: Distances of the gimbal platform

<i>Distances (in mm)</i>	<i>Yaw Gimbal</i>
$\bar{\mathbf{r}}_{Ga/a}^{(a)} = [Ga_x Ga_y Ga_z]^T$	$[0 \ 0 \ 57.5]^T$
$\bar{\mathbf{r}}_{Gm/m}^{(m)} = [Gm_x Gm_y Gm_z]^T$	$[0 \ -44.5 \ 0]^T$
$\bar{\mathbf{r}}_{m/a}^{(a)} = [am_x am_y am_z]^T$	$[0 \ 44.5 \ 57.5]^T$
$\bar{\mathbf{r}}_{a/b}^{(b)} = [ba_x ba_y ba_z]^T$	$[31.625 \ 0 \ -57.5]^T$

Table 3.2: Parameters of the yaw gimbal

<i>Brushless DC Motor Parameters</i>	<i>Yaw Gimbal</i>
K_t (Nm/Amp)	0.0615
K_b (V/(rad/s))	0.0616
R (Ω)	1.42
L (mH)	0.67
b (Nm/(rad/s))	2.15×10^{-5}
<i>Gimbal Platform Parameters</i>	
m (kg)	0.555
$\hat{\mathbf{j}}$ (kgm ²)	$\begin{bmatrix} 0.002 & -3.089 \times 10^{-6} & 2.505 \times 10^{-5} \\ -3.089 \times 10^{-6} & 0.004 & 3.17 \times 10^{-6} \\ 2.505 \times 10^{-5} & 3.17 \times 10^{-6} & 0.002 \end{bmatrix}$
FOR (field of regard) limits	$\pm 45^\circ$

Table 3.3: Parameters of the pitch gimbal

<i>Brushless DC Motor Parameters</i>	<i>Pitch Gimbal</i>
K_t (Nm/Amp)	0.036
K_b (V/(rad/s))	0.0359
R (Ω)	1.31
L (mH)	0.48
b (Nm/(rad/s))	10.45×10^{-6}
<i>Gimbal Platform Parameters</i>	
m (kg)	1.138
\hat{J} (kgm ²)	$\begin{bmatrix} 0.004 & 9.157 \times 10^{-6} & 1.418 \times 10^{-5} \\ 9.157 \times 10^{-6} & 0.003 & -1.355 \times 10^{-4} \\ 1.418 \times 10^{-5} & -1.355 \times 10^{-4} & 0.004 \end{bmatrix}$
FOR (field of regard) limits	$\pm 20^\circ$

3.1 Implementation of Inverse Dynamics Model in the Experimental Set-Up

In Chapter 2, open loop structure of *Inverse* and *Forward Gimbal Dynamics* of the proposed two-axis gimbal system is simulated with MATLAB® and Simulink® software. In this section, implementation of *Inverse Gimbal Dynamics* in Simulink® Real-Time (xPC Target) is discussed. Experimental set-up is used as the *Forward Gimbal Dynamics* to form the open loop structure with the *Real Plant*. The aim of this study is to observe the open loop response of the *Real Plant*.

Since, disturbances present in the *Real Plant* are unknown at the moment, *Ideal Inverse Gimbal Dynamics* is used in xPC Target. *Ideal Inverse Gimbal Dynamics* implies that there is no friction torque present in the revolute joint between the outer

ring and the base platform (T_{fra}) and in the revolute joint between the inner and outer rings of the 2-DoF gimbal assembly (T_{frm}). There are no off-diagonal inertia parameters (or off-diagonal terms are very small compared to diagonal terms), rotation axis and CoG offsets, as well. Open loop block diagram of the *Ideal Inverse Gimbal Dynamics-Real Plant* structure is given in Fig. 3.2.

Commanded acceleration ($\ddot{\bar{r}}_d$), velocity ($\dot{\bar{r}}_d$) and position (\bar{r}_d) are the inputs for *Ideal Inverse Gimbal Dynamics* (Eqns. 3.1, 3.2, 3.3). The output of the *Inverse Gimbal Dynamics* block, is the required torque (\bar{u}_d) needed to perform the commanded motion for an ideal system (Eqn. 3.4). Real plant outputs are encoder and gyro data (\bar{r} , $\dot{\bar{r}}$). In order to derive the acceleration input, $\ddot{\bar{r}}$, a backwards derivative operation at every 10 data point is performed for the gyro data (Eqns. 3.5, 3.6, 3.7) in xPC Target. Real plant input is the voltage, \bar{V}_c .

Different from the experiments carried out in Chapter 2, in this chapter, commanded position, velocity and acceleration inputs for the *Ideal Inverse Gimbal Dynamics* are not same as the position, velocity and acceleration outputs of the *Real Plant* (*Real Plant* is not ideal, there are complex and nonlinear disturbances).

Equations 3.1-3.7 are listed below:

$$\ddot{\bar{r}}_d = [\ddot{\psi}_{ac} \quad \ddot{\theta}_{mc}]^T \quad (3.1)$$

$$\dot{\bar{r}}_d = [\dot{\psi}_{ac} \quad \dot{\theta}_{mc}]^T \quad (3.2)$$

$$\bar{r}_d = [\psi_{ac} \quad \theta_{mc}]^T \quad (3.3)$$

$$\bar{u}_d = [T_{ac} \quad T_{mc}]^T \quad (3.4)$$

$$\ddot{\bar{r}} = [\ddot{\psi}_a \quad \ddot{\theta}_m]^T \quad (3.5)$$

$$\dot{\bar{r}} = [\dot{\psi}_a \quad \dot{\theta}_m]^T \quad (3.6)$$

$$\bar{r} = [\psi_a \quad \theta_m]^T \quad (3.7)$$

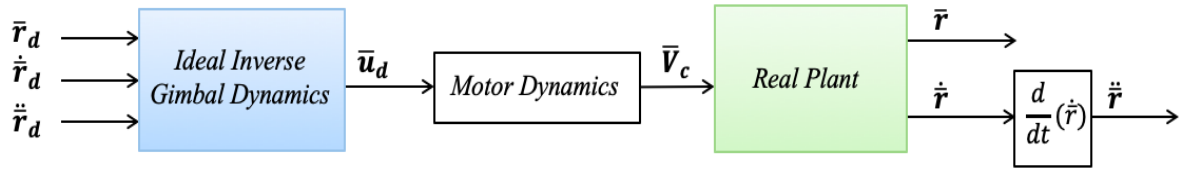


Figure 3.2: Open loop block diagram used in xPC Target for obtaining *Real Plant* outputs

In Figure 3.2, there is Motor Dynamics block between *Ideal Inverse Gimbal Dynamics* and *Real Plant*. It is Torque to Voltage (T2V) conversion with the motor parameters given separately for pitch and yaw gimbal motors in Tables 3.1 and 3.2. Block diagram representation of the Motor Dynamics is shown for a single-axis gimbal in Fig. 3.3. R, L and K_t are the motor parameters. u_d is the torque, i_c is the current and V_c is the voltage applied to the motor. Current saturation blocks ($\pm 10A$), are used to limit the motor current. Output torque of the *Ideal Inverse Gimbal Dynamics* is converted to current. Command filtering, [37] is used to find the derivative of the current. This shaping filter is used to find the derivative; because current signal in the experiment is noisy. The bandwidth of the command filter is selected as 100 Hz for both pitch and yaw gimbals, $w_n = 100 \times 2\pi \text{ rad/s}$.

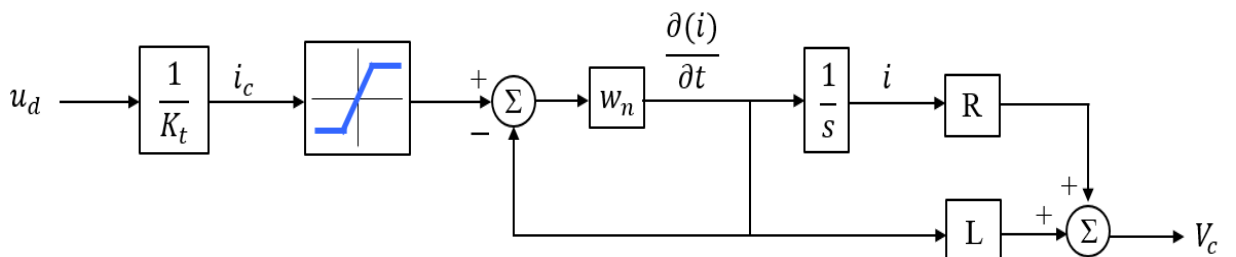


Figure 3.3: Block diagram representation of the *Motor Dynamics* used in xPC Target (Torque to Voltage conversion)

Open loop position response of the system for four different inputs sets are given in Figs. 3.4, 3.5, 3.6 and 3.7. The reference input sets corresponding to azimuth and elevation gimbals for each experiment are given in Table 3.3. At each experiment, azimuth and elevation gimbals are excited with the sinusoidal waves regarding to that experiment simultaneously.

Table 3.4: Azimuth and elevation gimbal Reference Sets used in Chapter 3

	Azimuth Gimbal	Elevation Gimbal
Reference Set 1	10°@ 2Hz sine	7°@ 2Hz sine
Reference Set 2	10°@ 1.5Hz sine	7°@ 2Hz sine
Reference Set 3	2°@ 4Hz sine	9°@ 3Hz sine
Reference Set 4	3°@ 5Hz sine	5°@ 3Hz sine

In the first experiment, reference positions are 10° and 7°@ 2Hz sinusoidal waves for azimuth and elevation gimbals, respectively. In the second experiment, only the frequency of the azimuth gimbal is changed to 1.5 Hz. This small change, affected the oscillation behaviour of both elevation and azimuth gimbals (Figs. 3.4 and 3.5). This example proves that system is *coupled*.

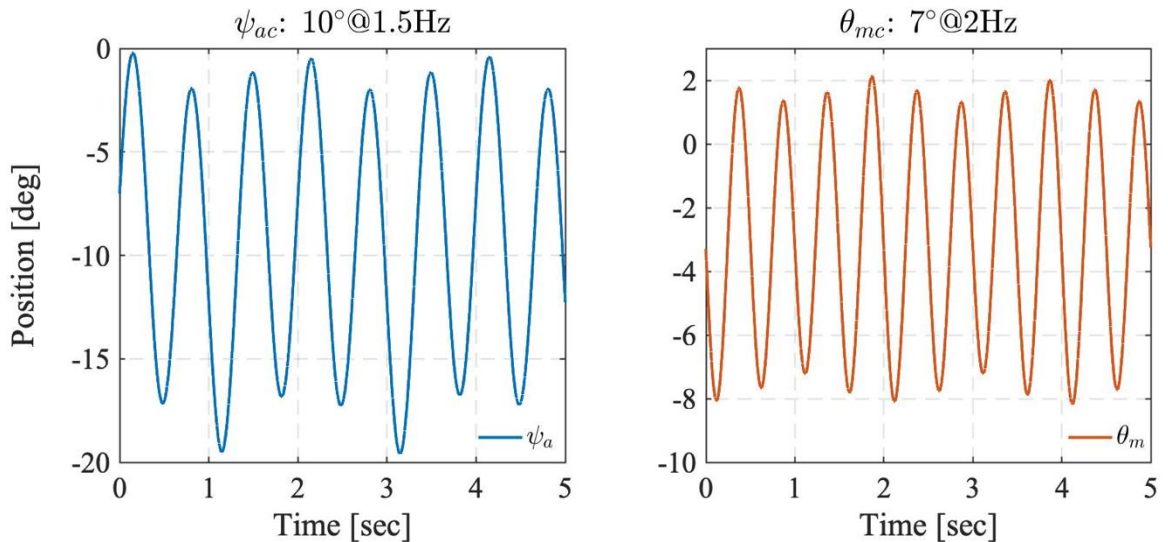


Figure 3.4: Open loop response of the system for Reference Set 1

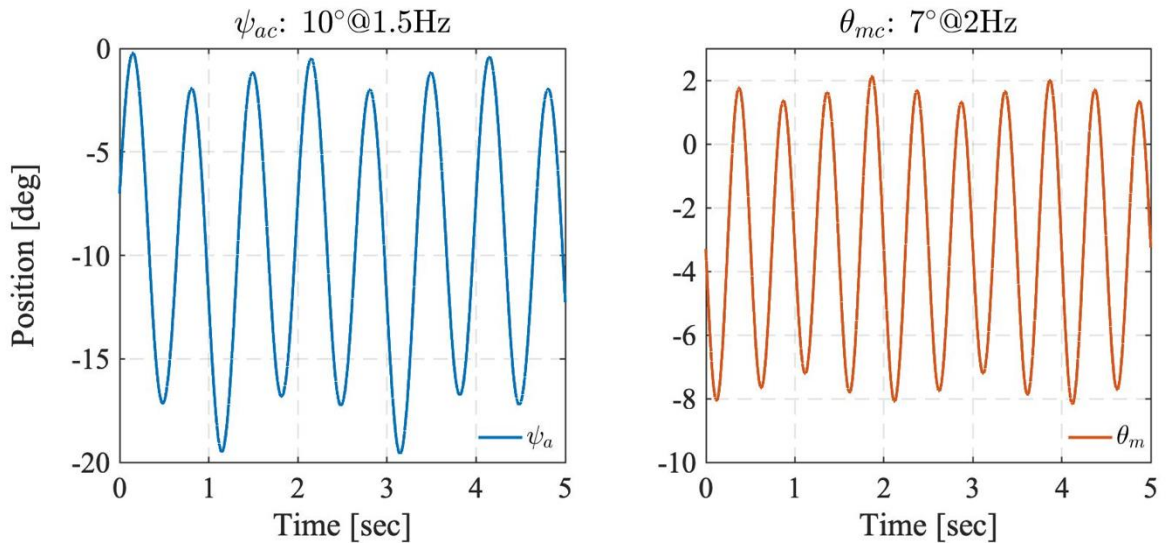


Figure 3.5: Open loop response of the system for Reference Set 2

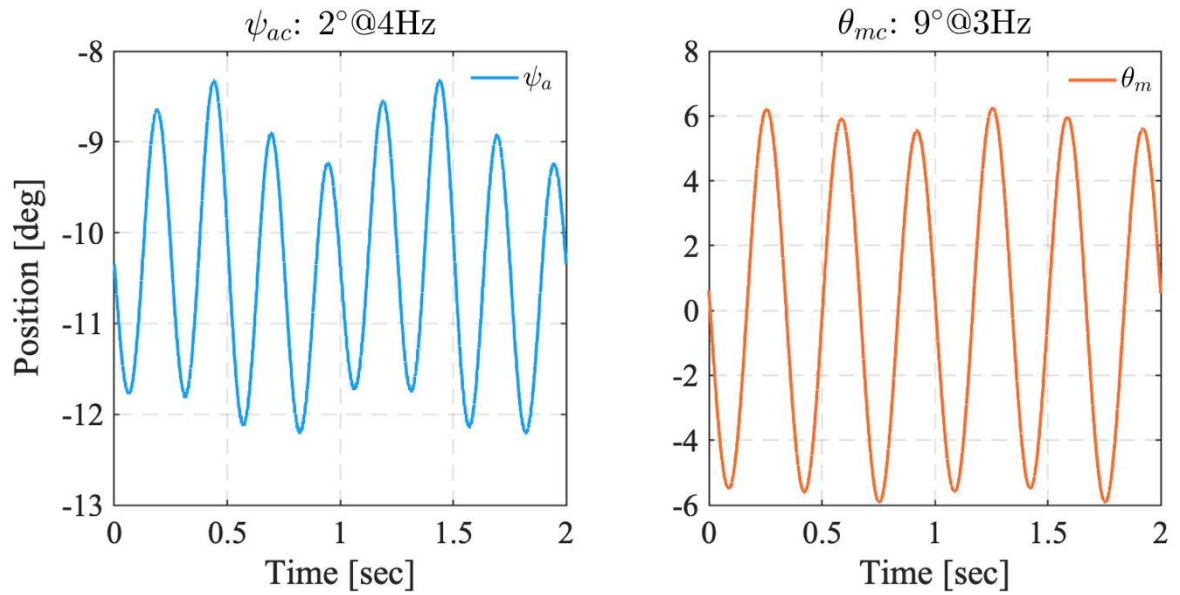


Figure 3.6: Open loop response of the system for Reference Set 3

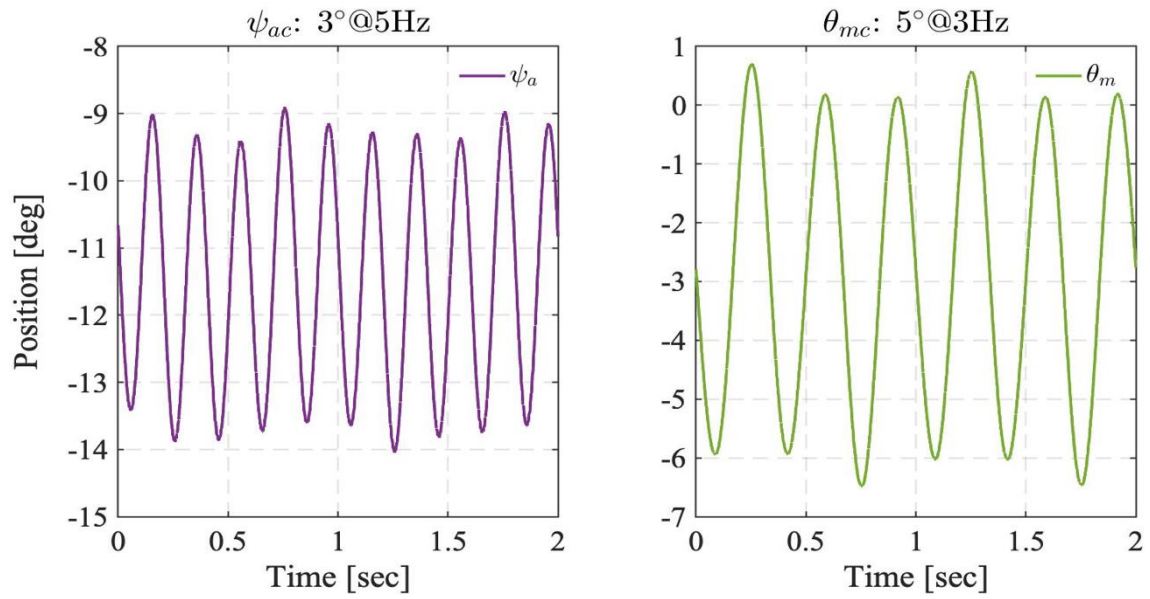


Figure 3.7: Open loop response of the System for Reference Set 4

It has been observed that, response of the system changes under different sinusoidal inputs (i.e., system produces different oscillation patterns in position and velocity). Response of the system is different for different commanded inputs with different frequencies. Real setup is a nonlinear system; different oscillation patterns are expected when the system is excited with different frequency inputs for elevation and azimuth gimbals. However, the effect of coupling and cable restraint torques should also be considered with the nonlinearity of the system while commenting on the response. Response obtained from the *Real Plant* is different compared to commandad inputs for the *Ideal Inverse Dynamics* in terms of magnitude and shape. Due to disturbance torques, *Real Plant* cannot catch the magnitude of the sinusoidal reference, does not oscillate around 0° and attain a different shape from a sine wave. This is the main reason why it is important to investigate the disturbance torque present in the system. This is done in Chapter 5 by using disturbance torque estimation from the *Real Plant* with Approaches 1 and 2.

Chapter 4

Parameter Sensitivity Analysis

As mentioned earlier, the mathematical model for a two-axis gimbal system presented in the previous sections have several more parameters, when compared to the dynamical models in literature. Hence, in this section, influences of all of the parameters associated with the dynamical behavior of the system are investigated by *Sensitivity Analysis*. The sensitivity analysis is performed by using the results of *Monte Carlo Simulations* (MCS), [38].

In the sensitivity analysis, at the start of each simulation, different values for the off-set distances, $\bar{d} = [am_x \ Ga_y \ Ga_x \ Gm_z \ Gm_x]^T$, off-diagonal terms in the inertia matrices, $\bar{J}_a = [J_{axy} \ J_{axz} \ J_{ayx} \ J_{ayz} \ J_{azx} \ J_{azy}]^T$, $\bar{J}_m = [J_{mxy} \ J_{mxz} \ J_{myx} \ J_{myz} \ J_{mzx} \ J_{mzy}]^T$ and the disturbance torques on the revolute joints, T_{fra} , T_{frm} are chosen from a sequence of random variables, i.e., a stationary stochastic process.

In this part, for sake of simplicity, it is assumed that, only viscous friction is responsible to generate the disturbance torques, i.e., $T_{fra} = -b_a \dot{\psi}_a$, $T_{frm} = -b_e \dot{\theta}_m$, with $\bar{b} = [b_a \ b_e]^T$. Also, moment of inertia tensors of pitch and yaw gimbals are assumed to be symmetric, i.e., $J_{axz} = J_{azx}$, and similar for the other off-diagonal elements. Moreover, base disturbance is not included in the MCS's. Sensitivity analysis is performed for the gimbal system with the distance and inertia parameters given in Chapter 3. The initial choice for viscous friction parameters is taken as $[0.08 \ 0.08]^T$.

Inverse Gimbal Dynamics is used to observe the influence of \bar{b} , \bar{d} , \bar{J}_a and \bar{J}_m vectors on the commanded torques, reaction forces and moments. Input for the inverse model is arranged so that the commanded torques, reaction moments and forces are constant (time invariant vectors are required). Both, pitch and yaw gimbals reach to their FOR limits (18° and 42°) linearly, with constant velocity and zero acceleration inputs in 1 second.

By setting all parameters to zero (\bar{b} , \bar{d} , \bar{J}_a and \bar{J}_m), nominal outputs are obtained from the inverse model and they are recorded to be used at each MCS. Nominal outputs describe the ideal situation. It is the case for which:

1. There are no CoG and off-axis offsets ($\bar{d} = \bar{0}$).
2. There are no off-diagonal terms in the inertia matrices ($\bar{J}_a, \bar{J}_m = \bar{0}$).
3. There are no frictional disturbances ($\bar{b} = \bar{0}$).

Fig. 4.1 shows the block diagram of the *Inverse Gimbal Dynamics*, which is used to obtain the nominal output vector \bar{Y}_N .

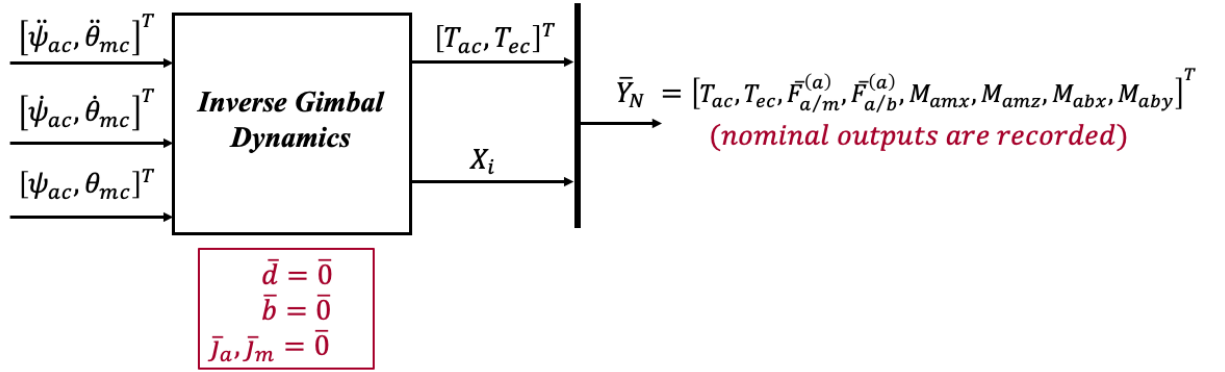


Figure 4.1: Block diagram of the *Inverse Gimbal Dynamics* used for nominal outputs

Three different MCSs ($N = 100$ is the number of simulations) are performed with MATLAB® so that effect of each non-ideal situation can be observed separately:

1. First simulation is done for observing the effects of distance parameters. The only disturbance present in the *Inverse Gimbal Dynamics* is the CoG and off-axis offsets.
2. Second simulation is done for observing the effects of viscous friction coefficients. The only disturbance present in the *Inverse Gimbal Dynamics* is the friction.
3. Third simulation is done for observing the effects of off-diagonal inertia parameters. The only disturbance present in the *Inverse Gimbal Dynamics* is the cross-coupling torque caused by inertia matrices.

4.1 First MCS: Effects of Distance Parameters

In the first MCS, viscous friction coefficients and off-diagonal inertia values are set to zero and distances are varied based on the Gaussian distribution with zero mean and 0.005 standard deviation.

Difference of outputs from the inverse model corresponding to random distance values \bar{Y} and nominal outputs \bar{Y}_N is denoted by $\bar{\Delta}_{out}$. Cross-correlation matrix between \bar{d} and $\bar{\Delta}_{out}$ is formed. Block diagram representation of the system used to obtain this matrix is given in Fig. 4.2.

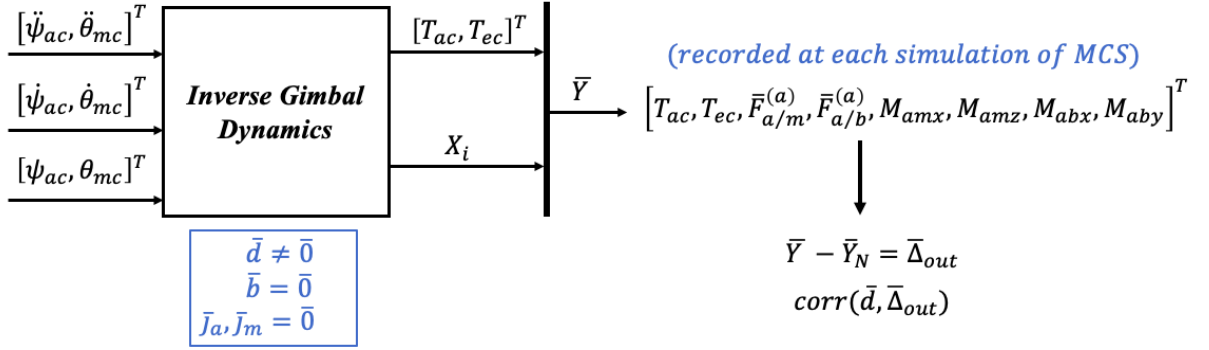


Figure 4.2: Block diagram of the *Inverse Gimbal Dynamics* in the first MCS

Correlation matrix has a dimension of 5x12, rows representing \bar{d} and columns representing $\bar{\Delta}_{out}$. Elements of the cross-correlation matrix formed between \bar{d} and $\bar{\Delta}_{out}$ is given in Appendix A, Table A.1. Significant elements of the cross-correlation matrix related with the distance parameters, am_x , Gm_z , Ga_y , Gm_x are given in Tables 4.1, 4.2, 4.3 and 4.4, respectively.

Elements of the matrix of p-values, indicating the existence of the relationship between \bar{d} and $\bar{\Delta}_{out}$ is given in Appendix A, Table A.2. If p-values are smaller than 0.05, elements of \bar{d} and $\bar{\Delta}_{out}$ are related, [39].

Table 4.1: Significant correlation coefficients related with am_x

\ddots	T_e	F_{amx}	F_{abx}	M_{aby}
a_{mx}	-0.99	0.687	-0.631	-0.639

Observations from Table 4.1 are explained below:

- There is a highly negative correlation (-0.99) between T_e and am_x . Among all the disturbed distance parameters ($am_x, Ga_y, Ga_x, Gm_z, Gm_x$), the correlation between am_x and T_e is the greatest.
- When am_x value is different than zero, F_{amx} increases. This is supported by the positive correlation coefficient between am_x and F_{amx} (0.687).
- According to EoMs of the system derived in Chapter 2, $F_{amx} = -F_{abx}$ when the base platform is stationary. Thus, F_{abx} increases in the opposite direction of F_{amx} , as F_{amx} increases. This indicates the negative correlation between am_x and F_{abx} (-0.631).
- In return, M_{aby} also increases caused by the moment generated by F_{abx} wrt. the pivot point. This explains the negative correlation coefficient between M_{aby} and am_x (-0.639). The increase in M_{aby} induces an increase in T_e in the same direction.
- From a different view, x-axis offset causes the pitch gimbal to have an extra pitching motion with respect to (wrt.) the pivot point. T_e should be applied in the opposite direction to the moment generated by the am_x distance in order to compensate its effect.

Table 4.2: Significant correlation coefficients related with Gm_z

\therefore	F_{amz}	F_{abz}
Gm_z	0.99	-0.99

Observations from Table 4.2 are explained below:

- There is a highly positive correlation (0.99) between Gm_z and F_{amz} . Increase in F_{amz} will induce an increase in F_{abz} in the opposite direction. There is a negative correlation between F_{abz} and Gm_z (-0.99). According to equations

derived in Chapter 2, $-F_{amz} - F_{abz} = m_a \bar{g}_a$, when the base platform is stationary. This proves the negative relation between F_{amz} and F_{abz} . F_{amz} and F_{abz} are related with Gm_z the most, compared to other distance parameters.

Table 4.3: Significant correlation coefficients related with Ga_y

\therefore	M_{abx}
G_{ay}	0.5

Observations from Table 4.3 are explained below:

- There is a positive correlation (0.5) between Ga_y and M_{abx} . When the CoG point of the outer ring has a distance to x_a axis, there will be a rolling moment for the yaw gimbal.

Table 4.4: Significant correlation coefficients related with Gm_x

\therefore	F_{amx}	F_{abx}	M_{aby}
G_{mx}	0.69	-0.68	-0.664

Observations from Table 4.4 are explained below:

- Changing Gm_x affects F_{amx} (correlation coefficient is 0.69), which, in return affects F_{abx} in the opposite direction (correlation coefficient is -0.68). It also, causes a pitching moment around the pivot point that affects the yaw gimbal. There is a highly negative correlation between Gm_x and M_{aby} (-0.664). This is an example of a coupled system, center of gravity position of the pitch gimbal affects the reaction moment appearing at the revolute joint between yaw gimbal and the base platform.

Fig. 4.3 shows the changes in T_e , Fig. 4.4 shows the changes in F_{amx} and Fig. 4.5 shows the changes in M_{amz} at each simulation of MCS due to changes in randomly distributed distance parameters.

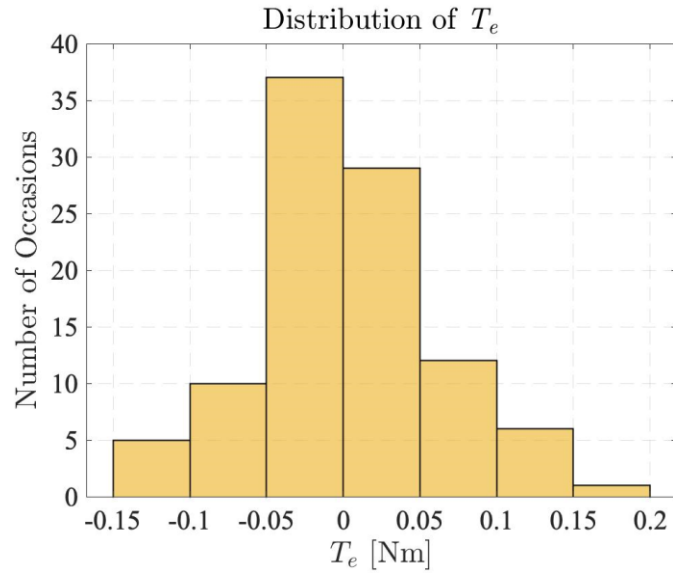


Figure 4.3: Distribution of T_e wrt. changes in distance parameters

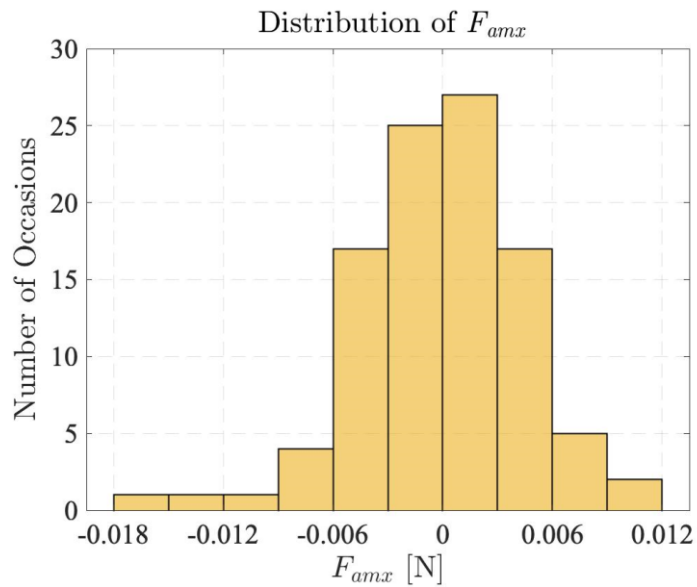


Figure 4.4: Distribution of F_{amx} wrt. changes in distance parameters

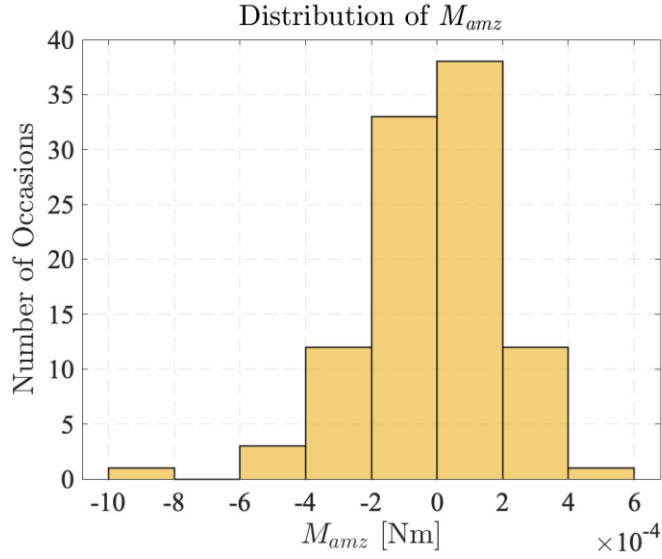


Figure 4.5: Distribution of M_{amz} wrt. changes in distance parameters

4.2 Second MCS: Effects of Viscous Friction Coefficients

In the second MCS, distance parameters and off-diagonal inertia values are set to zero and viscous friction coefficients are varied based on the Gaussian distribution function with 0.08 mean and 0.5 standard deviation.

Cross-correlation matrix (with dimensions 2x12) between \bar{b} and $\bar{\Delta}_{out}$ is formed. Block diagram representation of the system used to obtain this matrix is given in Fig. 4.6. Elements of the cross-correlation matrix formed between \bar{b} and $\bar{\Delta}_{out}$ is given in Appendix A, Table A.3. Significant elements of this correlation matrix are given in Table 4.5. Elements of the matrix of p-values between \bar{b} and $\bar{\Delta}_{out}$ is given in Appendix A, Table A.4.

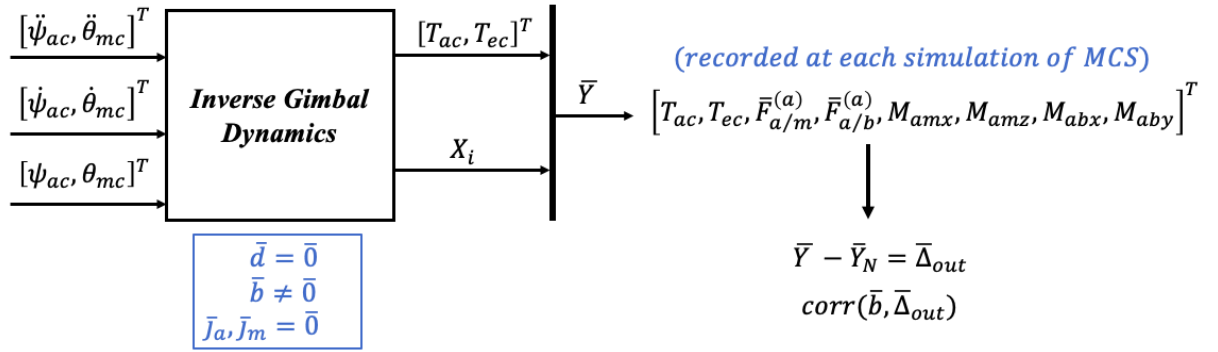


Figure 4.6: Block diagram of the *Inverse Gimbal Dynamics* in the second MCS

Table 4.5: Significant correlation coefficients related with b_a and b_e

\ddots	T_a	T_e	F_{amx}	M_{amx}
b_a	1	-0.036	-0.051	-0.051
b_e	-0.036	1	0.008	0.008

It has been observed that:

- As expected, there is a positive correlation between T_a and b_a , T_e and b_e . The correlation coefficient is 1. Fig. 4.7, shows the changes in T_a at each simulation of MCS.
- There is no correlation between viscous friction coefficients and reaction forces, moments. Correlation coefficients are very low (it is around $|0.051|$ for b_a and $|0.008|$ for b_e for most forces & moments). Reaction forces and moments stay the same during each iteration of MCS.

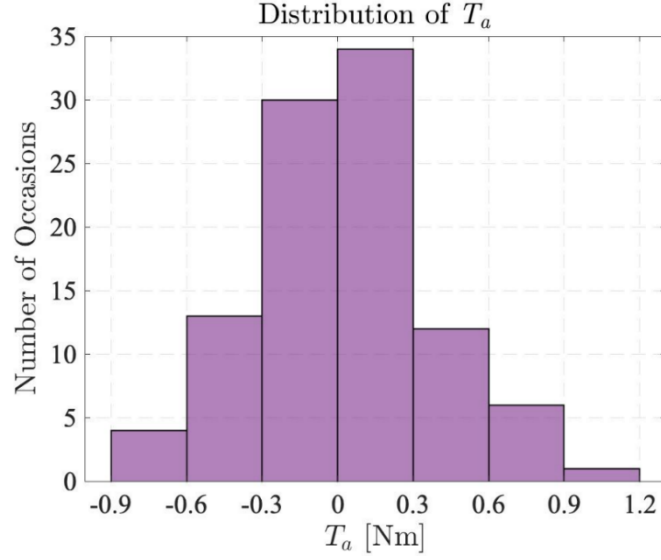


Figure 4.7: Distribution of T_a wrt. changes in friction coefficients

4.3 Third MCS: Effects of Off-Diagonal Inertia Terms

In the third MCS, distance parameters and friction coefficients are set to zero and off-diagonal terms in the inertia matrices are varied based on the Gaussian distribution function with 0.01 standard deviation and with mean values found from the 3D CAD model of the experimental set-up (given in Chapter 3).

Cross-correlation matrix (with dimensions 6x12) between $\bar{j} = [J_{axy} \ J_{axz} \ J_{ayz} \ J_{mxy} \ J_{mxz} \ J_{myz}]^T$ and $\bar{\Delta}_{out}$ is formed. Block diagram representation of the system used to obtain this matrix is given in Fig. 4.8. Elements of the cross-correlation matrix formed between \bar{j} and $\bar{\Delta}_{out}$ is given in Appendix A, Table A.5. Significant elements of the cross-correlation matrix related with the inertia parameters J_{mxz} , J_{mzx} , J_{myz} , J_{mzy} , J_{axz} , J_{azx} are given in Tables 4.6, 4.7 and 4.8, respectively. Elements of the matrix of p-values between \bar{j} and $\bar{\Delta}_{out}$ is given in Appendix A, Table A.6.

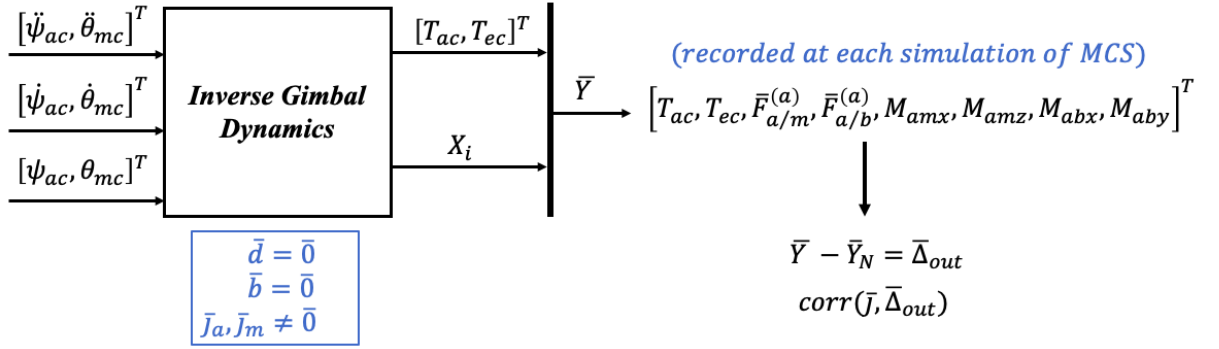


Figure 4.8: Block diagram of the *Inverse Gimbal Dynamics* in the third MCS

Figs. 4.9, 4.10 and 4.11 show the graph of T_e , M_{amx} and M_{aby} obtained after each iteration of MCS.

Table 4.6: Significant correlation coefficients related with $Jmxz$, $Jmzx$

	T_e	T_a
$Jmxz, Jmzx$	-0.99	-0.978

It has been observed from Table 4.6 that:

- There is a very high positive correlation between T_e and $Jmxz$, $Jmzx$. The correlation coefficient is 1. There is also a strong correlation between T_a and $Jmxz$, $Jmzx$. The correlation coefficient is -0.978. The QQ (quantile-quantile) plot given in Fig. 4.9, shows that T_e does not exactly follow a normal distribution. Only the points in the middle follow the straight line closely, points in the left-tile and right tiles deviate from it. This is the indication of having a nonlinear system. Inertia terms are varied based on a Gaussian distribution; but the outputs obtained after each iteration of MCS do not follow a Gaussian distribution (same comment is also valid for the QQ plot given in Fig. 4.10).

Table 4.7: Significant correlation coefficients related with J_{myz}, J_{mzy}

\ddots	M_{amx}	M_{amz}
J_{myz}, J_{mzy}	0.944	0.944

It has been observed from Table 4.7 that:

- Reaction forces are not affected from the changes in off-diagonal inertia terms (correlation coefficients are very small in Appendix A, Table A.5). On the other hand, reaction moments are highly influenced from the changes in inertia parameters. For instance, there exists a positive correlation between M_{amx}, M_{amz} and J_{myz}, J_{mzy} (0.944).

Table 4.8: Significant correlation coefficients related with J_{axz}, J_{azx}

\ddots	M_{aby}
J_{axz}, J_{azx}	0.747

It has been observed from Table 4.8 that:

- There exists a positive correlation between M_{aby} and J_{axz}, J_{azx} (0.747).

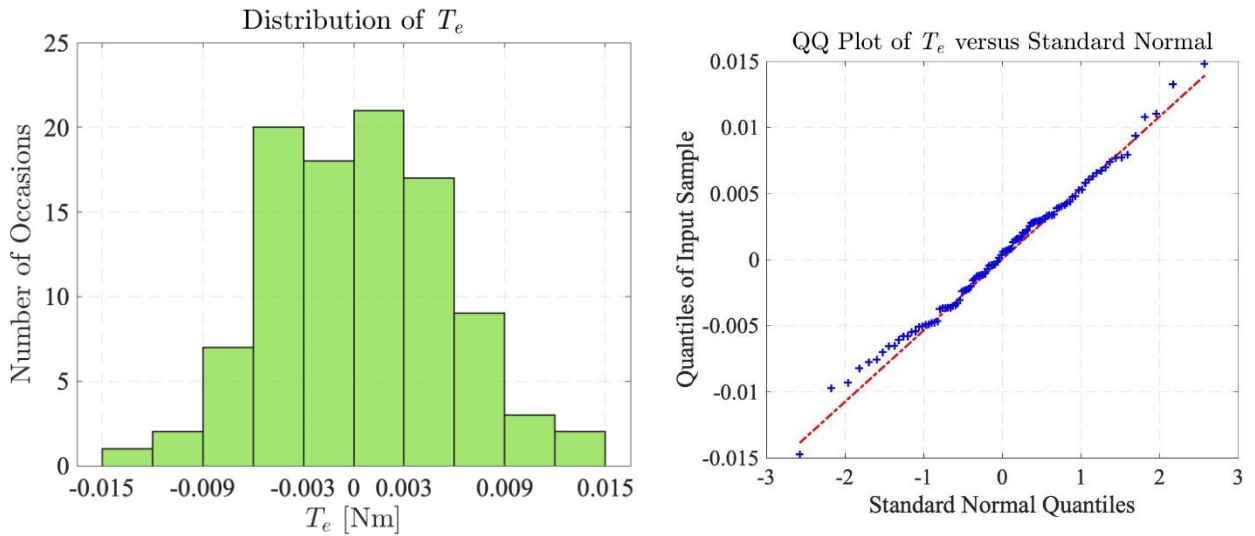


Figure 4.9: Distribution of T_e wrt. changes in inertia parameters and the QQ Plot

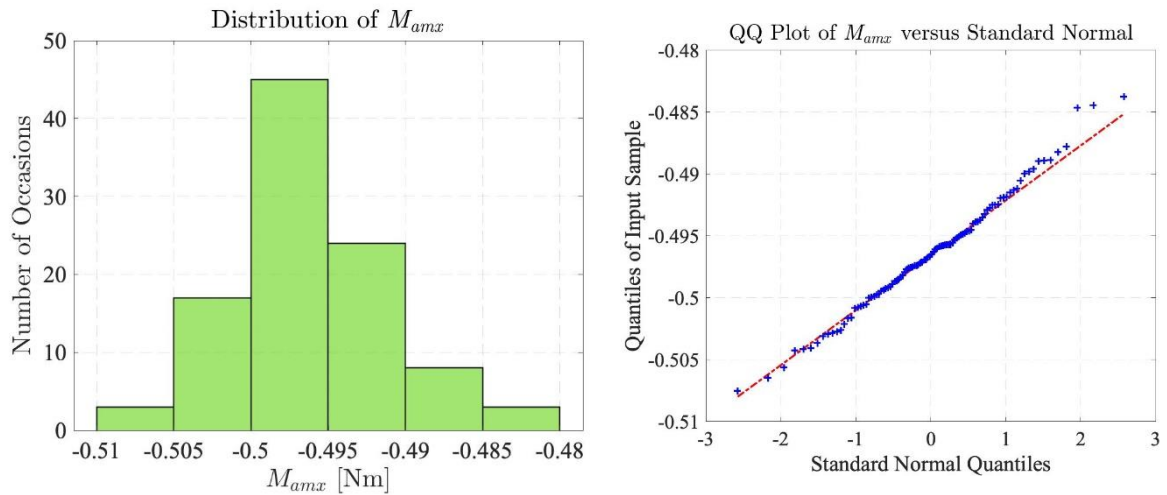


Figure 4.10: Distribution of M_{amx} wrt. changes in inertia parameters and the QQ Plot

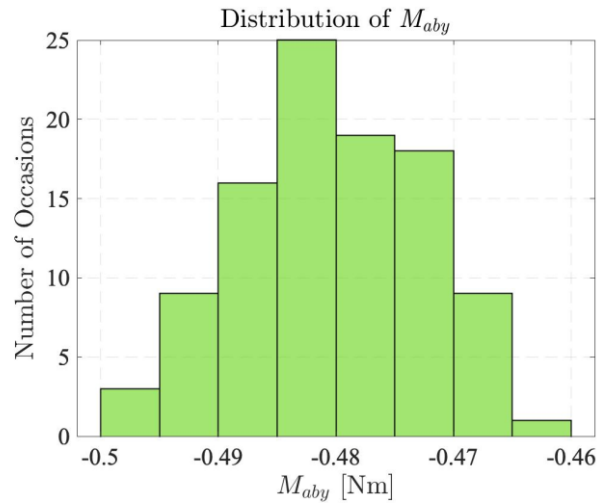


Figure 4.11: Distribution of M_{aby} wrt. changes in inertia parameters

Sensitivity analysis is performed to observe the behavior of commanded torques, reaction forces and moments corresponding to changes in distance, friction and inertia parameters. Results of this analysis shows that, distance parameters, off-diagonal inertia terms and viscous friction coefficients have a strong influence on the dynamical response of the system. Off-diagonal inertia parameters have no effect on the reaction forces, friction coefficients have no effect on the reaction forces and moments appearing at the revolute joints whereas changes in distance parameters have a strong effect both for reaction forces, moments and driving torques.

Chapter 5

Disturbance Torque Estimation Study Using the Experimental Set-Up

In order to decide on the control strategy that will be applied for the real plant, it is important to understand the nature of the disturbance torque. Real system is under the effect of external and internal nonlinear disturbances primarily caused by:

1. The friction torques on the revolute joints,
2. The disturbance torques as a result of model uncertainties (CoG and rotation axis offsets, off-diagonal inertia parameters),
3. The disturbance torques as a result of the electrical cables of motors, encoders/resolvers, gyroscope, camera and cooling pipes of the sensor system.

In this study, series of experiments are conducted to understand the behaviour of the overall disturbance torque and its dependency on system parameters and states.

5.1 Approach 1: Disturbance Torque (Trimming Torque) Estimation by Using the Stabilization Loop

This section is based on performing constant velocity experiments over the stabilization loop of the gimbal system. When the velocity of azimuth and elevation gimbals are constant, torque produced by the motors are only used to overcome the opposing disturbance torques (i.e., this can be proven by providing ramp input as the reference position, constant velocity and zero acceleration inputs to the *Ideal Inverse Gimbal Dynamics* in the simulation. Commanded torque is equal to zero).

Torque produced by the motors under constant velocity reference can also be interpreted as the *Trimming Torque*. It is the torque needed to balance the system so that the resultant moment acting on the gimbal is zero and gimbal has zero acceleration. Ideally, *Trimming Torque* is desired to be zero. When it is different from zero, this torque can be treated as the disturbance torque and it is not composed of the friction torque, solely. If gimbal dynamics is only represented with a rotating inertia term, then this torque can be considered as the friction torque (Eqn. 5.1). In Eqn. 5.1, T_f is the total friction torque, T_{motor} is the torque produced by the motor, J is the inertia that represents the *Forward Gimbal Dynamics* and $\ddot{\theta}$ is the angular acceleration of the gimbal platform.

$$\bar{T}_{motor} = \bar{J}\ddot{\theta} + \bar{T}_f \quad (5.1)$$

However, multi-axis gimbal is a chain mechanism. Linkages are connected by joints to build up the mechanism. Thus, there exists disturbance torques resulting from assembling the linkages (see Chapter 2, Eqns 2.27-2.28) and they are dependent on the model parameters (distances and inertia terms). For this reason, overall

disturbance acting on the system calculated by constant velocity experiments cannot be represented by a general friction model.

Since, two-axis gimbal is a coupled system, experiments for azimuth and elevation gimbals are done together. In the first round of experiments, azimuth and elevation gimbals are excited at the same time with the same constant velocities ranging from $1^\circ/s$ to $10.5^\circ/s$. MEMS gyroscope present in the set-up has a measurement noise of zero mean and $0.1^\circ/s$ variance. In order not to end up with a misleading remark, low velocity range is not studied with the set-up (system is not excited under $1^\circ/s$ velocity input). At each velocity, plant outputs $(\theta_m, \dot{\theta}_m, \psi_a, \dot{\psi}_a)$ and average torques (T_{mc}, T_{ac}) applied to the system are recorded. Average torques applied to the system are treated as the overall disturbance torques (T_{dm}, T_{da}) .

It has been observed that:

- Both for azimuth and elevation gimbals, disturbance torque increases as the angular velocity increases.

Disturbance torque-velocity mapping from the experiments are given in Figs. 5.1 and 5.2 for azimuth and elevation gimbals, respectively.

Under positive constant velocity inputs, inner and outer gimbals attain a linear position behaviour ranging from 0° to their FOR limits (20° and 45°).

It has been observed that:

- Both for azimuth and elevation gimbals, disturbance torque increases as the angular position increases under constant velocity.

Disturbance torque-position mapping under $4^\circ/s$ constant velocity input are given for azimuth and elevation gimbals in Figs. 5.3. and 5.4.

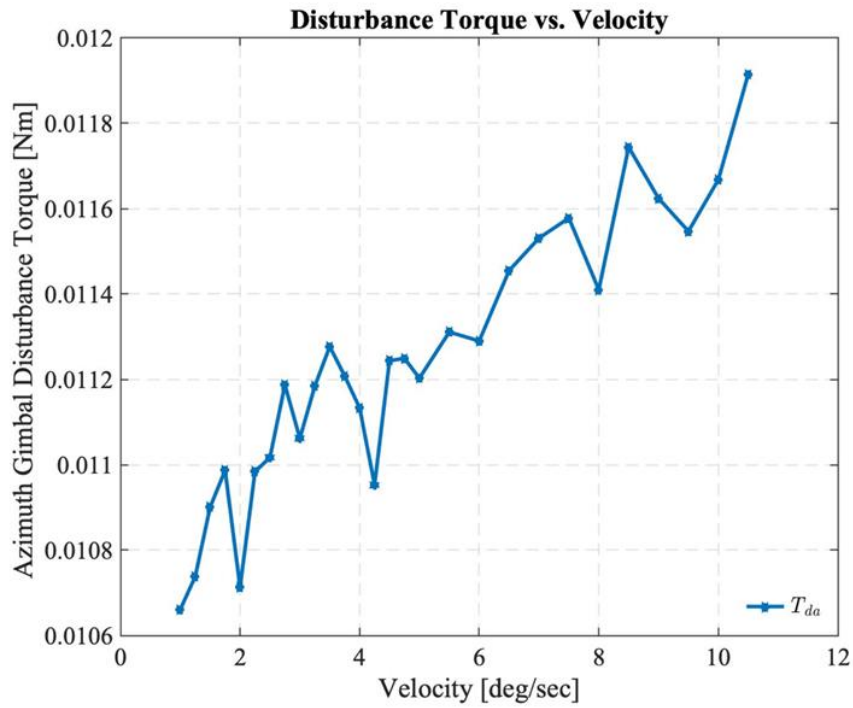


Figure 5.1: The disturbance torque-velocity graph of the azimuth gimbal from the experimental data

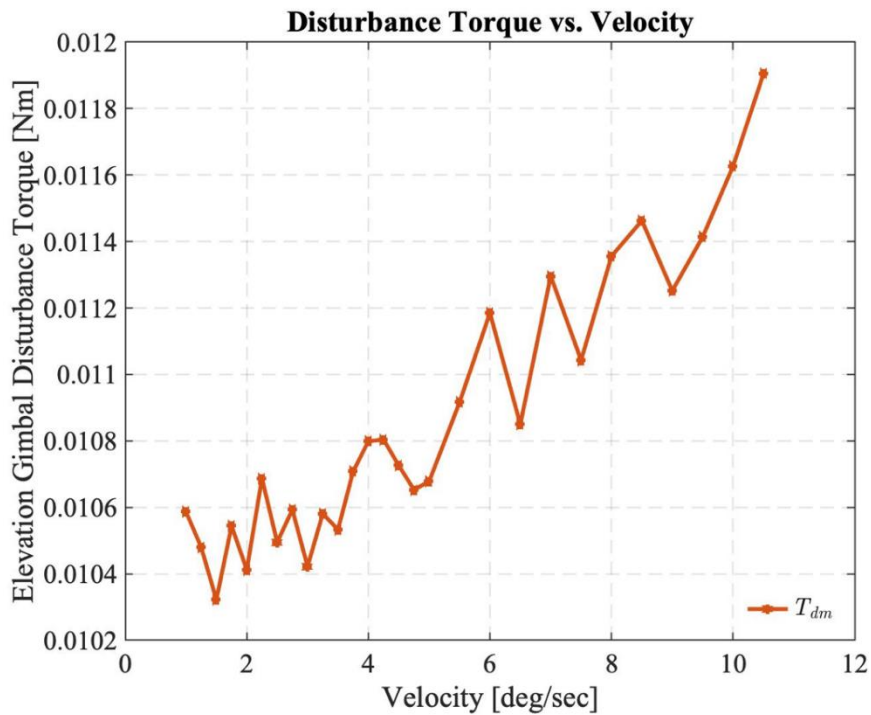


Figure 5.2: The disturbance torque-velocity graph of the elevation gimbal from the experimental data

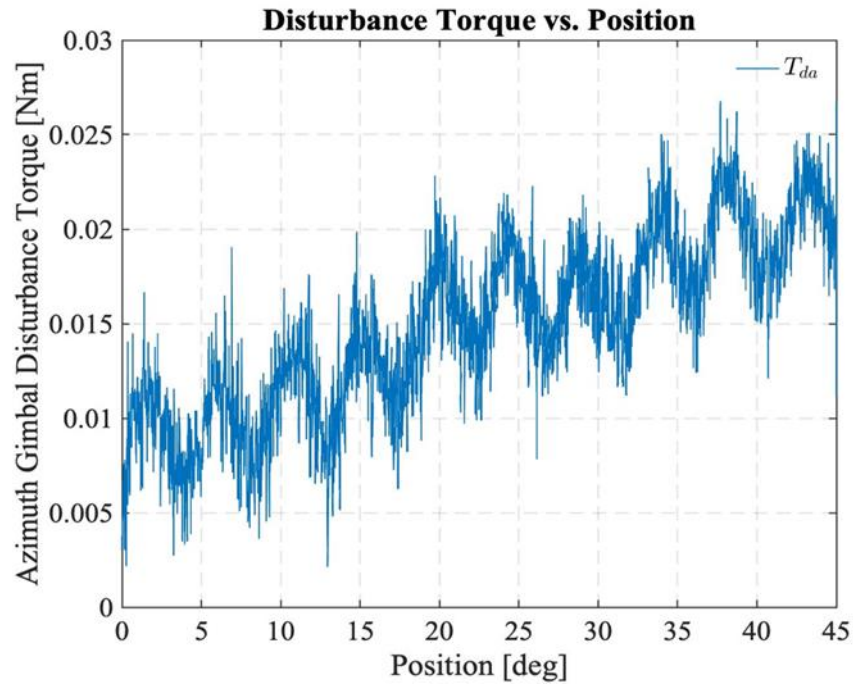


Figure 5.3: The disturbance torque-position graph of the azimuth gimbal from the experimental data

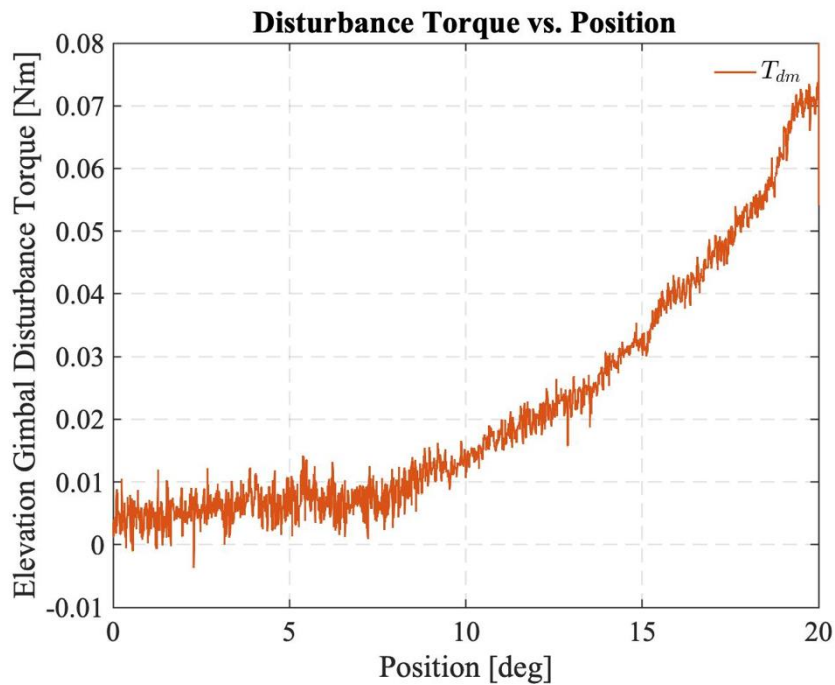


Figure 5.4: The disturbance torque-position graph of the elevation gimbal from the experimental data

Gimbal's pose dependent behaviour of the disturbance torque can also be explained by the following example. Under a pulse input, after gimbal reaches the desired position, the velocity will be zero. By using this information, disturbance torque at different positions of the gimbal can be calculated. This torque can be interpreted as the torque needed to move the system from that particular position under the effects of disturbance torques. In Fig. 5.5, elevation gimbal is moved step by step from 0° to 15° with pulse inputs having 3° magnitude. As the angular position of the elevation gimbal increases from 0° to 15° , mean value of the torque required to hold the gimbal at that particular position with zero velocity also increases. For this experiment, azimuth gimbal is held stationary. Same experiment is also performed with the azimuth gimbal by moving it step by step from 0° to 30° with pulse inputs having 5° magnitude and holding the elevation gimbal stationary. Unfortunately, due to gyro noise, deriving interpretations from the collected data for the azimuth axis was not meaningful.

Two-axis gimbal is a MIMO system, motion of elevation and azimuth axes are dependent on each other. In the second round of experiments, elevation gimbal is excited with $3^\circ/s$ velocity and velocity of azimuth gimbal is changed from $0^\circ/s$ to $8^\circ/s$. The aim of this experiment is to investigate the effect of azimuth gimbal motion on the disturbance torque of the elevation gimbal.

It has been observed that:

- Elevation gimbal's disturbance torque changes behaviour under the azimuth gimbal motion.

Results are shown in Fig. 5.6.

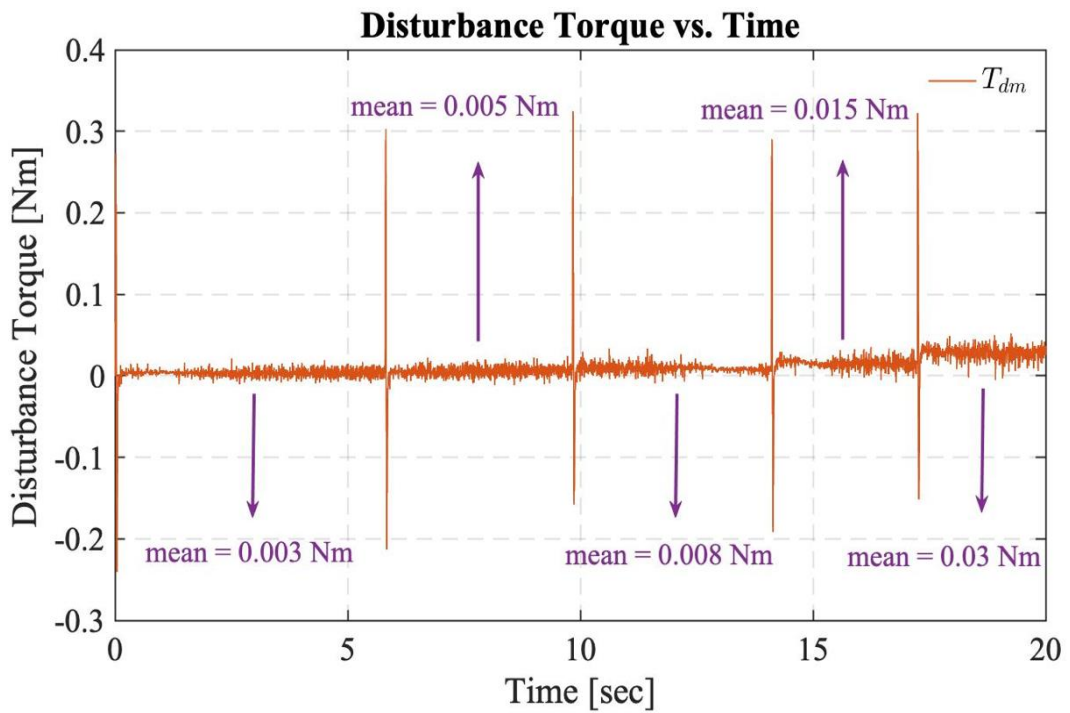
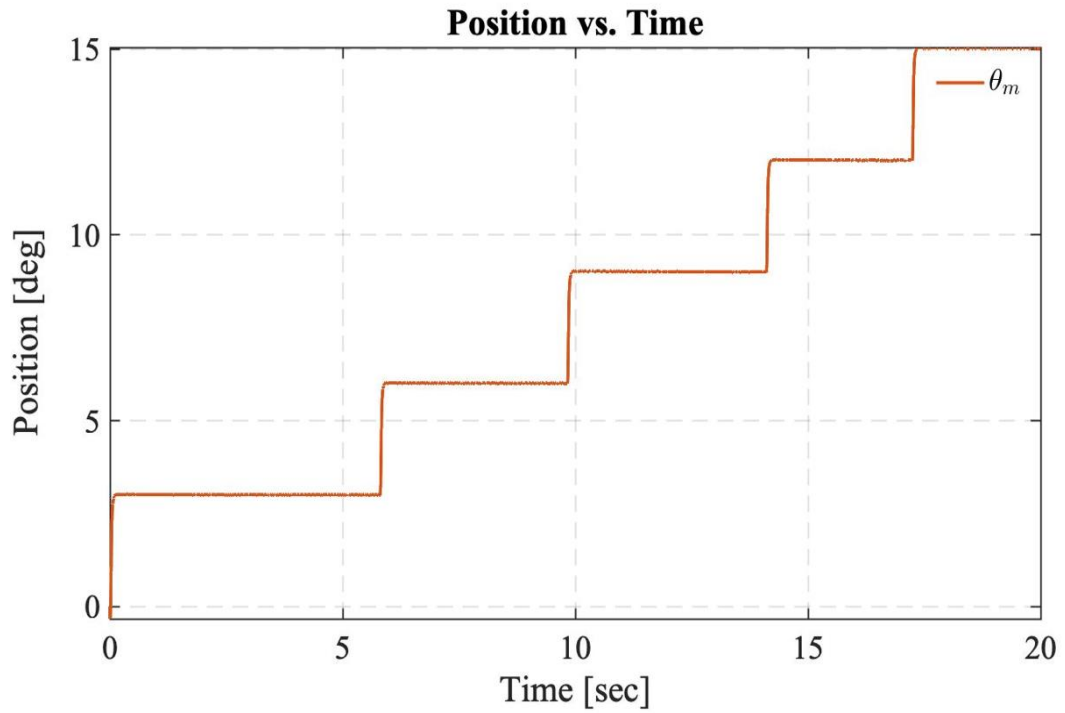


Figure 5.5: The position-time and disturbance torque-time graphs of the elevation gimbal from the experimental data under pulse input

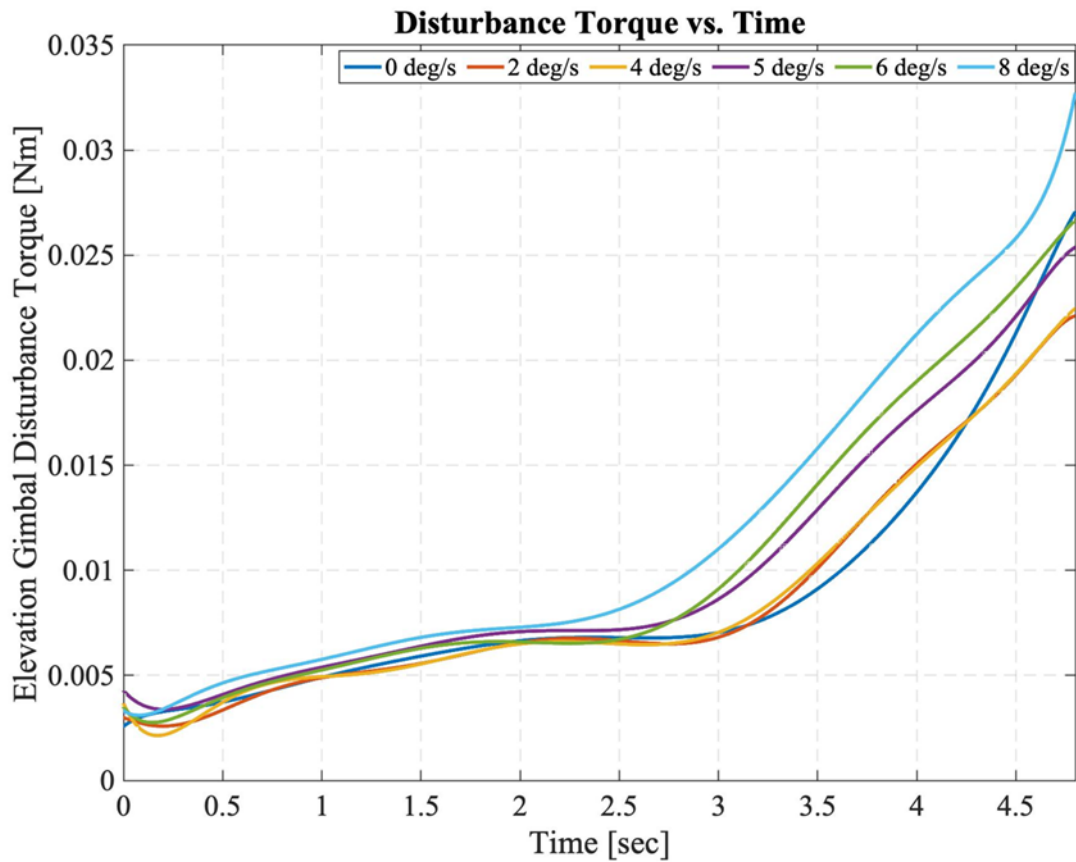


Figure 5.6: The disturbance torque graph of the elevation gimbal for different azimuth gimbal velocities

It is concluded that, disturbance torque present in the system is dependent on states $(\theta_m, \dot{\theta}_m, \psi_a, \dot{\psi}_a)$, (Figs. 5.1, 5.2, 5.3, 5.4, 5.5). There is coupling between azimuth and elevation gimbals, so that the motion of one gimbal affects the other (Fig. 5.6). Since, disturbance torque present in each gimbal is a function of it's own position and velocity and it is somehow related to other gimbal's position and velocity, we can propose, first a simple and a linear function for modeling the disturbance torque in the system as given in Eqn. 5.2 and 5.3. In Fig. 5.4, it has been observed that there exist a nonlinear relationship between disturbance torque and elevation gimbal's position.

$$T_{da} = k1_a \dot{\theta}_m + k2_a \theta_m + k3_a \theta_m^2 + k4_a \dot{\psi}_a + k5_a \psi_a + k6_a \quad (5.2)$$

$$T_{dm} = k1_e \dot{\theta}_m + k2_e \theta_m + k3_e \theta_m^2 + k4_e \dot{\psi}_a + k5_e \psi_a + k6_e \quad (5.3)$$

In order to identify the coefficients, $k1_a, k2_a, k3_a, k4_a, k5_a, k6_a$ and $k1_e, k2_e, k3_e, k4_e, k5_e, k6_e$, several datasets are collected from the experimental setup under different constant velocity inputs. Collected data is used to form an equation of the form, $A\bar{x} = \bar{b}$, which is solved in the least square sense. Corresponding to each dataset, a set of coefficients are identified. Datasets and identified coefficients from each dataset are given in Table 5.1. Symbolic representations of matrix A and vectors \bar{x} and \bar{b} are given in Eqns. 5.4, 5.5 and 5.6.

The parameters $k1_a, k2_a, k3_a, k4_a, k5_a$ and $k1_e, k2_e, k3_e, k4_e, k5_e$ are associated with the state dependent friction torques, cogging torques of wires and cooling pipes. Similarly, the parameters $k6_a$ and $k6_e$ are associated with the state independent bias terms, disturbances related to mechanism and linkages (i.e., off-diagonal inertia terms and CoG, rotation axis offsets).

$$\hat{A} = \begin{bmatrix} \dot{\theta}_m & \theta_m & \theta_m^2 & \dot{\psi}_a & \psi_a & 1 & 0 & 0 & 0 & 0 & 0 & 0 \\ 0 & 0 & 0 & 0 & 0 & 0 & \dot{\theta}_m & \theta_m & \theta_m^2 & \dot{\psi}_a & \psi_a & 1 \end{bmatrix} \quad (5.4)$$

$$\bar{x} = [k1_a \quad k2_a \quad k3_a \quad k4_a \quad k5_a \quad k6_a \quad k1_e \quad k2_e \quad k3_e \quad k4_e \quad k5_e \quad k6_e]^T \quad (5.5)$$

$$\bar{b} = \begin{bmatrix} T_{da} \\ T_{dm} \end{bmatrix} \quad (5.6)$$

Table 5.1: Details regarding DataSets (constant velocity data with simple disturbance function)

		DataSet 1	DataSet 2	DataSet 3	DataSet 4	DataSet 5
Azimuth gimbal input (deg/s)		3	2	5	1	7
Elevation gimbal input (deg/s)		2	4	3	1	7
\bar{x}	$k1_a$	0.0013	0.0011	0.0013	0.0011	2.77×10^{-4}
	$k2_a$	-0.0312	-0.0266	-0.0123	-0.013	-0.0014
	$k3_a$	-2.5×10^{-5}	4.35×10^{-5}	-2.8×10^{-6}	5.07×10^{-7}	2.39×10^{-5}
	$k4_a$	3.54×10^{-4}	-5.38×10^{-4}	-6.49×10^{-4}	-0.0013	-4.38×10^{-6}
	$k5_a$	0.017	-0.0395	0.0073	0.008	0.0012
	$k6_a$	-0.0025	-0.0071	0.0045	-0.0023	0.0051
	$k1_e$	-0.0025	-0.0014	-0.0027	-0.003	-0.0023
	$k2_e$	0.0071	0.0073	0.0087	0.0176	-0.0145
	$k3_e$	1.95×10^{-4}	1.97×10^{-4}	1.96×10^{-4}	1.78×10^{-4}	1.59×10^{-4}
	$k4_e$	0.002	0.0026	0.0021	9.48×10^{-4}	0.0021
	$k5_e$	-0.0043	-0.0125	-0.0056	-0.0108	0.0122
	$k6_e$	0.0059	0.0029	0.0051	0.0194	-0.0013

It was expected (if the system were linear) to find similar coefficients from each dataset and form a single function that represents the disturbance torque for the whole operational range. However, each coefficient set is very different from each other. Fig. 5.7 shows the estimated disturbance torque calculated with the coefficients given in Table 5.1 and the real disturbance torque obtained from the experiment plotted together for the DataSet 1.

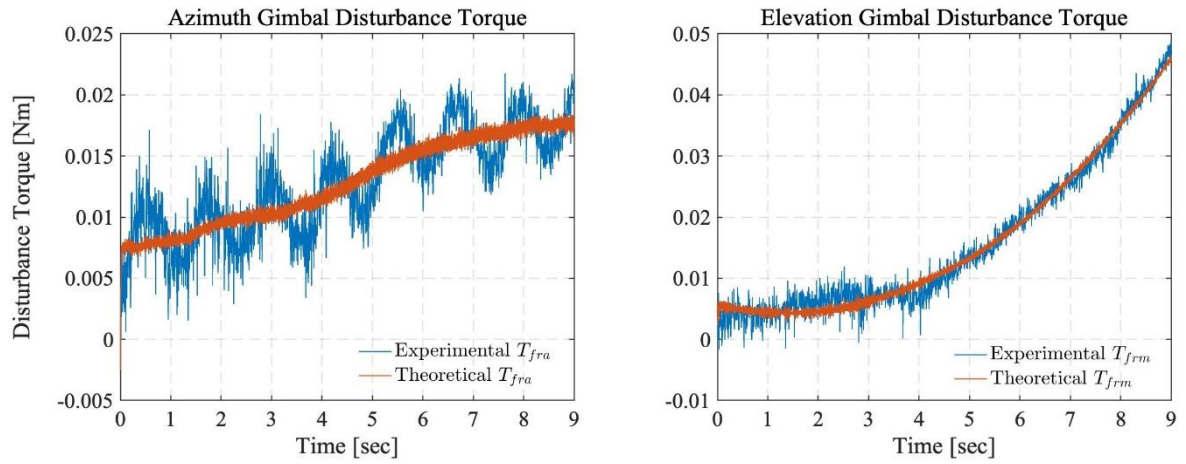


Figure 5.7: The estimated disturbance torque-real disturbance torque graph for DataSet 1 plotted both for azimuth and elevation gimbals with the coefficient set of DataSet 1

Next, estimated disturbance torque for DataSet 5 is calculated with the coefficients found from the DataSet1 in Fig. 5.8. As it is observed in Fig.5.8, coefficients found from DataSet 1 do not fit for the disturbance function of DataSet 5. Similar computational studies are performed for other pairings and the same conclusion is reached in each case. For example, Fig. 5.9 shows the estimated disturbance torque calculated with the coefficients found from the DataSet1 for the disturbance torque present in DataSet 4. Even though coefficients from DataSet1 better represents the disturbance function of DataSet 4 than the disturbance function of DataSet5, there is still considerable difference between estimated and real torques. In Figs. 5.7-5.9, theoretical disturbance torque is the disturbance torque calculated with the coefficients given in Table 5.1 and with the Eqns. 5.2 and 5.3.

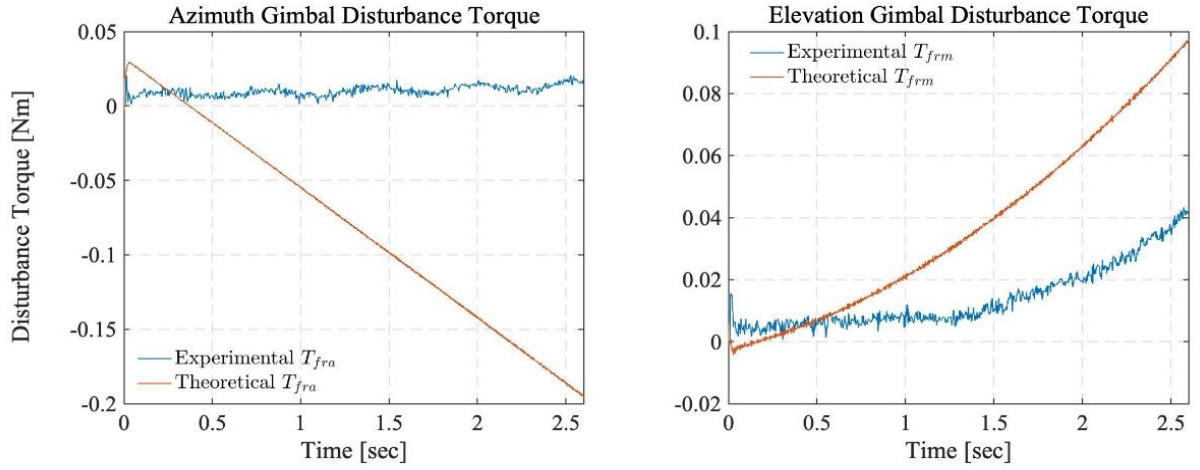


Figure 5.8: The estimated disturbance torque-real disturbance torque graph for DataSet 5 plotted both for azimuth and elevation gimbals with the coefficient set of DataSet 1

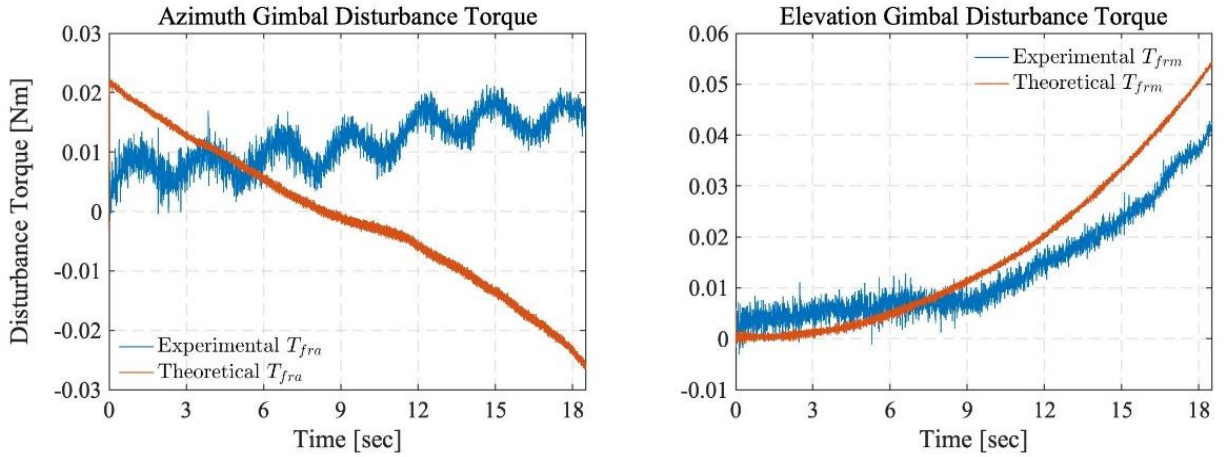


Figure 5.9: The estimated disturbance torque-real disturbance torque graph for DataSet 4 plotted both for azimuth and elevation gimbals with the coefficient set of DataSet 1

These observations lead us to the conclusion that there exists a state dependent, highly nonlinear, time-varying and complex disturbance torque present in the experimental set-up. This disturbance torque also changes its behaviour with respect to different inputs for azimuth and elevation gimbals. So, it is very difficult for us to fit a general disturbance model that represents the behavior in the FOR range of the

setup. Instead, we offer a *nonlinear regressor*, “*a multi-layer perceptron*”, to represent the disturbance torque in the system and perform torque compensation when PID controller is not sufficient enough to overcome disturbances.

5.2 Approach 2: Disturbance Torque Estimation by Using Ideal Inverse Dynamics-Real Plant-Ideal Inverse Dynamics

Different from Approach 1, based on our detailed mathematical model, disturbance torque can be estimated by using the triplet, “*Ideal Inverse Dynamics-Real Plant-Ideal Inverse Dynamics*”. It is assumed that the differential torque between the first and second *Ideal Inverse Dynamics* is the disturbance torque.

In this section, disturbance torque present at the experimental setup is determined by using *Ideal Inverse Dynamics-Real Plant-Ideal Inverse Dynamics*, in this order. Successive use of this sequence in xPC Target, enables us to observe the complex disturbance function under a desired input in the experimental setup. In order to find the disturbance torque for a varying velocity reference (i.e., sinusoidal input), an open loop block diagram given in Fig. 5.10 can be used while working with xPC Target.

Eqns. 3.1-3.7, provided in Chapter 3, Section 3.1 are also valid for Fig. 5.10. Similar to Section 3.1, in order to derive the acceleration input, \ddot{r} , that is used as an input for the second *Ideal Inverse Gimbal Dynamics* in the block diagram of the real system, a backwards derivative operation at every 10 data point is performed for the gyro data. The output of the second *Inverse Gimbal Dynamics* block, is the corresponding torque (\bar{u}'_d) produced from the output of the *Real Plant* (Eqn. 5.7). $\bar{\Delta u}$ is the disturbance torque (differential torque) in the system (Eqn. 5.8). *Motor Dynamics* block is explained in detail in Chapter 3, Section 3.1.

$$\bar{\mathbf{u}}'_d = [T_{ma} \quad T_{mm}]^T \quad (5.7)$$

$$\bar{\Delta \mathbf{u}} = \bar{\mathbf{u}}'_d - \bar{\mathbf{u}}_d = [\Delta T_a \quad \Delta T_m]^T = [T_{da} \quad T_{dm}]^T \quad (5.8)$$

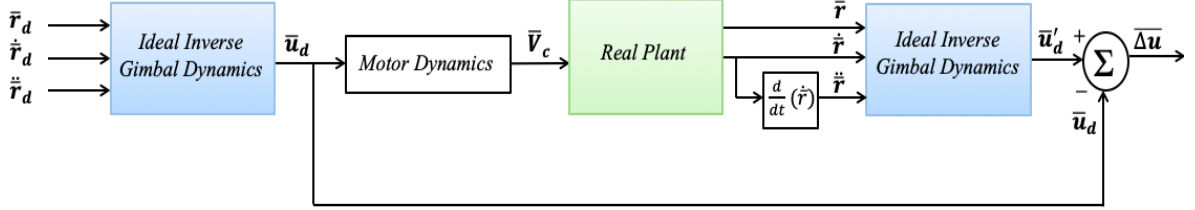


Figure 5.10: Open loop block diagram used in xPC Target for calculating T_{da} and T_{dm}

In Fig. 5.11, $10^\circ @ 2 \text{ Hz}$ position input is commanded for the azimuth gimbal and $7^\circ @ 2 \text{ Hz}$ position input is commanded for the elevation gimbal. In Fig. 5.12, $3^\circ @ 5 \text{ Hz}$ position input is commanded both for the azimuth gimbal and the elevation gimbals. In Fig. 5.13, $5^\circ @ 4 \text{ Hz}$ position input is commanded both for the azimuth gimbal and the elevation gimbals. T_{ac} , T_{ma} and T_{da} are plotted for the azimuth gimbal in Figs. 5.11-5.13 for the corresponding inputs.

In order to perform a nonlinear interpolation that represents the disturbance torques given in Figs. 5.11-5.13, studies carried out similar to what is done in Section 5.1. This time, disturbance torques are assumed to have a more complex and highly nonlinear form as given in Eqns. 5.9 and 5.10.

$$T_{da} = k1_a \dot{\theta}_m + k2_a \theta_m^2 + k3_a \dot{\psi}_a + k4_a \psi_a^4 - k5_a (\psi_a^5 \theta_m^3) + k6_a \quad (5.9)$$

$$T_{dm} = k1_e \dot{\theta}_m + k2_e \theta_m^3 + k3_e \dot{\psi}_a + k4_e \psi_a^2 - k5_e (\psi_a \theta_m^3) + k6_e \quad (5.10)$$

Representation of the matrix \hat{A} for the complex functions of disturbance torques is given in Eqn. 5.11.

$$\hat{A} = \begin{bmatrix} \dot{\theta}_m & \theta_m^2 & \dot{\psi}_a & \psi_a^4 & \psi_a^5 \theta_m^3 & 1 & 0 & 0 & 0 & 0 & 0 & 0 \\ 0 & 0 & 0 & 0 & 0 & 0 & \dot{\theta}_m & \theta_m^3 & \dot{\psi}_a & \psi_a^2 & \psi_a \theta_m^3 & 1 \end{bmatrix} \quad (5.11)$$

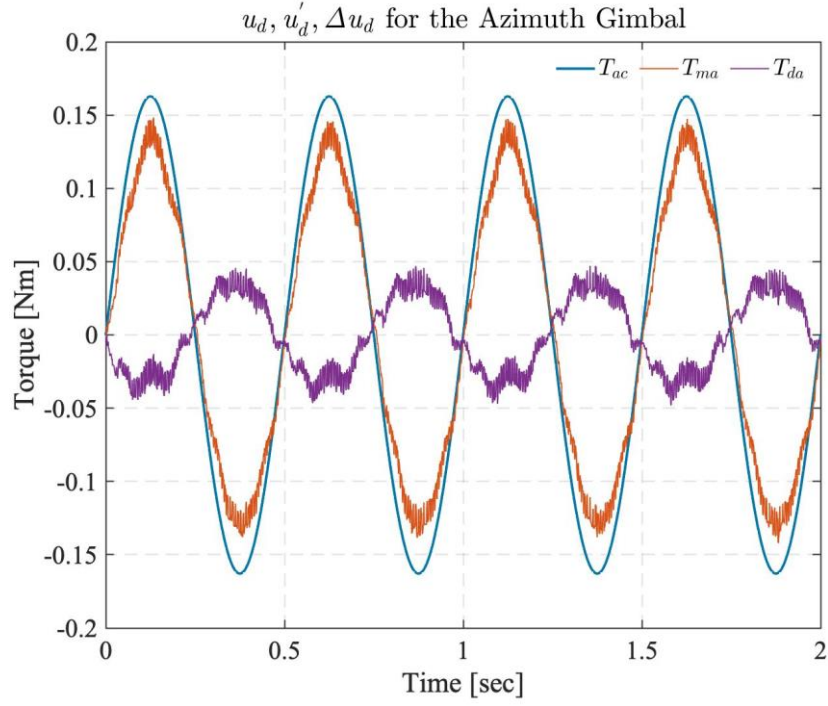


Figure 5.11: T_{ac} , T_{ma} and T_{da} plotted for the $10^\circ @ 2 \text{ Hz}$ commanded position input of the azimuth gimbal

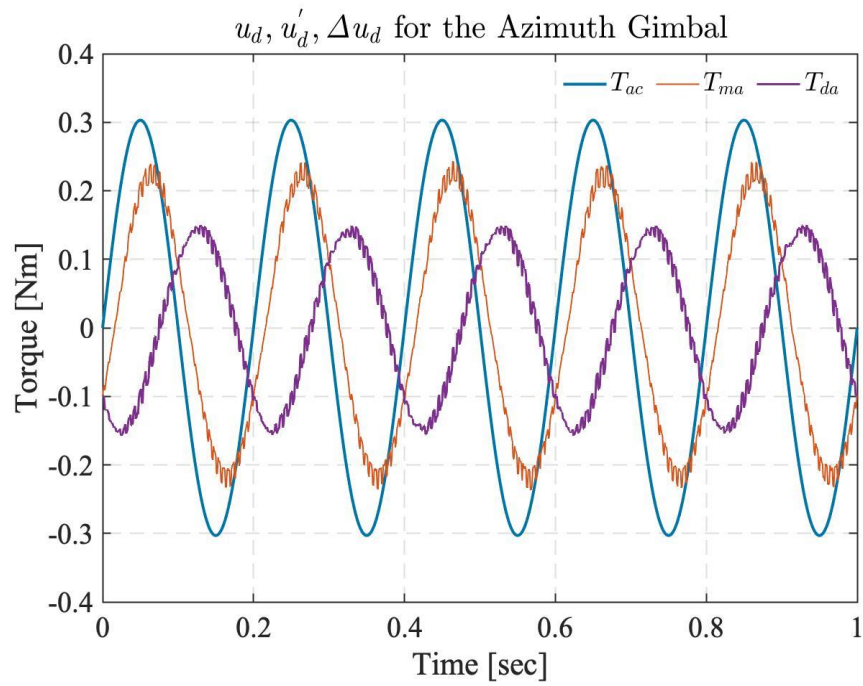


Figure 5.12: T_{ac} , T_{ma} and T_{da} plotted for the $3^\circ @ 5 \text{ Hz}$ commanded position input of the azimuth gimbal

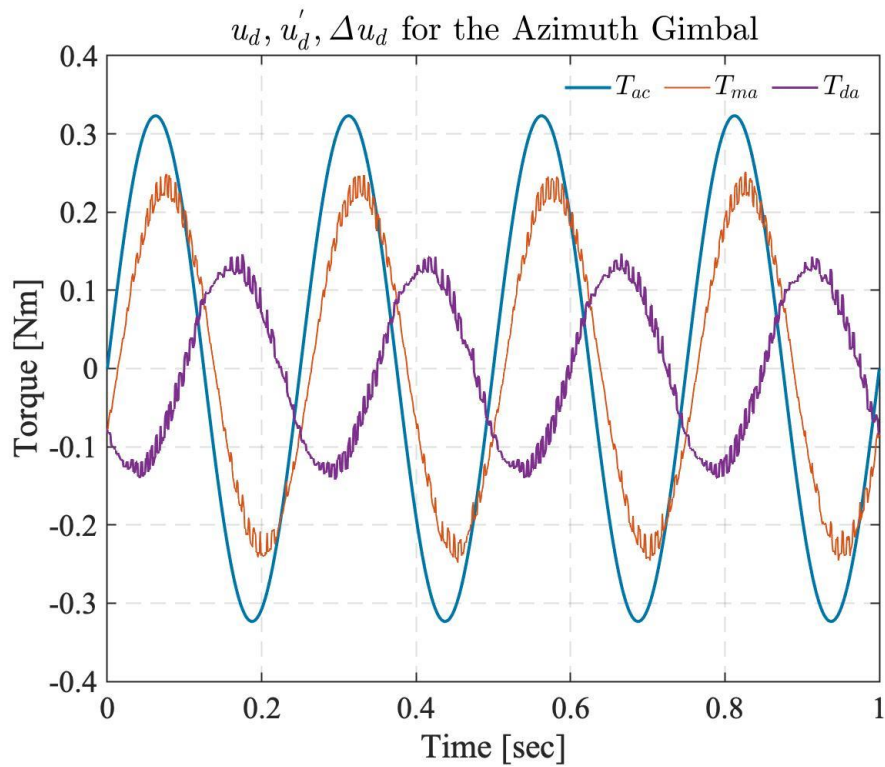


Figure 5.13: T_{ac} , T_{ma} and T_{da} plotted for the $5^\circ @ 4 \text{ Hz}$ commanded position input of the azimuth gimbal

Reference inputs for three different datasets and identified disturbance coefficients from these datasets by using matrices given in Eqns. 5.5, 5.6 and 5.11 are listed in Table 5.2. Each coefficient set works well for the dataset that is calculated from; but fails to represent the system when it is applied to the other dataset *even for the more complex functions of disturbance torques*. Fig. 5.14 shows the estimated disturbance torque calculated with the coefficients found from the DataSet 6 for the disturbance torque present in DataSet 6. Fig. 5.15 shows the estimated disturbance torque calculated with the coefficients found from DataSet 6 for the disturbance torque present in DataSet 7. All the information obtained in Chapter 5, lead us to develop a neural network based disturbance torque compensator for the two-axis gimbal system.

Table 5.2: Details regarding DataSets (sinusoidal data with complex disturbance function)

		DataSet 6	DataSet 7	DataSet 8
Azimuth gimbal input		$5^\circ @ 4 \text{ Hz sine}$	$3^\circ @ 5 \text{ Hz sine}$	$10^\circ @ 2 \text{ Hz sine}$
Elevation gimbal input		$5^\circ @ 4 \text{ Hz sine}$	$3^\circ @ 5 \text{ Hz sine}$	$7^\circ @ 2 \text{ Hz sine}$
\bar{x}	$k1_a$	9.06×10^{-5}	-0.0033	-0.0064
	$k2_a$	0.0038	0.0088	-0.0014
	$k3_a$	9.94×10^{-4}	0.0044	0.0035
	$k4_a$	-2.09×10^{-6}	-7.35×10^{-6}	3.37×10^{-7}
	$k5_a$	-3.2×10^{-11}	1.65×10^{-9}	2.43×10^{-11}
	$k6_a$	0.0721	0.1546	0.0104
	$k1_e$	0.0014	0.0011	4.15×10^{-4}
	$k2_e$	0.0019	0.0019	-1.49×10^{-4}
	$k3_e$	-6.62×10^{-4}	-1.01×10^{-4}	-2.26×10^{-4}
	$k4_e$	-7.09×10^{-4}	-0.0013	-2.52×10^{-4}
	$k5_e$	1.62×10^{-4}	1.74×10^{-4}	-2.63×10^{-6}
	$k6_e$	0.1304	0.1928	0.0234

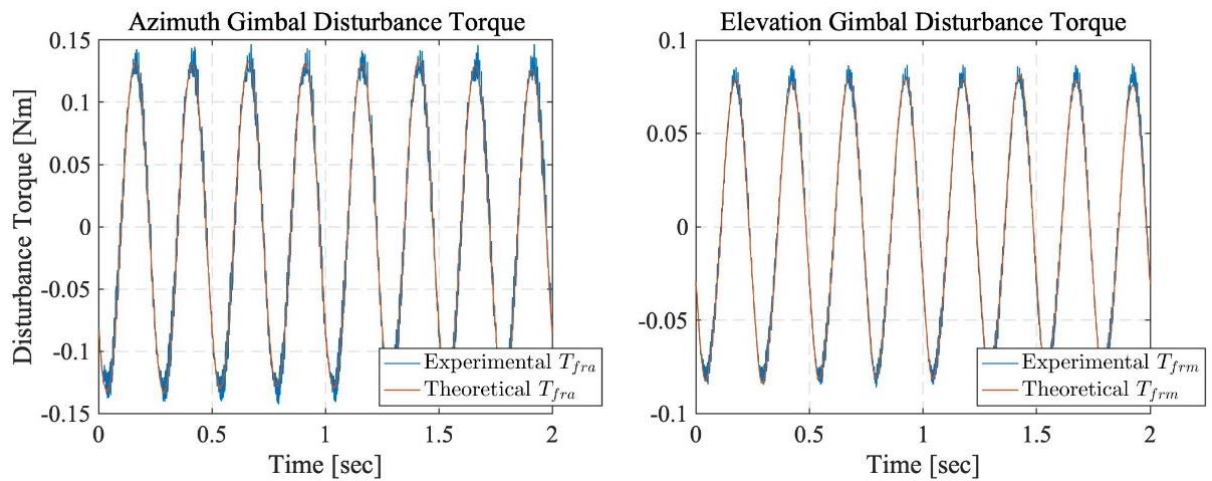


Figure 5.14: The estimated disturbance torque-real disturbance torque graph for DataSet 6, plotted both for azimuth and elevation gimbals with the coefficient set of DataSet 6

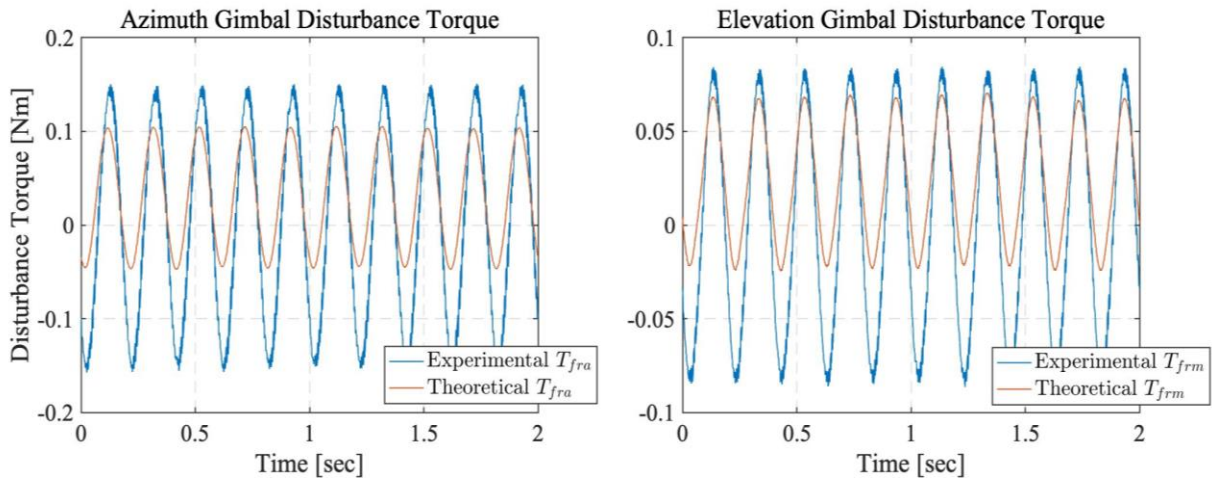


Figure 5.15: The estimated disturbance torque-real disturbance torque graph for DataSet 7, plotted both for azimuth and elevation gimbals with the coefficient set of DataSet 6

Summary of Chapter 5:

Disturbance torque calculated either by constant velocity experiments or *Ideal Inverse Dynamics–Real Plant– Ideal Inverse Dynamics* sequence, is the result of friction and model uncertainties (Chapter 2, Eqns. 2.27-2.28). Therefore, total disturbance torque acting on the system, cannot be represented using a friction model that is dependent only on gimbal's velocity. Such friction models do not represent the cross-coupling nature of the disturbance torque and cannot capture the disturbances caused by the rotation axis, CoG offsets and off-diagonal inertia parameters (i.e., viscous, LuGre, Leuven friction models). In this study, a MLP structure is suggested for disturbance torque estimation and it is explained in detail in Chapter 6. *Ideal Inverse Dynamics–Real Plant– Ideal Inverse Dynamics* sequence will be used for collecting the training data of MLP from the experimental set-up.

Chapter 6

MLP-Assisted Control Structure

In this chapter, neural network based control structures are developed for a two-axis gimbal system. Neural networks are employed to approximate the complex nature of the disturbance torque present in the experimental set-up (Chapter 5) and support the pre-existing cascaded PID control structure. There are three different methods to implement the neuro-control structures. The performance of the proposed algorithm (Method 2) is first verified by simulation studies. Experiments of the system with the NN-based controller, cascaded PID controller and ADRC with linear ESO, [35] are carried out in Simulink®. Then, the proposed controller is tested in the real set-up shown in Chapter 3 by using Simulink Real-Time®. Associated block diagrams and plots will be given in the following pages.

6.1 Method 1: NN Based Control Structure with Inverse Gimbal Dynamics (NNX)

Figures 6.1, 6.2 and 6.3 describe the training data collection and controller structure implementation of the first neural network structure, NNX. It is trained by using “Ideal Inverse Gimbal Dynamics and Disturbed Inverse Gimbal Dynamics”, (Fig.6.1).

Disturbed Inverse and *Forward Gimbal Dynamics* implies that there is friction torque present in the revolute joint between the outer ring and the base platform (T_{fra}) and in the revolute joint between the inner and outer rings of the 2-DoF gimbal assembly (T_{frm}). For the *Disturbed Inverse Gimbal Dynamics* model, friction torques T_{fra}, T_{frm} are introduced as the viscous friction torques (Eqns. 6.1, 6.2) with coefficients b_a, b_e (taken as 0.08 Nm.sec).

$$T_{fra} = b_a \dot{\psi}_a \quad (6.1)$$

$$T_{frm} = b_e \dot{\theta}_m \quad (6.2)$$

When desired acceleration ($\ddot{\bar{r}}_d$), velocity ($\dot{\bar{r}}_d$) and position (\bar{r}_d) are feed into *Ideal Inverse Gimbal Dynamics*, required torque (\bar{u}_d) needed to perform this motion will be produced for an ideal system. When these inputs are feed into *Disturbed Inverse Gimbal Dynamics*, same inputs will produce the torque needed to overcome this friction and perform the required motion. The differential torque between them, ($\overline{\Delta u}$), can be interpreted as the overall disturbance torque acting on the system. The training data set of NNX is $\{(\bar{r}_d, \dot{\bar{r}}_d, \ddot{\bar{r}}_d), \overline{\Delta u}, t \in [0, t_f]\}$, (Fig. 6.2). Explicit form of vectors in Figs. 6.1, 6.2 and 6.3 are given in Chapters 3, 5, Eqns. 3.1-3.7, 5.7, 5.8.

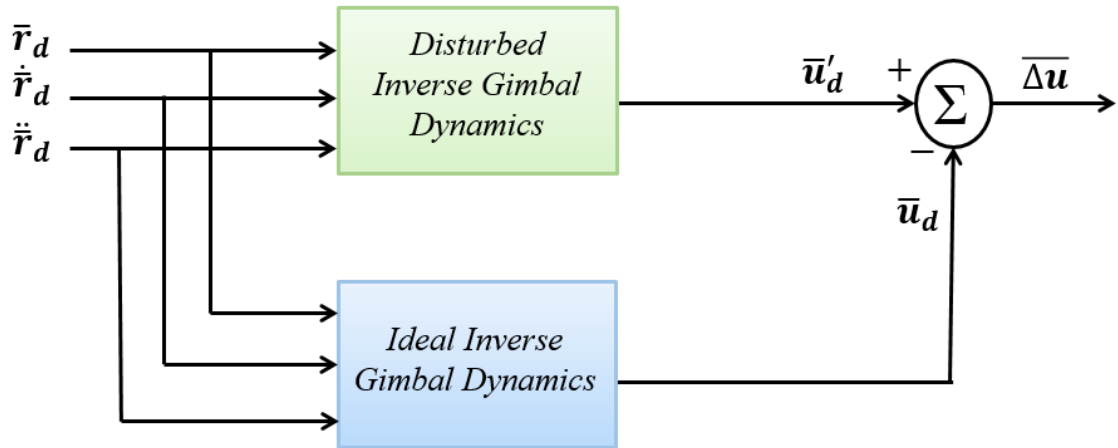


Figure 6.1: Training method for NNX (Neural Network X)

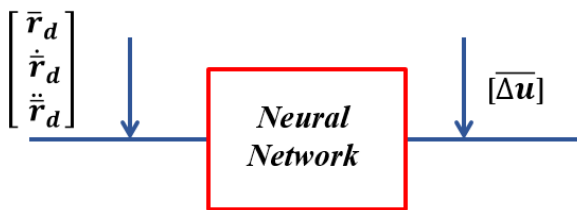


Figure 6.2: Input-output relationship of NNX

The difference between \bar{u}_d and \bar{u}'_d results in *Delta Torque* ($\overline{\Delta u}$), enables the real plant (*Disturbed Forward Gimbal Dynamics*) to perform the desired motion in an open loop structure when it is added to \bar{u}_d (Fig. 6.3). The switch mechanism at the output of the neural network enables to show the open loop structure also in Fig. 6.3.

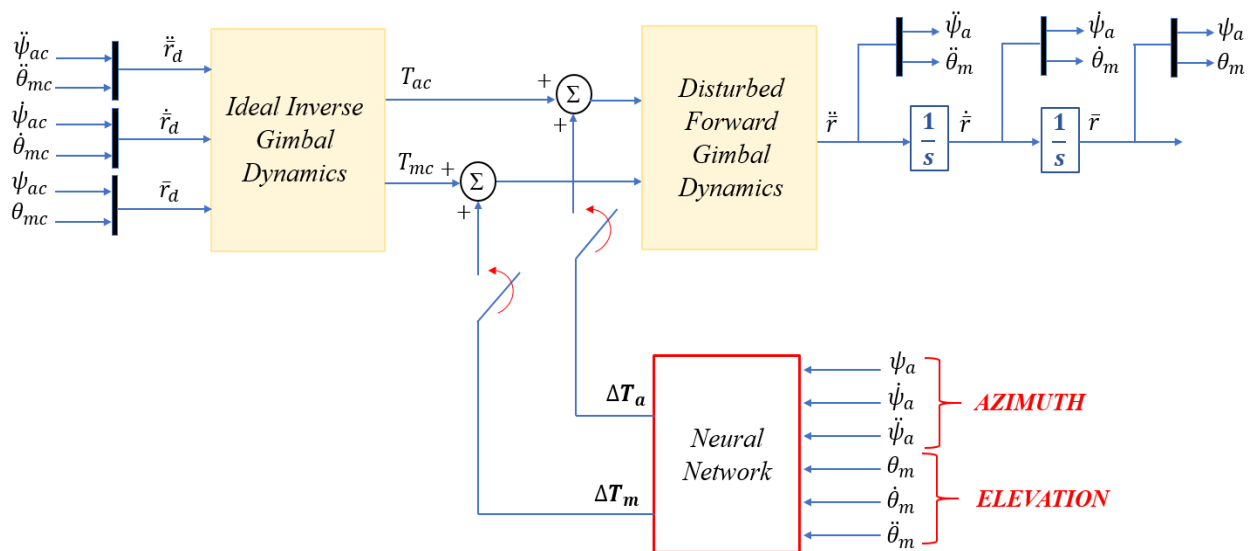


Figure 6.3: Block diagram implementation of NNX in open loop structure

In the following example, NNX structure is trained with the desired position input given in Fig. 6.4 for azimuth and elevation gimbals. We created an amplitude and frequency varying sinusoidal wave as the reference position input that travels from 5° to 25° with an increasing frequency of 0.5 to 4 Hz for the azimuth axis and another amplitude and frequency varying sinusoidal that travels from 2° to 18° with an increasing frequency of 0.5 to 4 Hz for the elevation axis.

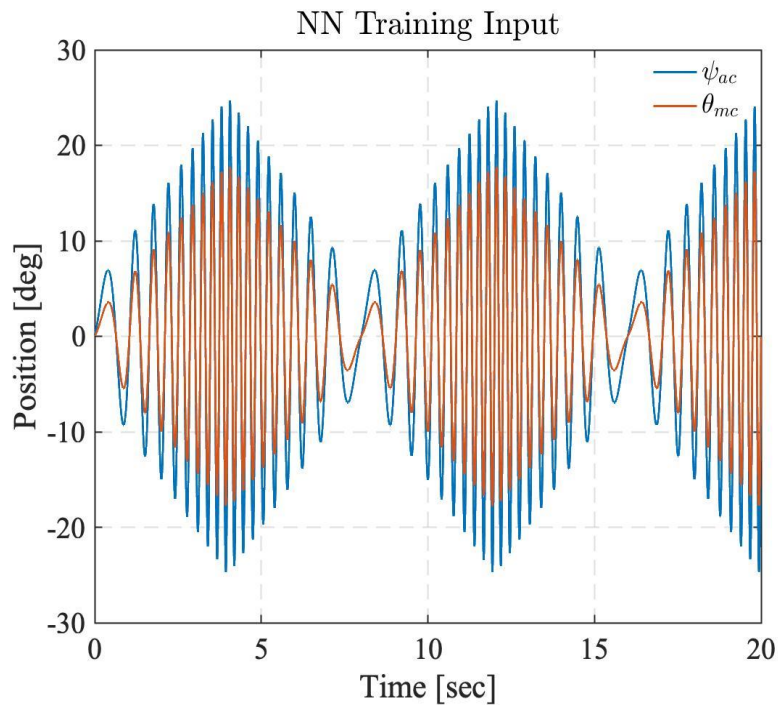


Figure 6.4: NNX training input for azimuth and elevation axes

Fig. 6.5 shows the response of the azimuth axis for an input of sinusoidal wave with 25° amplitude and 1Hz frequency and the response of the elevation axis for an input of 15° amplitude and 1Hz frequency. Gimbals are working simultaneously. Green line shows the output of open loop gimbal, red line is the reference signal and blue line is the response when NNX is present.

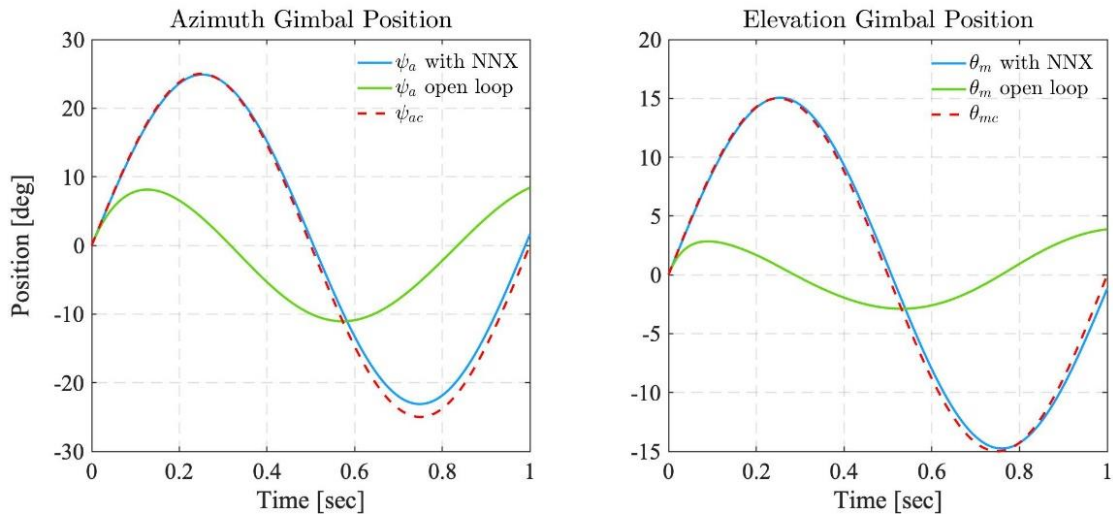


Figure 6.5: Azimuth and elevation gimbal position with NNX structure

Details about the NNX:

The feedforward neural network that is designed for this simulation has 2 hidden layers, each composed of 20 neurons. Layer outputs are calculated by the transfer function *poslin*. Training data has 20001 pairs. Input vector has a dimension of 6 x 20001. It is shuffled before being provided to the network for training. First three rows are the azimuth gimbal’s position, velocity and acceleration; last three rows are the elevation gimbal’s position, velocity and acceleration. Training data output has a dimension of 2 x 20001, first row corresponds to delta torque required for the azimuth axis and second row corresponds to delta torque required for the elevation axis. The training method is chosen as *Levenberg-Marquardt* backpropagation.

6.2 Method 2: NN Based Control Structure with Inverse and Forward Gimbal Dynamics (Torque Compensation)

This section is about disturbance torque compensation by using “*Ideal Inverse Dynamics-Disturbed Forward Dynamics-Ideal Inverse Dynamics*” sequence which is implemented in MATLAB®. *Real Plant* is replaced by *Disturbed Forward Gimbal Dynamics* in simulations. *Disturbed Forward Dynamics* refers to the simulated version of the *Real Plant* with the parameters given in Chapter 3. Disturbance torque functions for azimuth and elevation axes used in simulations have a complex and highly nonlinear form given in Eqns. 6.3 and 6.4 (Chapter 5, Section 5.2). The inputs in Eqns. 6.3 and 6.4 are in radians, so the coefficients are slightly modified and chosen larger with respect to coefficients given in Table 5.2.

$$T_{da} = -0.08\dot{\theta}_m - 0.1\theta_m^2 - 0.2\dot{\psi}_a - 0.1\psi_a^4 - (\psi_a^5\theta_m^3) \quad (6.3)$$

$$T_{dm} = -0.08\dot{\theta}_m - 0.08\theta_m^3 - 0.02\dot{\psi}_a - 0.02\psi_a^2 - (\psi_a\theta_m^3) \quad (6.4)$$

NN training is performed with the block diagram given in Fig. 6.6. Inputs and outputs of the block diagram in Fig. 6.6 are given in open form in Chapter 3, Eqns. 3.1-3.7 and in Chapter 5, Eqns. 5.7-5.8. Input for the *Disturbed Forward Dynamics* is the torque, \bar{T}_c . In simulations, *Motor Dynamics* block is composed of *Torque to Voltage (T2V)* and *Voltage to Torque (V2T)* conversions. By that way, the dynamics that motor brings in real-time experiments is also covered in simulations. Block diagram of the *Motor Dynamics* used in Simulink® is given in Fig. 6.7.

When desired acceleration (\ddot{r}_d), velocity (\dot{r}_d) and position (\bar{r}_d) are feed into *Ideal Inverse Gimbal Dynamics*, required torque (\bar{u}_d) needed to perform this motion will be produced for an ideal system. When \bar{u}_d is feed into *Disturbed Forward Gimbal*

Dynamics or Real Plant, resultant motion will be equal (r, \dot{r}, \ddot{r}) which is different than $(\bar{r}_d, \dot{\bar{r}}_d, \ddot{\bar{r}}_d)$ due to disturbance torque present in the system. \bar{u}'_d is the torque value corresponding to motion of the *Real Plant* or the representative plant of the real system in the simulations (r, \dot{r}, \ddot{r}) . It is obtained by sending the output of *Disturbed Forward Gimbal Dynamics (Real Plant)* to *Ideal Inverse Gimbal Dynamics*. The training data set of the neural network is $\{(\bar{r}_d, \dot{\bar{r}}_d, \ddot{\bar{r}}_d), \bar{\Delta u}, t \in [0, t_f]\}$. Output of the NN is the disturbance torque $(\bar{\Delta u})$. The input-output relationship of the NN is plotted in Fig. 6.8. The proposed design procedure of the NN-based control strategy is presented in the block diagram in Fig. 6.9 for the simulations. Note that, acceleration (\ddot{r}) is the output of the *Disturbed Forward Dynamics* block.

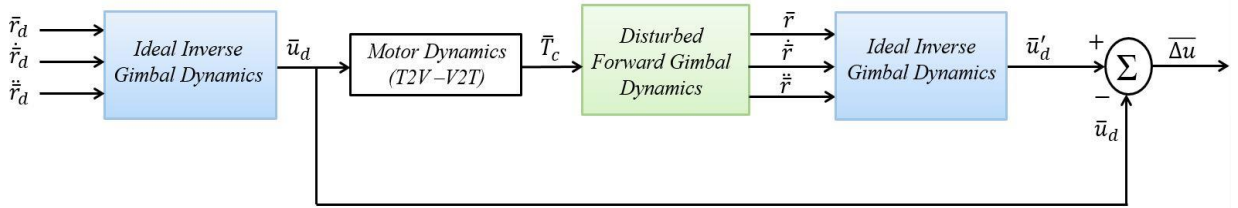


Figure 6.6: Training structure used in Simulink® for Method 2

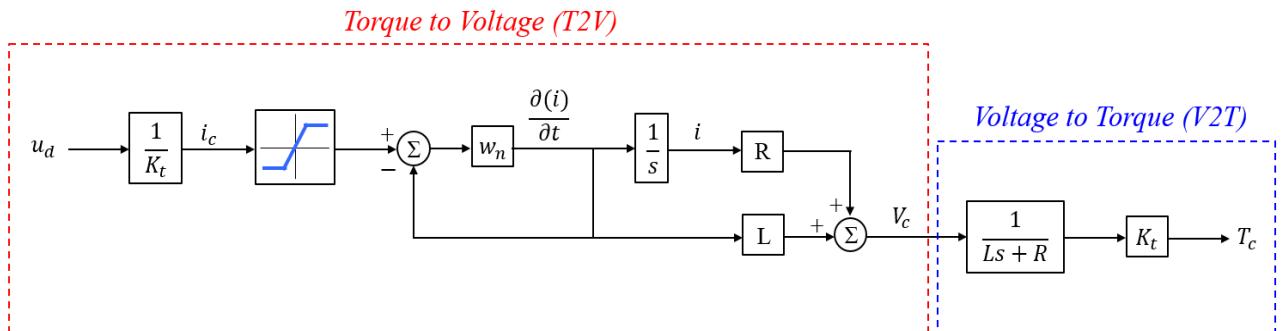


Figure 6.7: Motor Dynamics block in Simulink® (T2V and V2T conversions)

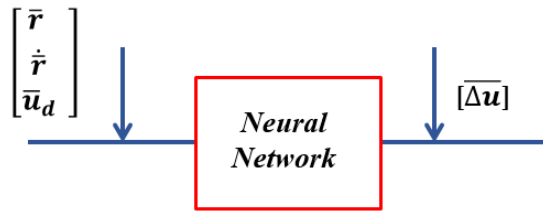


Figure 6.8: Input-output relationship of the NN

The difference between \bar{u}'_d and \bar{u}_d results in *Delta Torque* ($\overline{\Delta u}$), enables the real plant to reach the reference position in a closed loop structure when it is added to \bar{u}_d (Fig. 6.9). It works as a disturbance torque compensator that compensates the loss in the plant. It also works as a feedforward torque estimator; because torque output of PID controller (*Ideal Inverse Gimbal Dynamics*) enters the NN. It enhances the response of the system when the PID controller is not sufficient enough to perform the desired motion (improves target tracking performance).

Other alternatives for Fig. 6.9:

- Note that, position, velocity and acceleration inputs of the first *Inverse Gimbal Dynamics* block is provided from the references. Another alternative can be to provide velocity and acceleration from the plant outputs.
- Instead of \bar{u}_d , \bar{r}_d can be used in the training and input set of the NN.

Both of these strategies are implemented in Simulink® and similar results are obtained with the block diagram given in Fig. 6.9.

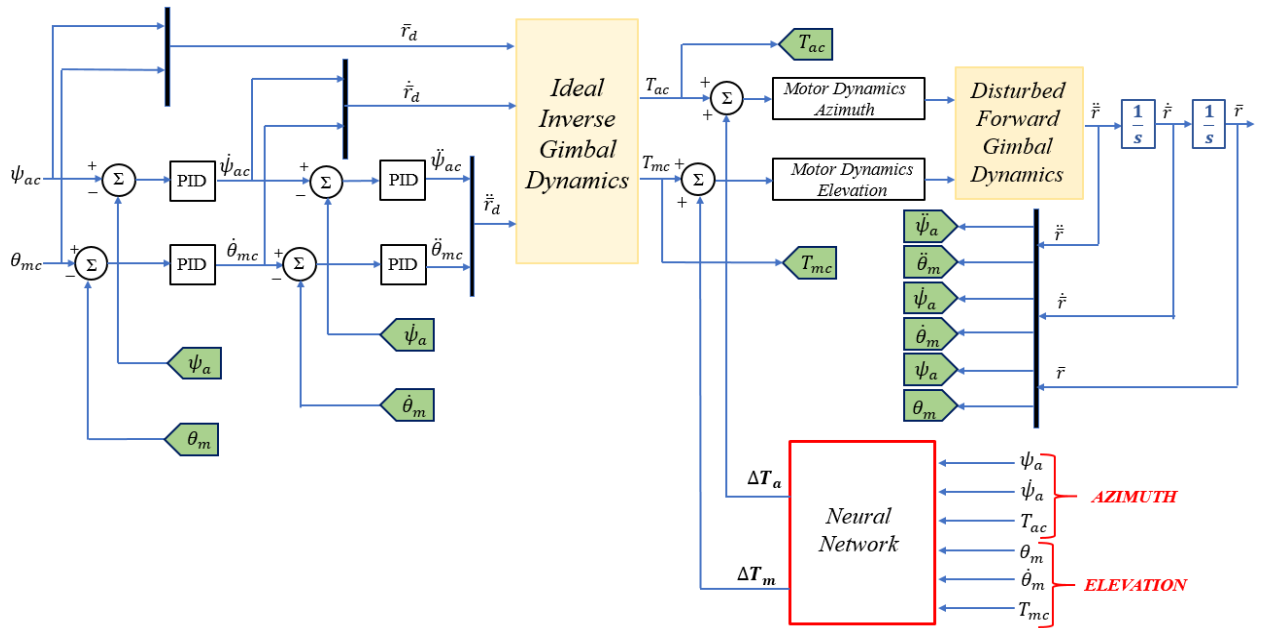


Figure 6.9: Block diagram implementation of NN with cascaded PID controllers in Simulink®

In the examples given below, NN is trained with an amplitude decreasing, frequency increasing sinusoidal wave. Training input changes from 30° to 1° , for the azimuth axis and it changes from 15° to 1° , for the elevation axis with frequency starting from 0.5 Hz and ending at 5 Hz. With this input, almost all ranges in the FOR limits of the experimental set-up are covered (Fig. 6.10).

The feedforward neural network that is designed for this simulation is similar to NNX structure explained in Section 6.1. Input vector is different compared to NNX only. First three rows of the feature vector are the azimuth gimbal's position, velocity and torque output of the *Ideal Inverse Gimbal Dynamics* (T_{ac}); last three rows are the elevation gimbal's position, velocity and torque output of the *Ideal Inverse Gimbal Dynamics* (T_{mc}). An image from the MATLAB® Neural Network Toolbox used for training this network is given in Fig. 6.11

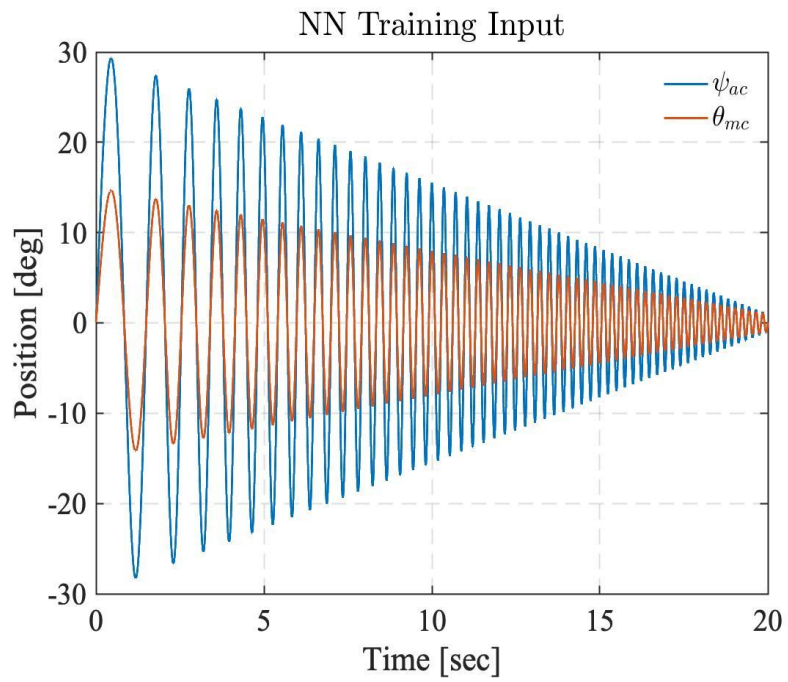


Figure 6.10: NN training input for azimuth and elevation axes

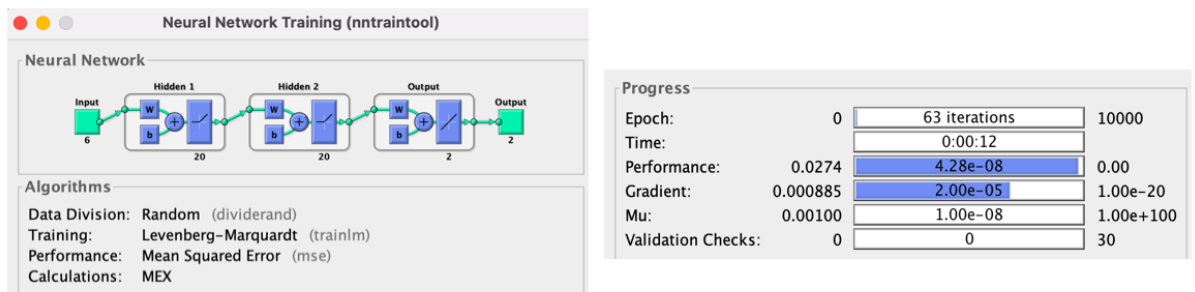


Figure 6.11: An image from MATLAB® Neural Network Toolbox

In the first example, PID controllers are used with the coefficients given in Appendix B, Table B.1. In one scenario, after gimbal reaches the target and get locked onto it, it is expected to perform high frequency and low amplitude motion. Thus, in this example, PID controllers are ideally tuned under a pulse input with $\pm 3^\circ$ amplitude, 2 second period and 50% pulse width. The response of the cascaded PID controller for the tuning input is given in Fig. 6.12 for azimuth and elevation gimbals. Reference input sets used in this section are given in Table 6.1.

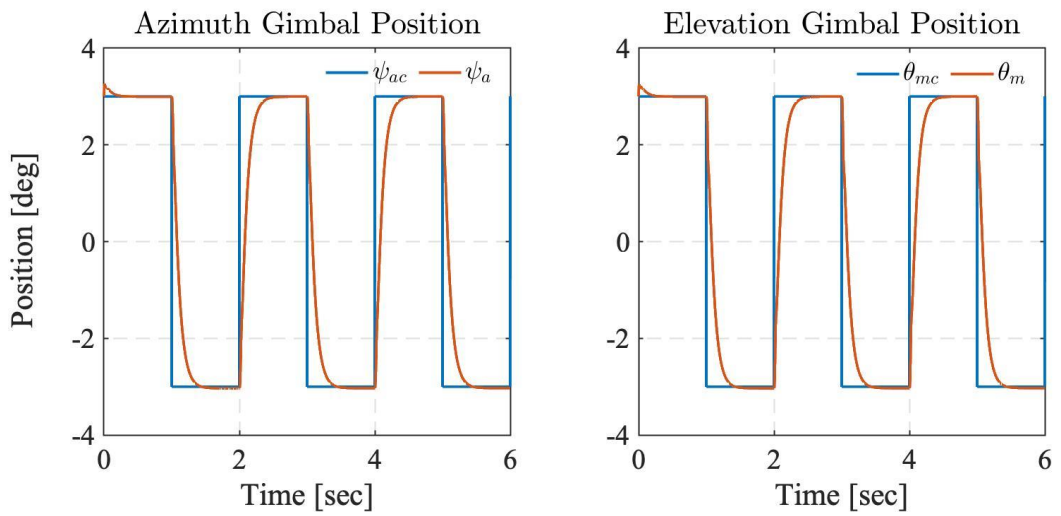


Figure 6.12: Response of the azimuth and elevation gimbals for the pulse input

Table 6.1: Azimuth and elevation gimbal Reference Sets used in Section 6.2

	Azimuth Gimbal	Elevation Gimbal
Reference Set 1	15°@ 1Hz sine	8°@ 1Hz sine
Reference Set 2	1°@ 5Hz sine	1°@ 5Hz sine

During the search pattern (while gimbal is trying to locate the position of the target), it may be required for the gimbal to oscillate with larger amplitudes and slower frequencies. Response of the system with the NN controller is plotted under the Reference Set 1 (Figs. 6.13 and 6.14). Blue line shows the reference input, purple line is the response of the system that runs with PID + NN, orange line is the response of the system that only runs with PID controllers. Without NN, it is observed that azimuth gimbal reaches to 14.4° and elevation gimbal reaches to 7.6° . *NN helps the gimbal to reach the desired position as well as it speeds up the response, decreases time delay.*

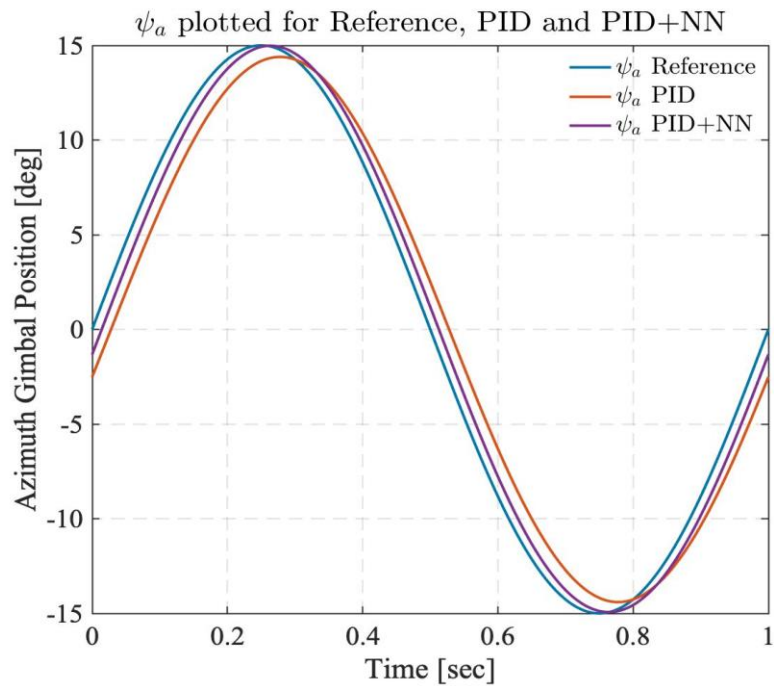


Figure 6.13: Azimuth gimbal position for the sinusoidal input with PID set 1 (15° and 1 Hz)

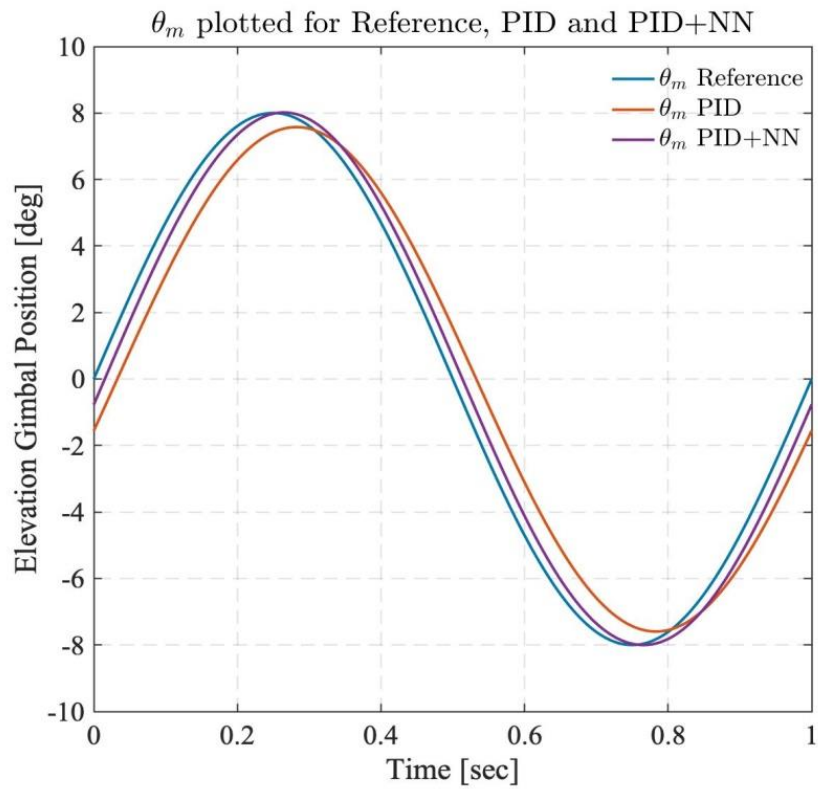


Figure 6.14: Elevation gimbal position for the sinusoidal input with PID set 1 (8° and 1 Hz)

In the second example, PID controllers are used with the coefficients given in Appendix B, Table B.2. Response of the system is plotted under the Reference Set 1 (Figs. 6.15, 6.16). Without NN, it is observed that azimuth gimbal reaches to 12.1° and elevation gimbal reaches to 4.5° .

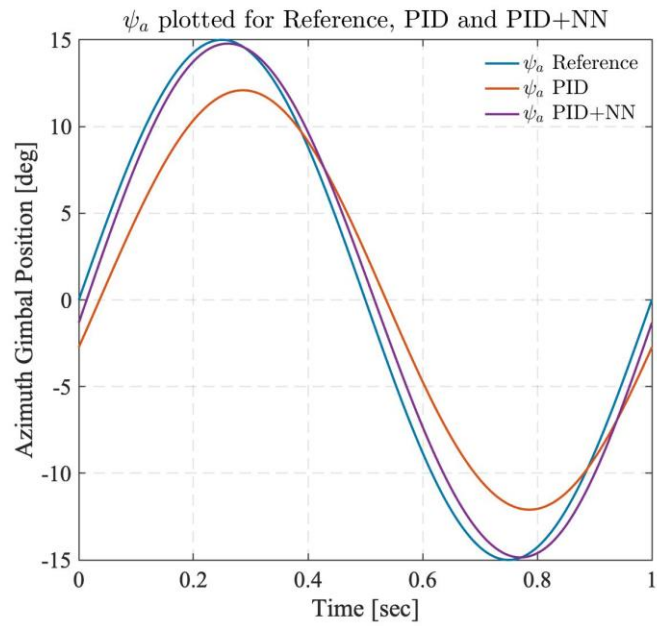


Figure 6.15: Azimuth gimbal position for the sinusoidal input with PID set 2 (15° and 1 Hz)

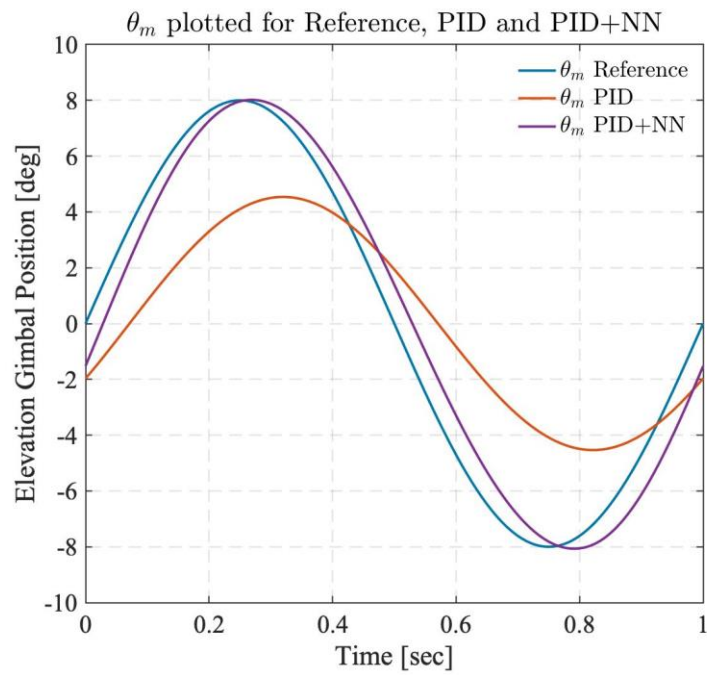


Figure 6.16: Azimuth gimbal position for the sinusoidal input with PID set 2 (8° and 1 Hz)

NN based control structure increases the bandwidth and gain margin of the system. By applying the chirp signal that reaches 20 Hz in 10 seconds with amplitude 1° for azimuth and elevation gimbals, the bandwidth of the system is found. Both, azimuth and elevation gimbals reach to 70.7% of the reference input around 5Hz (2.5th second) as shown in Figs. 6.17 and 6.18. First 5 seconds of the chirp signal and response are shown in the plots.

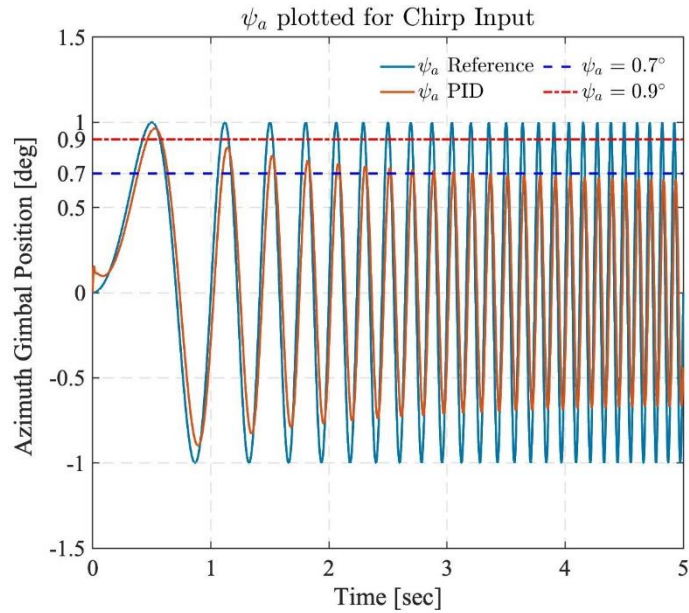


Figure 6.17: Azimuth gimbal response corresponding to chirp signal

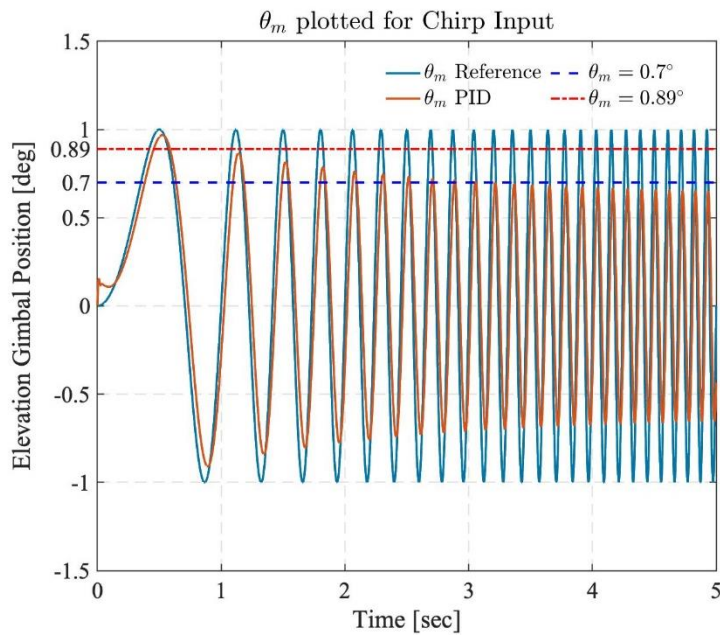


Figure 6.18: Elevation gimbal response corresponding to chirp signal

Azimuth and elevation gimbals are excited with Reference Set 2. It is observed that the response of the system that only runs with PID controllers is around 0.73° , whereas response of the system that runs with PID + NN is better. Azimuth gimbal reaches to 0.9° , elevation gimbal reaches to 0.89° (Fig. 6.19). Motor current applied to the system is within the saturation limits in both cases. NN based controller, increases the bandwidth of azimuth and elevation gimbals approximately 4.2 times for the sinusoidal wave with 1° amplitude.

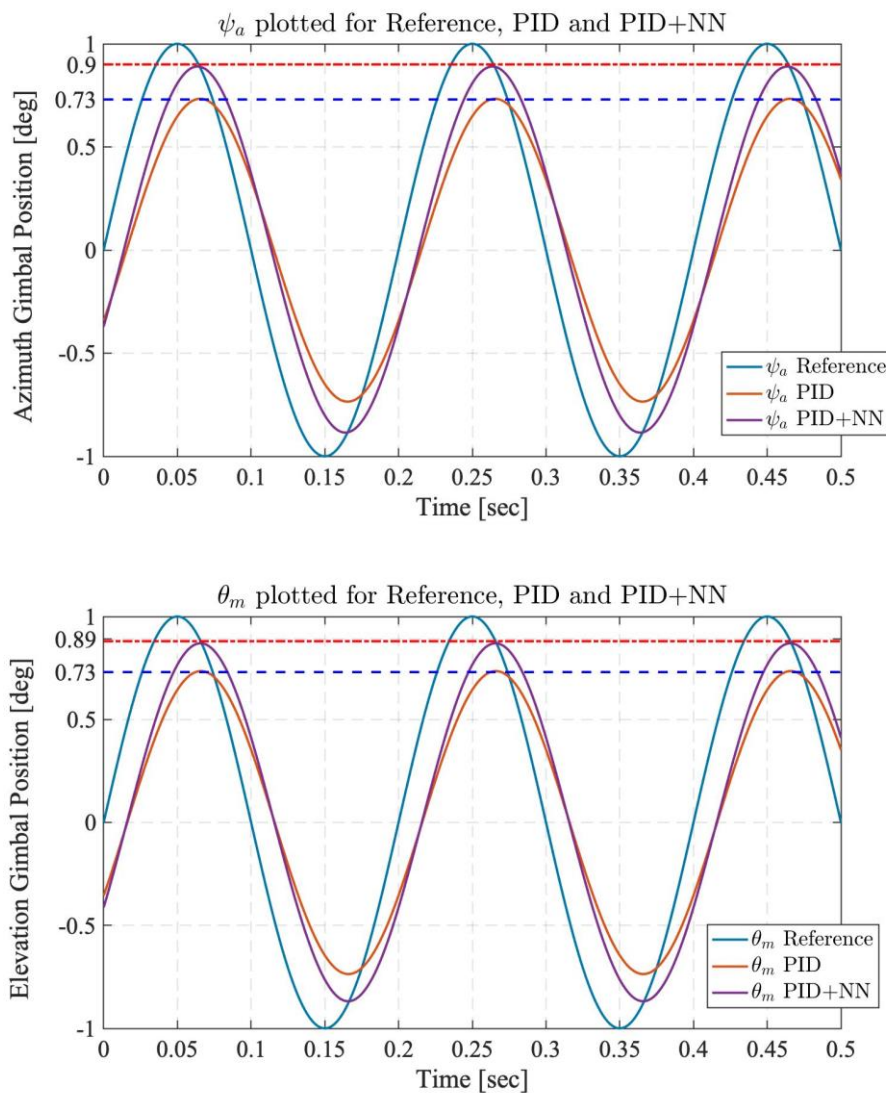


Figure 6.19: Azimuth and elevation gimbal's response for the Reference Set 2

6.3 ADRC with ESO Implementation for Inverse and Forward Gimbal Dynamics

Active Disturbance Rejection Control (ADRC) theory is invented by J. Han in [35]. It is a method to replace the conventional PID controller. This method is applicable for systems having double integral structures (Chapter 2, Section 2.4). It is composed of three main parts. First part is the *Transient Profile Generator*, given by Eqns. 6.5 and 6.6. Second part is the *Nonlinear Weighted Sum*, given by Eqns. 6.7, 6.8 and 6.9. *Nonlinear Weighted Sum* acts like a simple PD type controller (proportional derivative). Third part is *Total Disturbance Estimation and Rejection* by using *ESO*, explained with Eqns. 6.10, 6.11. This method is chosen to be implemented in our system; because it successfully estimates unmodeled dynamics and disturbances. This method is used separately for each channel. Equations for a single channel are given below for our system.

Eqns. 6.5 and 6.6 introduce the implementation of a nonlinear derivative operation. v_1 is the desired trajectory (i.e., desired position, ψ_a and θ_m), v_2 is its derivative (i.e., desired velocity, $\dot{\psi}_a$ and $\dot{\theta}_m$), v is the reference input (i.e., desired position references, ψ_{ac} and θ_{mc}), r is the learning rate that speeds up or slows down the transient profile.

$$\dot{v}_1 = v_2 \quad (6.5)$$

$$\dot{v}_2 = -r \text{sign}\left(v_1 - v + \frac{v_2 |v_2|}{2r}\right) \quad (6.6)$$

Commands generated from Eqns. 6.5 and 6.6, (v_1 and v_2), are used to form the error signals (e_1 and e_2), that are used as the reference acceleration input ($\ddot{\psi}_a$ and $\ddot{\theta}_m$) for the *Inverse Gimbal Dynamics*. k_1 and k_2 are the parameters to be tuned.

$$e_1 = v_1 - r \tag{6.7}$$

$$e_2 = v_2 - \dot{r} \tag{6.8}$$

$$\dot{r} = k_1 e_1 + k_2 e_2 \tag{6.9}$$

The block diagram composed of the *Transient Profile Generator* and *Nonlinear Weighted Sum with Inverse and Forward Gimbal Dynamics* is given in Fig. 6.20.

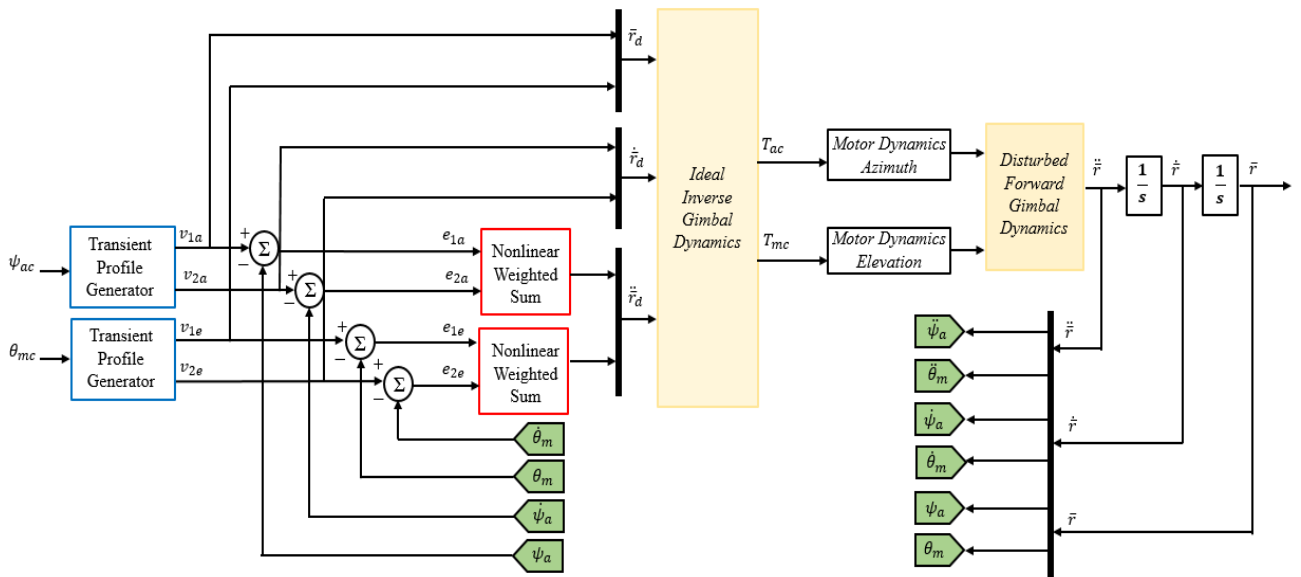


Figure 6.20: Block diagram implementation of *Transient Profile Generator* and *Nonlinear Weighted Sum with Inverse and Forward Gimbal Dynamics* in Simulink®

Consider the state space representation of the system expressed in Eqn. 6.10. $f(x_1, x_2, w(t), t)$ is the state dependent unmodeled dynamics and disturbances acting on the system. u is the control input and y is the system output needs to be controlled.

$$\dot{x}_1 = x_2 \tag{6.10}$$

$$\dot{x}_2 = f(x_1, x_2, w(t), t) + bu$$

$$y = x_1$$

Creating an additional state variable x_3 to represent total disturbances in the system $F(t)$, and writing $\dot{F}(t) = G(t)$, a new set of state space equations are expressed in Eqn. 6.11. System is always observable.

$$\dot{x}_1 = x_2 \tag{6.11}$$

$$\dot{x}_2 = x_3 + bu$$

$$\dot{x}_3 = G(t)$$

$$y = x_1$$

The state observer (ESO), is constructed with the set of equations given in Eqn. 6.12. z_1, z_2 and z_3 are the outputs of ESO. z_1 is the observed position, z_2 is the observed velocity and z_3 is the estimated disturbances. Observer gains in Eqn. 6.12 are linear. Observer parameters that needs to be tuned are β_{01}, β_{02} and β_{03} . Controller parameter that should be tuned is b (or b_0). The block diagram implementation of ADRC with *Inverse and Forward Dynamics* is shown in Fig. 6.21.

$$e = z_1 - y \quad (6.12)$$

$$\dot{z}_1 = z_2 - \beta_{01}e$$

$$\dot{z}_2 = z_3 + bu - \beta_{02}e$$

$$\dot{z}_3 = -\beta_{03}e$$

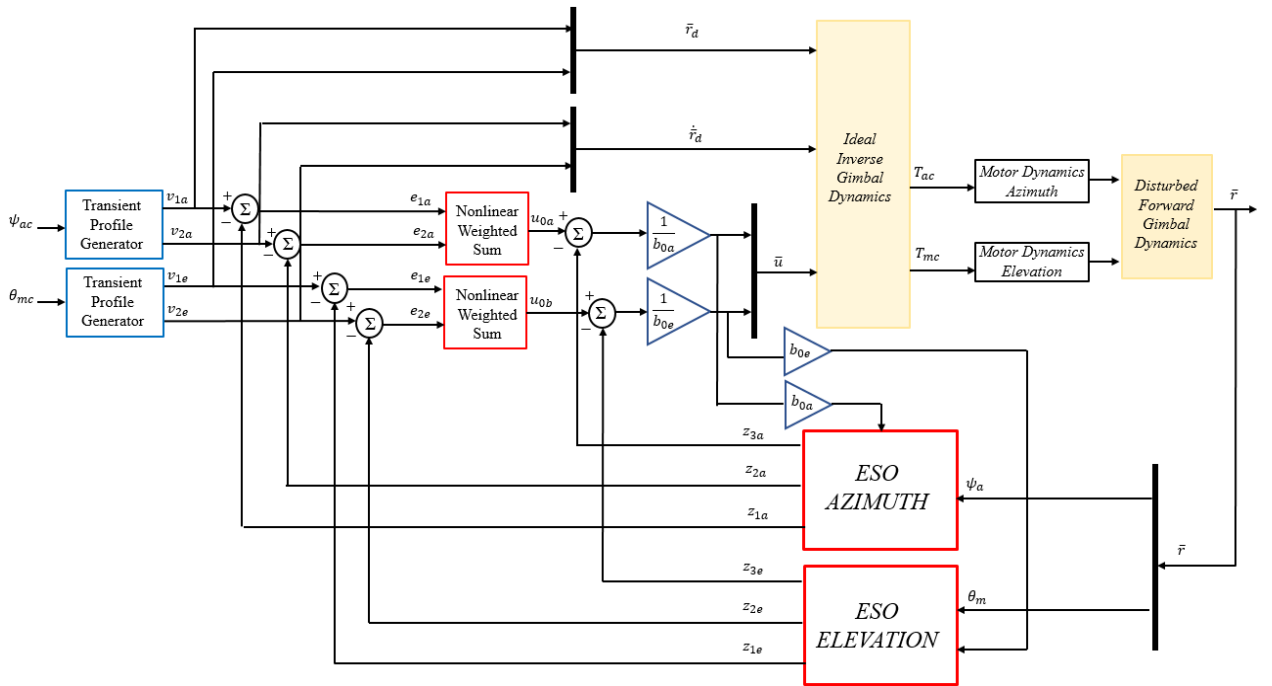


Figure 6.21: Block diagram implementation of ADRC with *Inverse* and *Forward Gimbal Dynamics* in Simulink®

Instead of using a NN based controller, disturbance torque compensation can also be supplied from using *Ideal Inverse Dynamics*. By sending the output of *Disturbed Forward Gimbal Dynamics* to the second *Ideal Inverse Gimbal Dynamics* block, the differential torque between the first *Ideal Inverse Gimbal Dynamics* and the *Second Ideal Inverse Gimbal Dynamics* can be calculated and added to system. In other

words, with this approach, instead of training a NN with the data obtained from *Ideal Inverse Dynamics*, the training data can be directly supplied from *Ideal Inverse Dynamics*. However, this approach is not applicable as wide as the NN-controllers suggested in this thesis especially for relatively high frequency reference inputs (see Figs. below). The block diagram implementation of cascaded PID controllers with *Inverse Dynamics* based compensation is shown in Fig. 6.22.

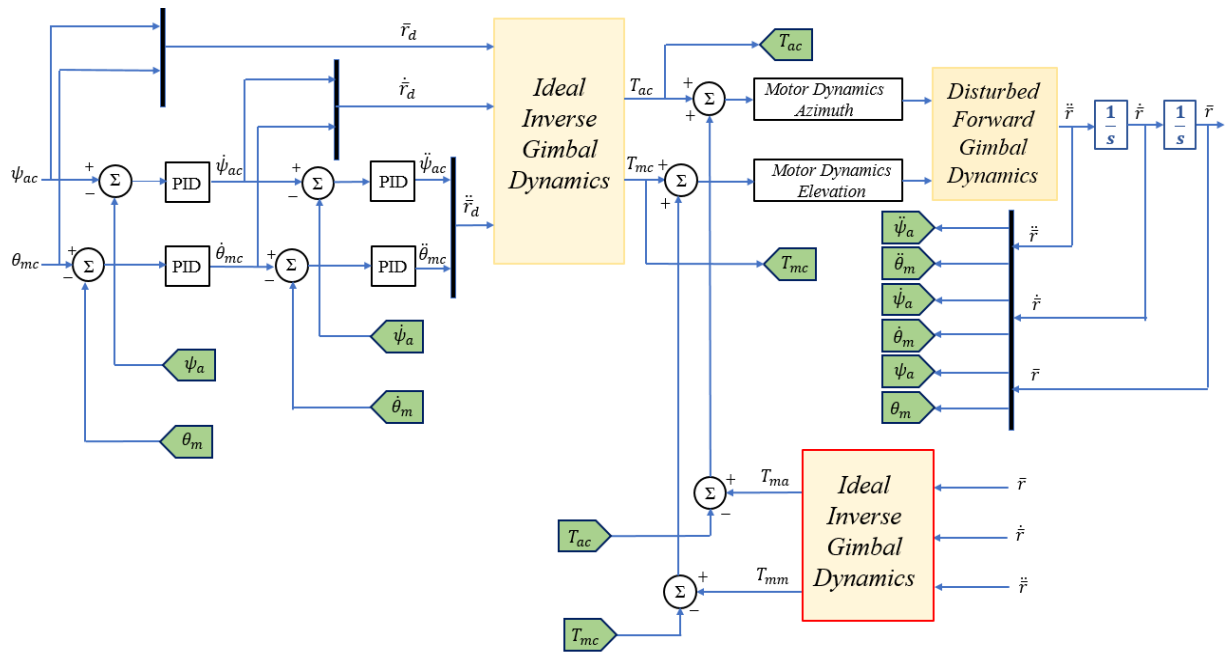


Figure 6.22: Block diagram implementation of cascaded PID controllers with *Inverse Dynamics* based compensation in Simulink®

In the following examples, comparisons between PID, NN-based controller (with Method 2), ADRC with ESO and inverse model based controller are provided for different reference input sets. Constants associated with PID and ADRC controllers are given in Appendix B, Tables B.1, B.3. Reference input sets used in this section are given in Table 6.2. For the first round of experiments, frequency of the reference is held constant at 3 Hz. Amplitude of the sinusoidal wave is varied from 2° to 11° . For the second round of experiments, amplitude of the reference is held constant at

5°. Frequency of the sinusoidal wave is varied from 1 Hz to 5 Hz. The ADRC controller is optimally tuned under a pulse input with $\pm 3^\circ$ amplitude, 2 seconds period and 50% pulse width. The response of the ADRC controller for this input is given in Fig. 6.23 for azimuth and elevation gimbals.

Table 6.2: Azimuth and elevation gimbal Reference Sets used in Section 6.3

	Azimuth Gimbal	Elevation Gimbal
<i>Reference Set 1</i>	2°@ 3Hz sine	2°@ 3Hz sine
<i>Reference Set 2</i>	4°@ 3Hz sine	4°@ 3Hz sine
<i>Reference Set 3</i>	6°@ 3Hz sine	6°@ 3Hz sine
<i>Reference Set 4</i>	8°@ 3Hz sine	8°@ 3Hz sine
<i>Reference Set 5</i>	11°@ 3Hz sine	11°@ 3Hz sine
<i>Reference Set 6</i>	5°@ 1Hz sine	5°@ 1Hz sine
<i>Reference Set 7</i>	5°@ 2Hz sine	5°@ 2Hz sine
<i>Reference Set 8</i>	5°@ 3Hz sine	5°@ 3Hz sine
<i>Reference Set 9</i>	5°@ 4Hz sine	5°@ 4Hz sine
<i>Reference Set 10</i>	5°@ 5Hz sine	5°@ 5Hz sine

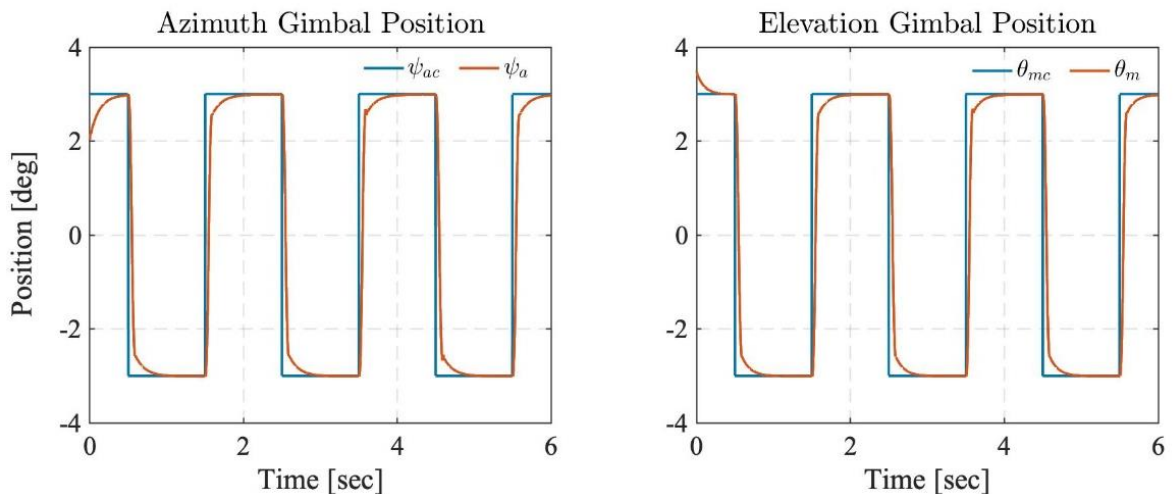


Figure 6.23: Response of the azimuth and elevation gimbals for the pulse train input with ADRC

It has been observed that, at smaller amplitudes ADRC controller decreases the time delay in the response. Tracking performance of the ADRC controller is the best in small amplitudes. However, as the amplitude increases, ADRC controller produces a larger phase difference in the response compared to PID, NN-based and inverse model based controllers. The response of ADRC is input dependent (mean tracking error varies).

Figs. 6.24, 6.25, 6.26 show the response of the aforementioned controllers for the Reference Sets 1, 3, 5 for the azimuth gimbal. The equations used for calculating and normalizing mean tracking and peak position errors in MATLAB® are given in Eqn. 6.13. Fig. 6.27 shows the change in these errors for each controller corresponding to Reference Sets 1-5. Tables 6.3-6.5 give the percent improvement of mean tracking and peak errors wrt. PID controller, (m) and (p), for each controller. The equations used to calculate these percentage errors are given in Eqn. 6.14. Percent decrease in Tables 6.3-6.5 indicates the percent how much each controller decreases mean tracking and peak errors wrt. PID controller.

$$e_{mean} = \frac{mean|r_d - r|}{max(r_d)} \quad (6.13)$$

$$e_{peak} = \frac{|max(r_d) - max|r||}{max(r_d)}$$

$$m = \left(\frac{e_{mean PID} - e_{mean controller}}{e_{mean PID}} \right) \times 100 \quad (6.14)$$

$$p = \left(\frac{e_{peak PID} - e_{peak controller}}{e_{peak PID}} \right) \times 100$$

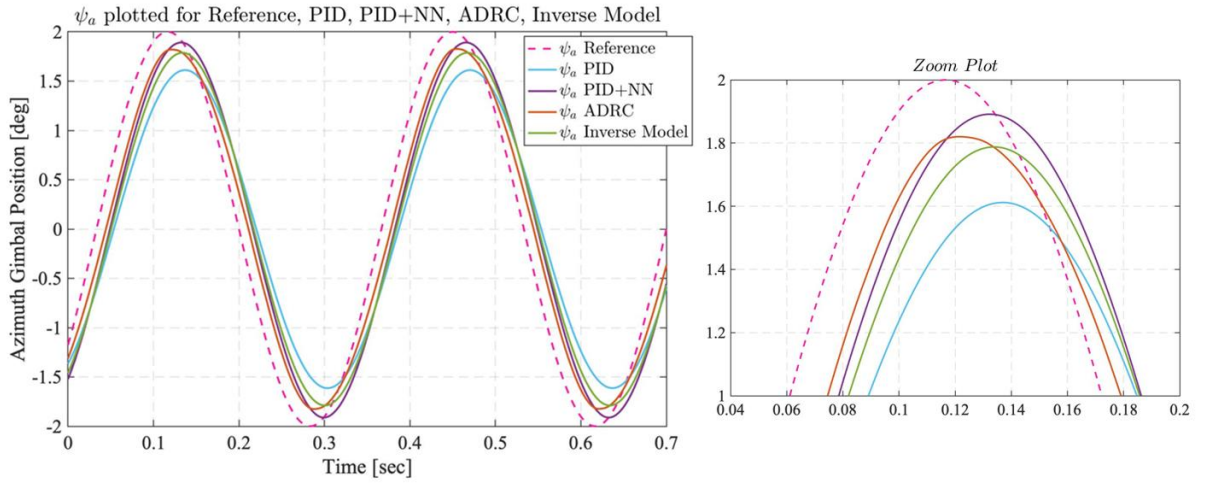


Figure 6.24: Response of the azimuth gimbal for Reference Set 1

Table 6.3: Percent improvement (azimuth) wrt. PID controller for Reference Set 1

	<i>Percent Decrease (%)</i>	
	Mean Track Error	Peak Error
<i>PID+NN</i>	23.35	77.2
<i>ADRC</i>	48.15	55.13
<i>Inverse Model</i>	16.56	45.46

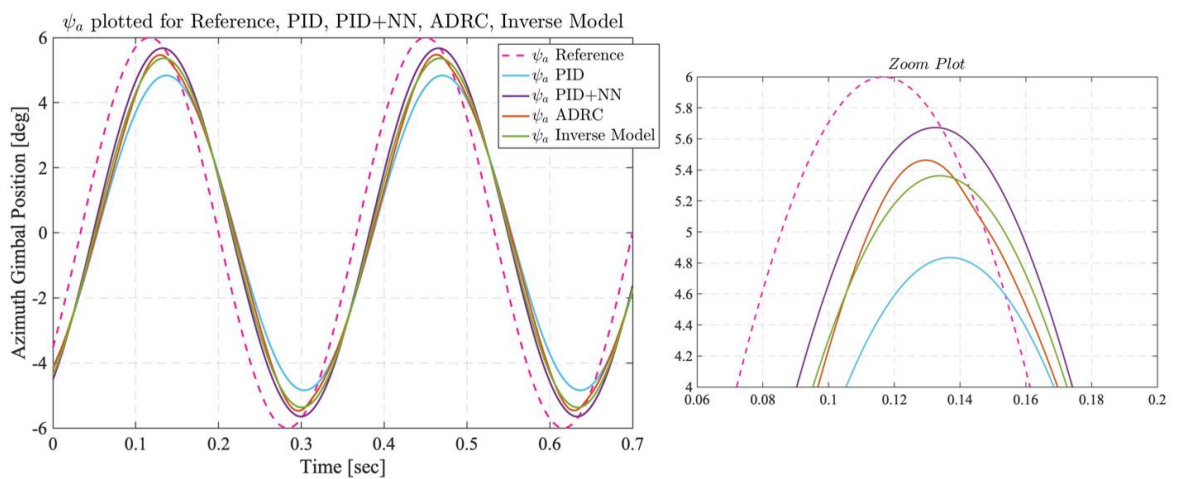


Figure 6.25: Response of the azimuth gimbal for Reference Set 3

Table 6.4: Percent improvement (azimuth) wrt. PID controller for Reference Set 3

	<i>Percent Decrease (%)</i>	
	Mean Track Error	Peak Error
<i>PID+NN</i>	23.81	71.78
<i>ADRC</i>	15.56	54.56
<i>Inverse Model</i>	16.56	45.46

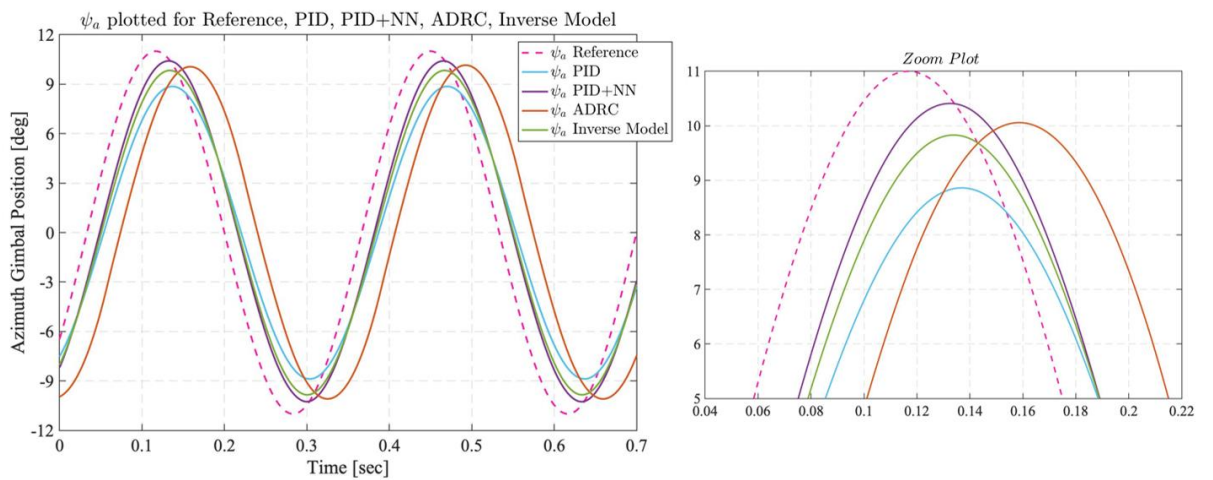


Figure 6.26: Response of the azimuth gimbal for Reference Set 5

Table 6.5: Percent improvement (azimuth) wrt. PID controller for Reference Set 5

	<i>Percent Decrease (%)</i>	
	Mean Track Error	Peak Error
<i>PID+NN</i>	24.28	72.15
<i>ADRC</i>	-89.92	60
<i>Inverse Model</i>	16.56	45.46

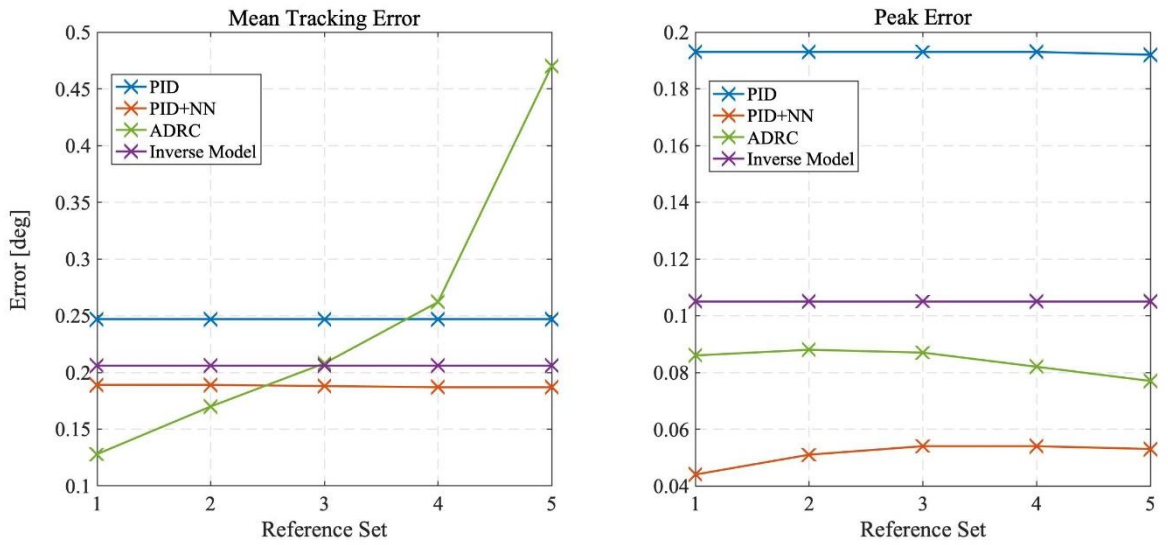


Figure 6.27: Mean tracking and peak errors (azimuth) of each controller for Reference Sets 1-5

In the second round of experiments, similar to what is seen before, it has been observed that the response of ADRC is not better than the simple PID controller in each case. Figs. 6.28, 6.29, 6.30 show the response of the controllers for the Reference Sets 6, 7, 10 for the azimuth gimbal. Tables 6.6-6.8 give the p and m values for each controller for the Reference Sets 6, 7, 10. Fig. 6.31 shows the changes in mean tracking and peak errors of each controller for Reference Sets 6-10.

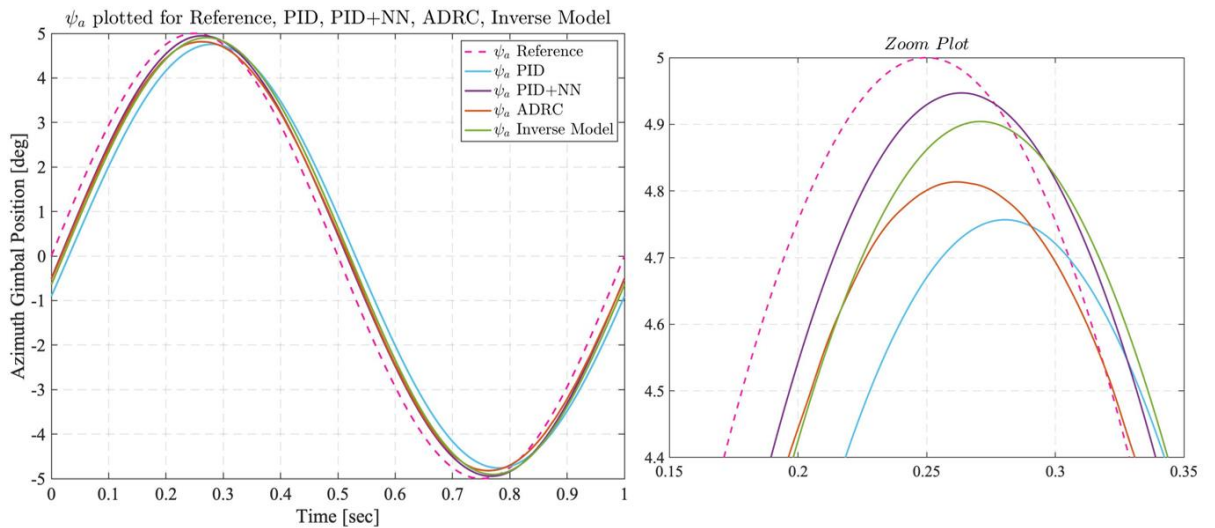


Figure 6.28: Response of the azimuth gimbal for Reference Set 6

Table 6.6: Percent improvement (azimuth) wrt. PID controller for Reference Set 6

	<i>Percent Decrease (%)</i>	
	Mean Track Error	Peak Error
<i>PID+NN</i>	48.68	77.8
<i>ADRC</i>	45.65	25.03
<i>Inverse Model</i>	31.61	61.11

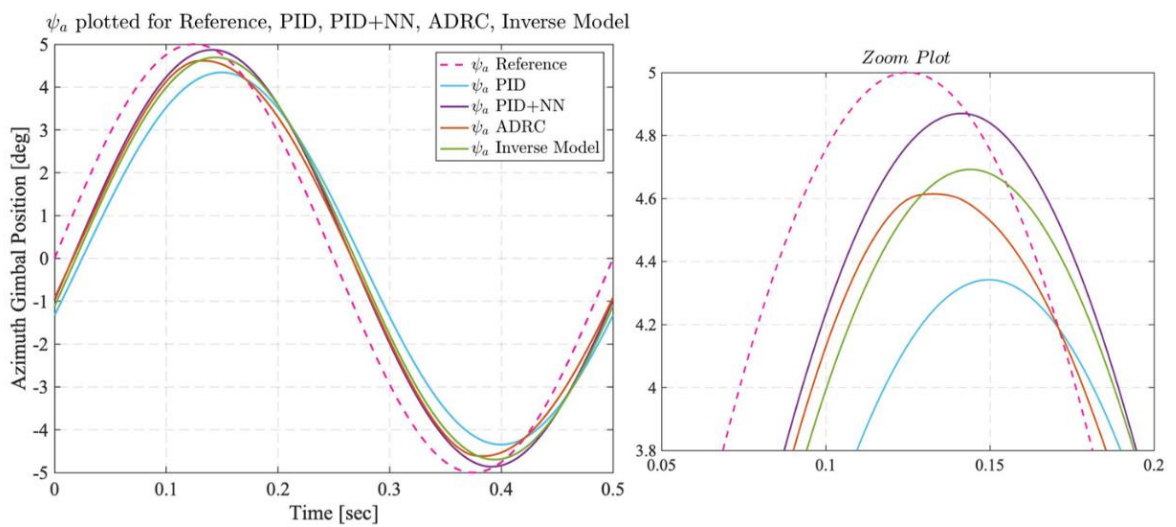


Figure 6.29: Response of the azimuth gimbal for Reference Set 7

Table 6.7: Percent improvement (azimuth) wrt. PID controller for Reference Set 7

	<i>Percent Decrease (%)</i>	
	Mean Track Error	Peak Error
<i>PID+NN</i>	35.92	80.11
<i>ADRC</i>	38.23	41.22
<i>Inverse Model</i>	24.31	53.42

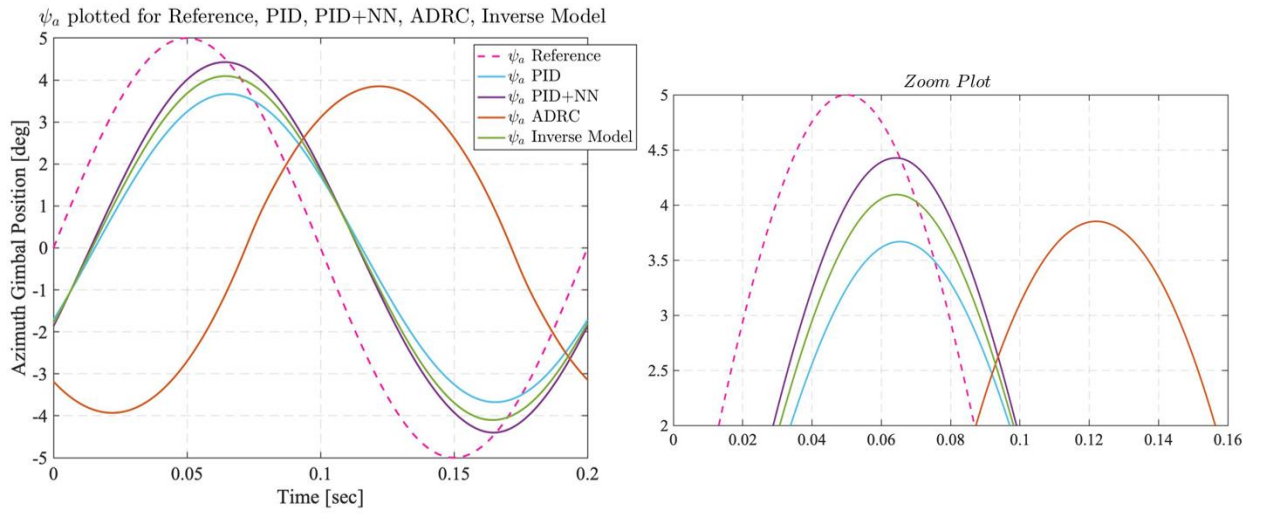


Figure 6.30: Response of the azimuth gimbal for Reference Set 10

Table 6.8: Percent improvement (azimuth) wrt. PID controller for Reference Set 10

	<i>Percent Decrease (%)</i>	
	Mean Track Error	Peak Error
<i>PID+NN</i>	12.39	56.76
<i>ADRC</i>	-231.96	19.29
<i>Inverse Model</i>	9.14	32.14

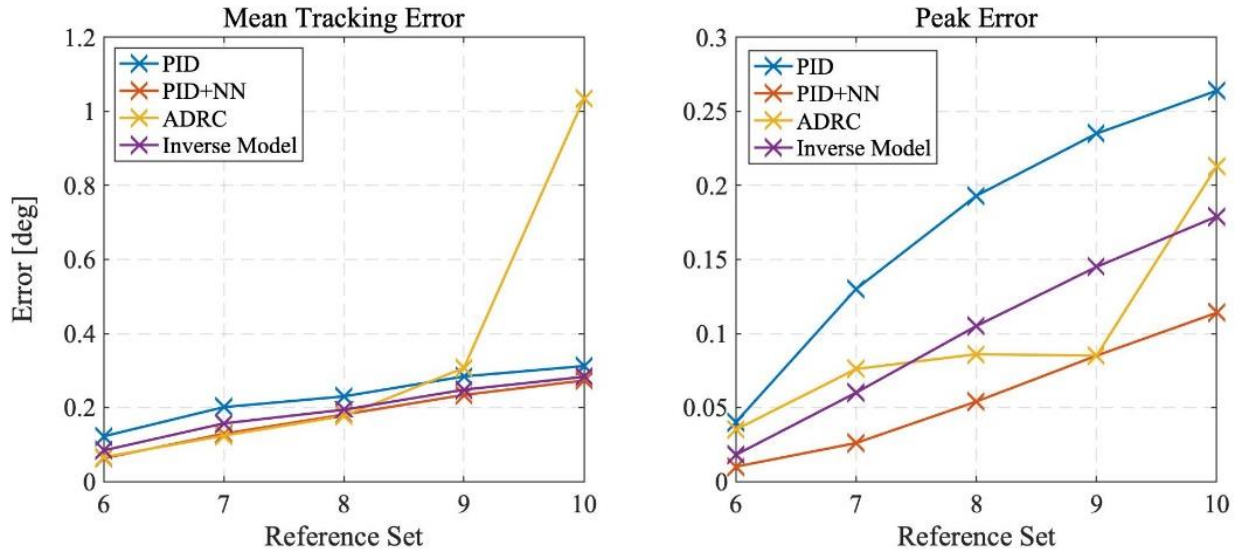


Figure 6.31: Mean tracking and peak errors (azimuth) of each controller for Reference Sets 6-10

For the third round of experiments, response of cascaded PID, ADRC, NN based and Inverse model controllers are investigated for the disturbances resulting from model parameter uncertainties. Inertia and distance parameters are disturbed from their nominal values to create CoG, rotation axis offsets and dynamical mass unbalance. NN is trained for the undisturbed distance and inertia parameters. In this example, disturbance compensation ability of the proposed algorithm for the untrained data can also be observed. As a consequence of *Parameter Sensitivity Analysis*, some of the most influential parameters affecting the system/on the system are disturbed (Table 6.9). Parameters are disturbed approximately within their 3σ width.

Table 6.9: Disturbed model parameters

J_{axy}, J_{ayx}	-0.08 kgm^2
J_{mxz}, J_{mzx}	0.01 kgm^2
$a_{m_x}, G_{m_x}, G_{a_x}$	0.015 m
J_{azx}, J_{axz}	-0.01 kgm^2
G_{m_z}, G_{a_y}	-0.015 m

Fig. 6.32, shows the response of the azimuth gimbal for the Reference Set 2 under parameter disturbances.

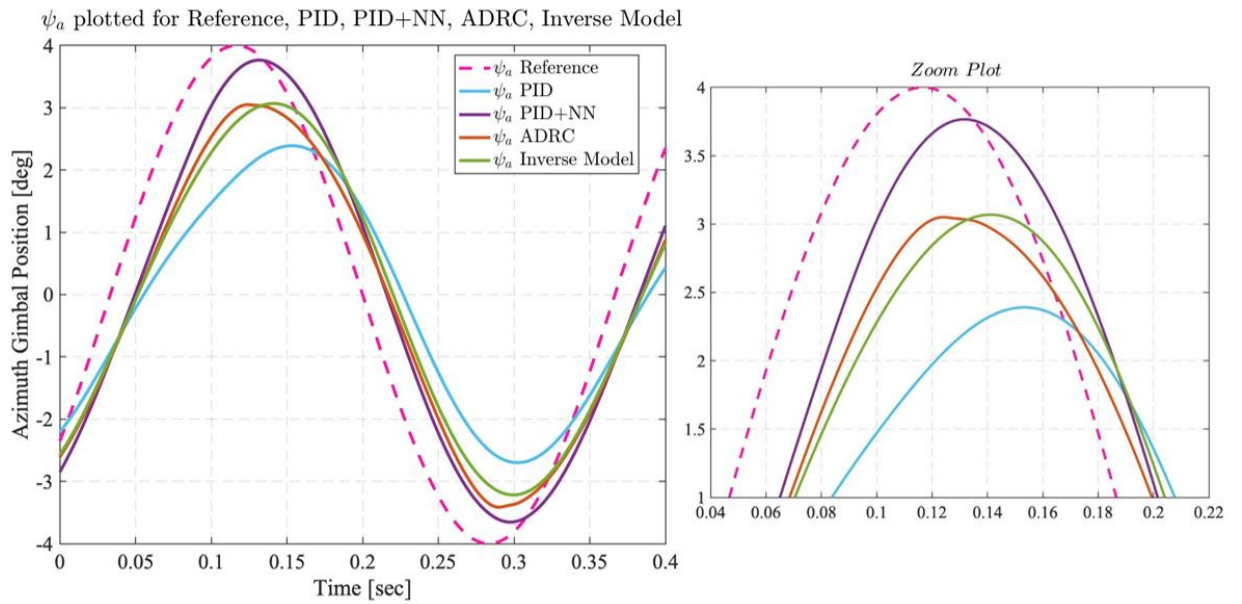


Figure 6.32: Response of the azimuth gimbal for Reference Set 2 under model parameter disturbances

Mean tracking error of each controller are plotted for the undisturbed/disturbed cases of model parameters in Fig. 6.33. Blue columns correspond to undisturbed cases of model parameters and results represented by orange columns are performed under disturbed parameters. According to Figs. 6.32 and 6.33, NN based controller performs the best both in tracking and peak errors even if it is not trained under this disturbance that we artificially created after the training. It is interesting to observe that, mean tracking error for NN based controller stays the same under this artificially created disturbance. Performances of PID, ADRC and Inverse Model controllers decrease by 31%, 25% and 18%, respectively in terms of mean tracking error for Reference Set 2. On the other hand, performance of the NN based controller stays the same.

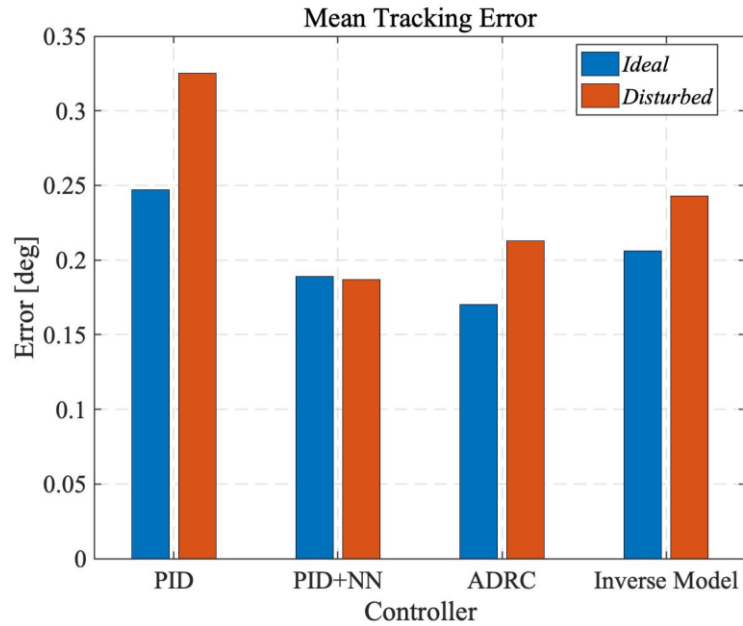


Figure 6.33: Changes in the mean tracking error of the azimuth gimbal for Reference Set 2: orange columns represent the mean tracking error for the experiment performed with disturbed model parameters

Among cascaded PID, NN-based, ADRC and inverse model based controllers, according to mean and peak value figures and tables, best controllers are ADRC ve NN-based controllers. In terms of peak error, NN-based controller is always better than ADRC for the azimuth axis.

ADRC is input dependent. Based on the reference set, ADRC can perform better/worse than the simple PID controller. NN-based controller is always better than the cascaded PID. *ADRC requires tuning and design effort for different reference sets (Fig. 6.30)*. It is difficult and it takes time to tune the coefficients of ADRC controller. Even though ADRC controller decreases the time delay in the response compared to other controllers, it is not valid for every reference input. It can also increase the time delay in the response (Fig. 6.26). Disturbance torques present in the system are coupled coming from two different axes. This is verified by the data collected from the experimental set-up in Chapter 5. **ADRC controller**

uses distinct ESOs for each channel. Instead, in the proposed algorithm, there is only one NN and it works as a MIMO disturbance torque compensator. Inputs of the NN come from both the azimuth and elevation axes.

PID and ADRC controllers are designed optimally. On the other hand, one cannot say NN being optimal. It depends on the training dataset, layer and neuron numbers, training algorithm. So, it has a chance to improve its performance further. Especially, training set has an important effect on the performance of the NN in our system. ADRC is basically applicable for double integral systems. In our system, *Inverse Dynamics* is ideal; however there is disturbance in the *Forward Plant*. So, the double integral structure is in a way lost. This might be another reason why ADRC controller does not work as well as NN based controller in our system.

6.4 Implementation of Method 2 for Real-Time Experiments

Proposed control strategy with Method 2 (compensation by the torque input channel) is tested in the experimental set-up by using xPC Target. Block diagram representation given in Fig. 6.9 is implemented on the host PC. Input for the real system is \bar{V}_c . During experiments, gyro data is used by passing it through a 100 Hz low-pass filter. While obtaining the training data for the NN, acceleration is derived by using the filtered version of the gyro data and taking derivative at every 100 point. Neural network structure used in the experiments is same as the ones used in Simulink®. There are two layers in the NN, each layer is composed from 64 neurons. Comparisons of the proposed algorithm with cascaded PID controllers are shown with figures using the data obtained from the physical system.

In Example 1, NN is trained with the inputs given in Fig. 6.34 (red crosses), sine waves are used for the azimuth gimbal and cosine waves are used for the elevation

gimbal. PID coefficients are given in Appendix B, Table B.4. It is observed that the response of the system that runs with PID + NN is better compared to response of the system that runs only with PID controllers for the training input (Fig. 6.34, red crosses) and for the input that is outside the range of training set (Fig. 6.34, blue circles). Figure 6.35, shows the response of the azimuth gimbal for the training input.

The orange line in Fig. 6.34, corresponds to $y = 3x + 14$ line. This is the reason $8^\circ @ 2\text{Hz}$ and other amplitudes around this reference input are chosen to be studied with the NN trained in Example 1.

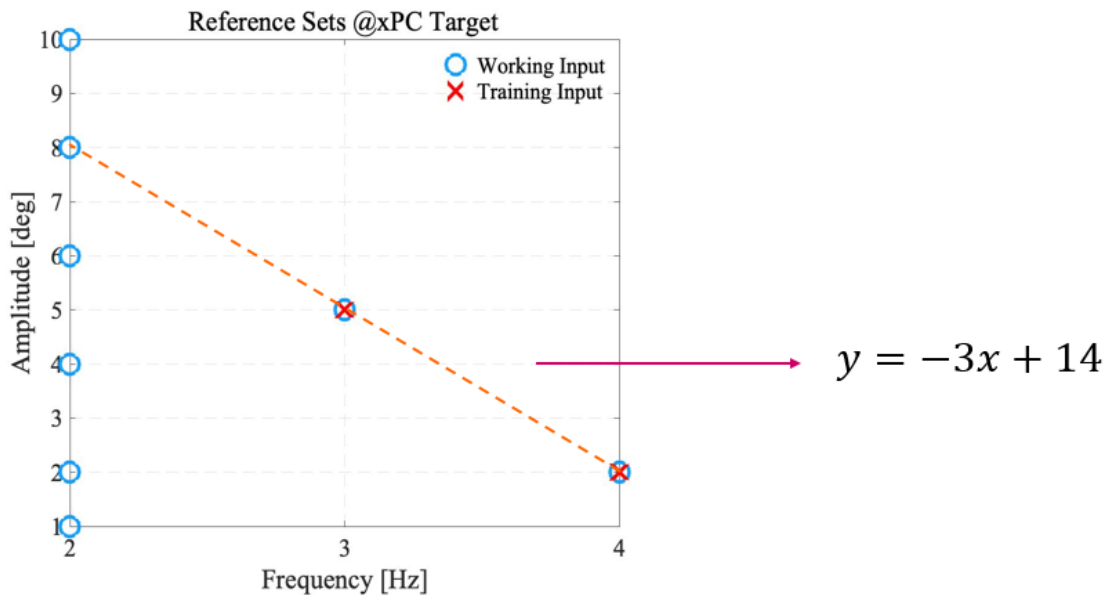


Figure 6.34: Reference Sets used with the physical gimbal for Example 1

Figure 6.35, shows the response of the azimuth gimbal for the training input ($5^\circ @ 3\text{Hz}$). Figure 6.36 shows the response of the azimuth and elevation gimbals for the reference input ($6^\circ @ 2\text{Hz}$).

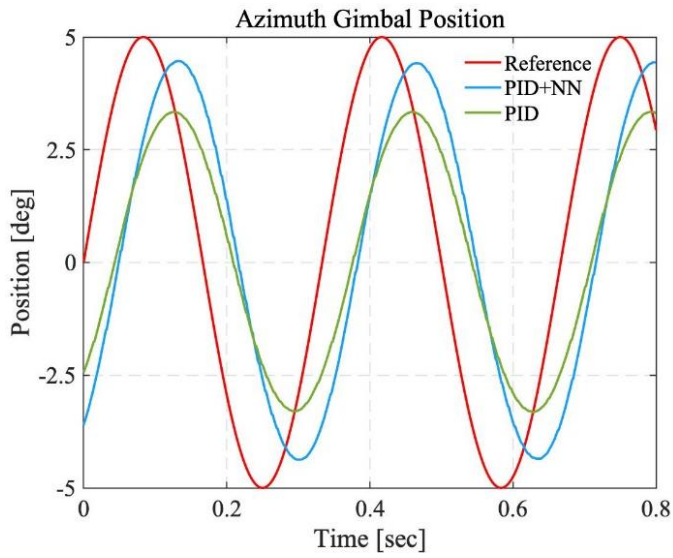


Figure 6.35: Response of the azimuth gimbal for the training input ($5^\circ@3\text{Hz}$) with NN based controller

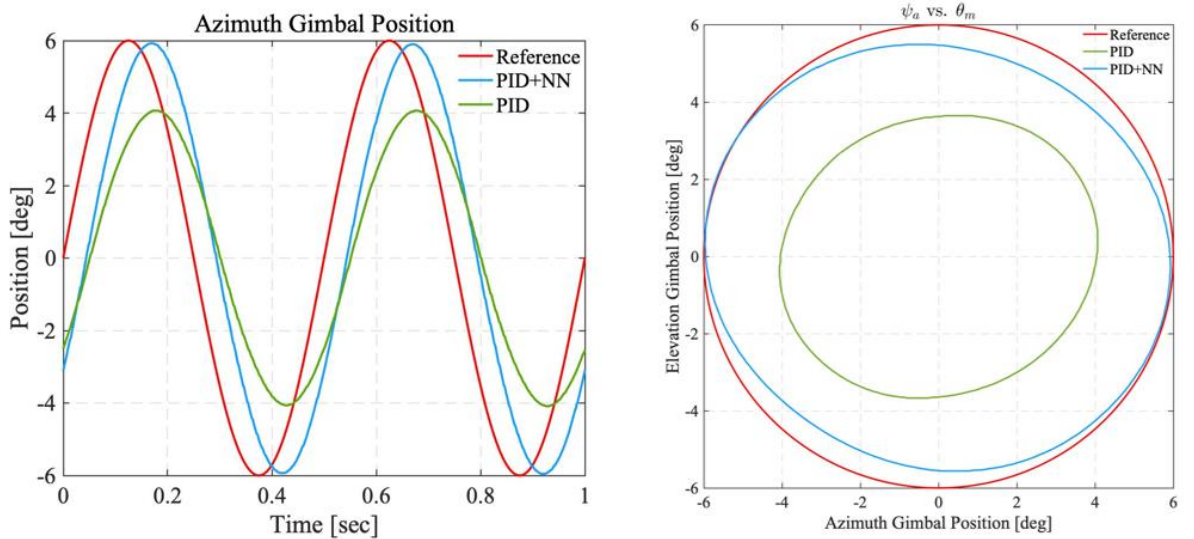


Figure 6.36: Response of the azimuth and elevation gimbals for the reference input ($6^\circ@2\text{Hz}$) with NN based controller

In Example 2, NN is trained and tested with the input sets given in Table 6.10. PID coefficients are given in Appendix B, Table B.5.

Table 6.10: Azimuth and elevation gimbal Reference Sets used for Example 2

	Azimuth Gimbal	Elevation Gimbal
<i>Reference Set 1</i>	2°@ 5Hz sine	2°@ 5Hz cosine
<i>Reference Set 2</i>	3°@ 5Hz sine	3°@ 5Hz cosine

By applying chirp signal for azimuth and elevation gimbals with amplitude 2°, the bandwidth of the set-up is found. Elevation gimbal response corresponding to chirp signal is given in Fig. 6.37 (chirp signal reaches 20 Hz in 10 seconds with amplitude 2°). Elevation gimbal reaches to 1.9° approximately around 3 Hz and to 1.5° around 5Hz. First 6 seconds of the chirp signal and response are shown in the plot.

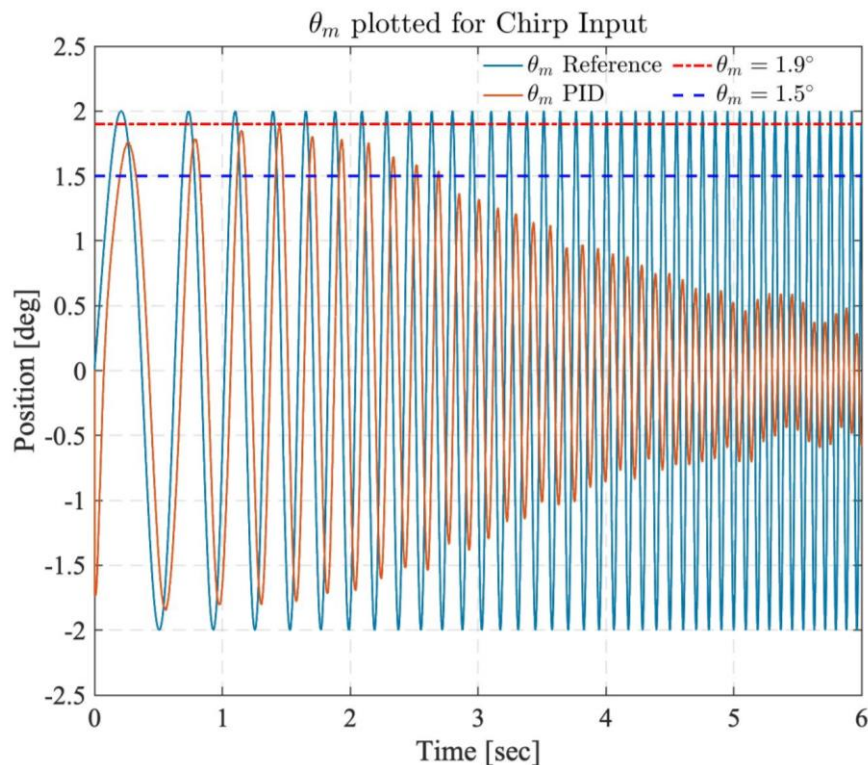


Figure 6.37: Elevation gimbal response corresponding to chirp signal in xPC Target with PID controllers

In Fig. 6.37, as the frequency increases response of the system tends to be more anti-symmetric wrt. x-axis and shows a different oscillation pattern in terms of shape and magnitude. This is the implication of having a highly nonlinear system.

Response of the elevation gimbal for the Reference Set 1 is shown in Fig. 6.38. NN based controller can reach to 1.95° and PID controller can reach to 1.55° around 5Hz. NN based controller increases the bandwidth of the system approximately around 66%. This NN, besides increasing the amplitude of the response, also decreases the phase difference for Reference Set 1.

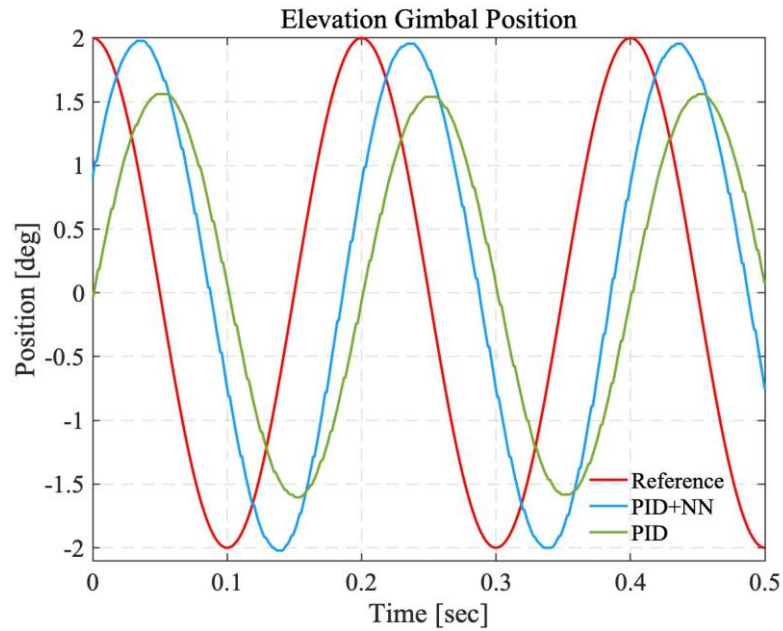


Figure 6.38: Elevation gimbal response corresponding to Reference Set 1 with NN based controller

6.5 Method 3: NN Based Control Structure with Inverse and Forward Gimbal Dynamics (Acceleration Compensation)

This section is about disturbance torque compensation of the system that is composed of “*Ideal Inverse Dynamics-Disturbed Forward Dynamics-Ideal Inverse Dynamics*” sequence in MATLAB®. Compensation is provided through the acceleration input channel. For a detailed explanation regarding Method 3, see Appendix C.

In this method, disturbance torque compensation is done by adding the output of the NN to the reference acceleration which is one of the inputs of the first *Ideal Inverse Dynamics* block. In simulations, Eqns. 6.3 and 6.4 represent disturbances in the *Disturbed Forward Dynamics* block (same as Section 6.2). NN training is performed using the block diagram given in Fig. 6.39. The training data set of the neural network is $\{(r, \dot{r}, \ddot{r}, 1), \Delta \ddot{r}, t \in [0, t_f]\}$. Output of the NN is the differential acceleration $\Delta \ddot{r}$, (Eqn. 6.15). The input-output relationship of the NN is plotted in Fig. 6.40. The proposed design procedure of the NN-based control strategy with Method 3 is presented in the block diagram in Fig. 6.41. Explicit form of the inputs and outputs, and the blocks used in Figs. 6.39-6.41 are explained clearly in previous sections (Sections 3.1, 5.2, 6.2). NN designed in this section is the same as the one used in Section 6.2. Only the inputs and the outputs are different.

$$\Delta \ddot{r} = \ddot{r}_d - \ddot{r} = [\Delta \ddot{\psi}_a \quad \Delta \ddot{\theta}_m]^T \quad (6.15)$$

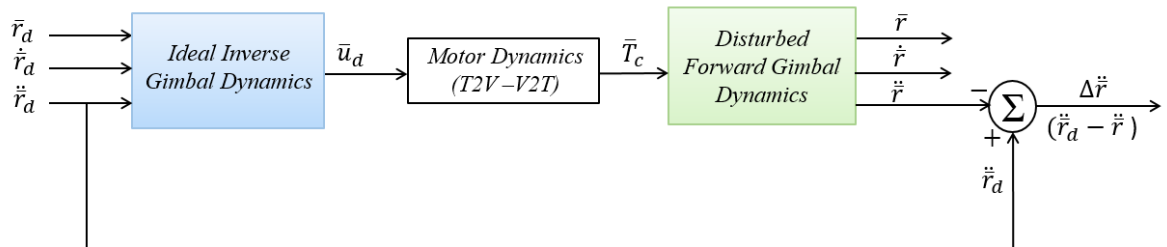


Figure 6.39: Training structure used in Simulink® for Method 3

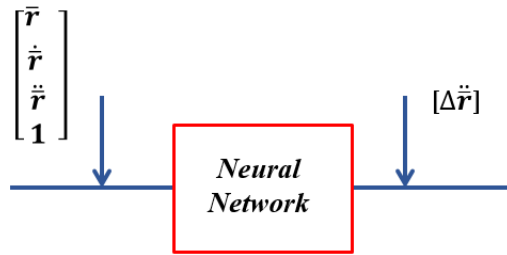


Figure 6.40: Input-output relationship of the NN used with Method 3

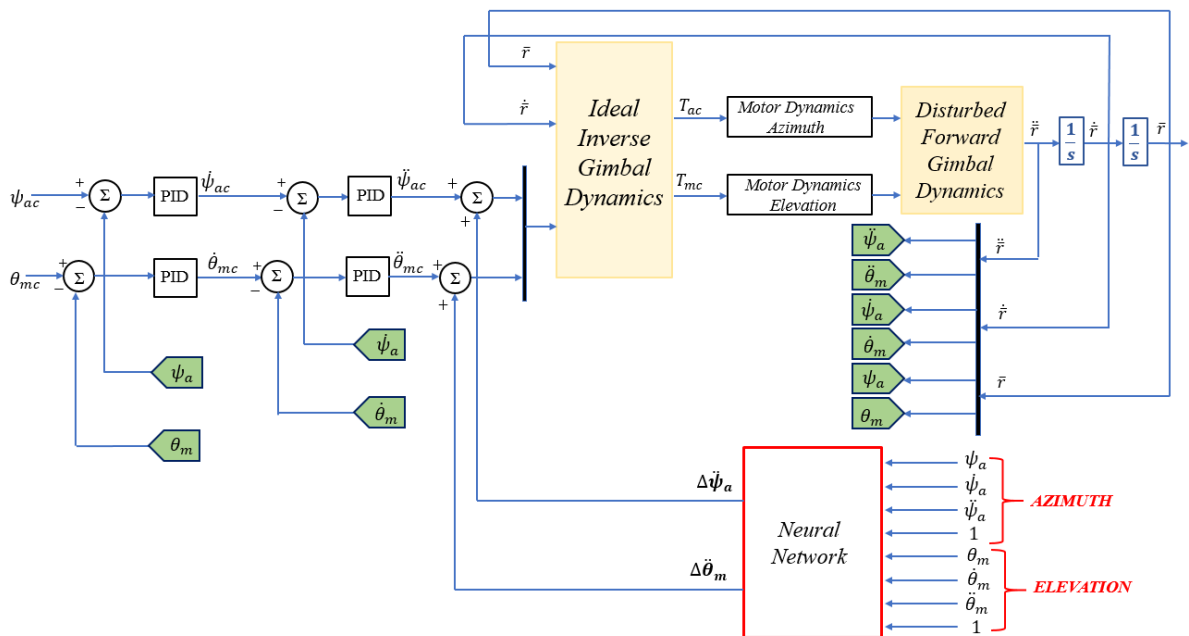


Figure 6.41: Block diagram implementation of the proposed NN in Simulink® (Method 3)

In the following examples, comparisons between cascaded PID controller and NN-based controller with Methods 2 and 3 are provided. Both in Methods 2 and 3, NN is trained with the training input given in Section 6.1, Fig. 6.4. Reference input sets used in this section are given in Table 6.11.

Table 6.11: Azimuth and elevation gimbal Reference Sets used in Section 6.5

	Azimuth Gimbal	Elevation Gimbal
<i>Reference Set 1</i>	5°@ 3Hz sine	5°@ 3Hz sine
<i>Reference Set 2</i>	1°@ 5Hz sine	1°@ 5Hz sine

Fig. 6.42, show the response of the controllers for the Reference Set 1 both for the azimuth and elevation gimbals. Results of Method 2 and 3 are so close to each other, especially for the elevation axis. Method 3 performs slightly better than Method 2 when it is trained with the training set given in Section 6.1. Different training inputs produce different results for the comparison between Method 2 and Method 3. The percentage decrease in mean tracking errors for Method 2 and 3 with respect to PID controller are given in Table 6.12.

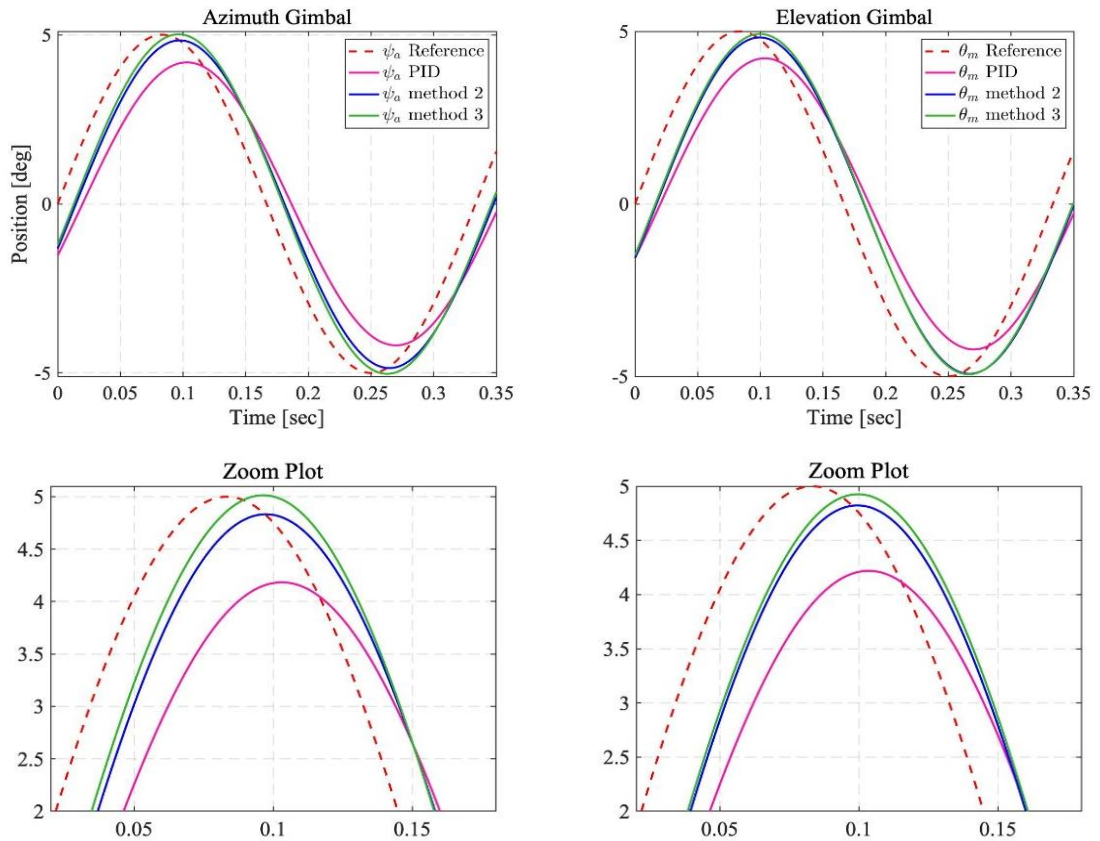


Figure 6.42: Response of the azimuth gimbal and elevation gimbals for Reference Set 1

Table 6.12: Mean track error improvement wrt. PID controller for Reference Set 1

	Percent Decrease (%)	
	Azimuth Gimbal	Elevation Gimbal
Method 2	28.27	18.43
Method 3	34.65	19.65

Fig. 6.43, shows that Method 3 increases bandwidth of the azimuth gimbal compared to cascaded PID controller (approximately by 5 times) for the Reference Set 2. Without NN based controller, PID controller reaches 0.96° around 1 Hz. Method 3 increases the bandwidth of the system slightly more compared to Method 2 (similar results are obtained as in Section 6.2).

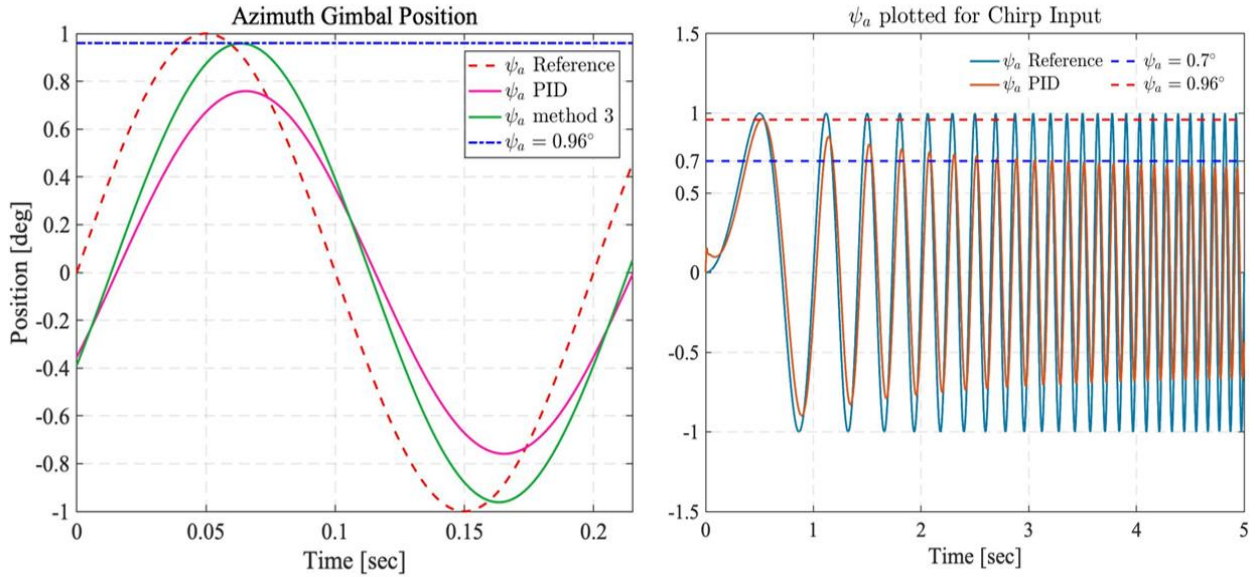


Figure 6.43: Response of the azimuth gimbal with PID and NN based controllers (Method 3) for the Reference Set 2

Chapter 7

Conclusion

In this thesis, first, a novel and fully detailed dynamical model for a two-axis gimbal system is proposed. Different from the existing articles regarding two-axis gimbal systems, EOMs of the system are derived using multi-body dynamics approach. Thus, mass, inertia and distance parameters are calculated from the 3D CAD model of the system by assuming inner and outer gimbals as separate rigid bodies. Mathematical model proposed in this study covers the misalignments between rotation axes of gimbals, the offsets between the CoG of the gimbals and the rotation axes, dynamical mass unbalance and the disturbances on the joints arising from friction or restraining elements of the whole gimbal system (such as cooling pipes and the cables of camera, encoders, motors, gyroscope). Thanks to Newton-Euler approach, the reaction forces and moments on the connection joints of the gimbal system are also expressed next, in detail. Translational motion is also considered with the rotational motion of the gimbal assembly. Most of these features do not appear in the literature, [1, 4, 6-20, 22-25].

After the derivation of the *Forward Dynamics* model, the *Inverse Dynamics* model is generated to estimate the complex, nonlinear, state and mechanism dependent disturbance torques present in the system. By using *Inverse Dynamics*, effects of the distance parameters, friction coefficients and cross-axis inertia terms (that are proposed in the mathematical model) on the dynamical behaviour of the system are investigated with MCSs.

Series of physical experiments are conducted to understand the behaviour of the overall disturbance torque and its dependency on system parameters and states. On the contrary of what is done in articles, [12, 13, 15], it is proven that disturbance torque present in each axis is a function of its own position and velocity, and it is somehow related to other gimbal's position and velocity. It is observed that, disturbance torque is composed of friction torque and disturbances resulting from the mechanism and linkages of the multi-axis gimbal system. They are also dependent on the model parameters (distances, mass and inertia terms).

A neural network is employed to approximate the complex nature of the disturbance torque present in the experimental set-up; because the cascaded PID controller is insufficient for compensation under the effects of complex disturbances, [2, 7, 8, 15, 18, 22, and 23]. The MLP structure supports and enhances the control performance of a previously designed cascaded PID controller by performing MIMO based compensation for the cross-coupled gimbal system. It improves the response of the system almost in the full operational range without requiring any tuning or adjustment (compared to ADRC, cascaded PID and inverse based controllers).

As a result of this study, we have reached a few important conclusions:

- Conventional controllers are very efficient and easy to implement in general. On the other hand, they may not be able to achieve sufficiently high

performance when dealing with complex systems, especially if there are unmodeled effects in the system or high disturbances. In all those cases, it is very useful to support a conventional controller by using a secondary controller such as a NN.

- Next, we have also observed that those secondary controllers usually fail in directly controlling even simple systems.
- Finally, and maybe most importantly, mathematical models of complex systems, will usually be impossible to express real physical phenomena exactly, affecting the real system. It is not very fruitful to try to develop “better” mathematical models (because it is usually impossible or too complex to be utilized in practice). A better idea in dealing with systems whose mathematical models are very complex should be to utilize simpler models with estimators (or observers) of the unmodeled dynamics which will appear in the form of disturbances (in addition to actual disturbances).

Original Contributions:

- The novel and fully detailed dynamical model is developed,
- *Inverse Dynamics* model is generated to estimate the complex, nonlinear, state and mechanism dependent (model parameters, i.e., distances, mass and inertia terms) disturbance torques present in the system,
- Three different MLP structures are proposed to support the control performance of the cascaded PID controller by performing MIMO based compensation for the cross-coupled gimbal system,
- *Inverse* and *Forward Gimbal Dynamics* of a two-axis gimbal system are used together both in the cascaded PID control and NN-based control structures,
- By using *Inverse* and *Forward Gimbal Dynamics* consecutively, a new procedure for collecting the training data of a NN is developed,
- Experiments on a physical set-up are performed for the proposed control structure with Method 2.

Future Work:

As a future study, physical experiments with base disturbance are planned to be performed. Another item is to control the physical system based on ADRC + ESO and compare the results with those what we have found already. In order to obtain a better mathematical model “important paramaters” will be identified by a system identification study based on open loop data from the real physiscal system using Inverse Dynamics. Online learning of the NN will be performed on the physical set-up. By that way, the proposed algorithm will work very well even for the time-varying disturbances. NN-based controller with Method 3 will be also implemented in the xPC Target as well. Finally, stability analysis of the NN based controller will be conducted, [40, 41].

BIBLIOGRAPHY

- [1] J.M. Hilkert, “Inertially Stabilized Platform Technology Concepts and Principles”, *IEEE Control Systems Magazine*, vol. 28, no. 1, pp. 26-46, 2008.
- [2] O. Hasturk, A.M. Erkmen, I. Erkmen “Proxy-Based Sliding Mode Stabilization of a Two-Axis Gimbaled Platform”, *Proceedings of the World Congress on Engineering and Computer Science*, vol. 1, pp. 370-376, 2011.
- [3] Z. Hurak and M. Rezac, “Image-based Pointing and Tracking for Inertially Stabilized Airborne Camera Platform”, *IEEE Transactions on Control Systems Technology*, vol. 20, no. 5, pp. 1146-1159, 2012.
- [4] M.M. Abdo, A.R. Vali, A.R. Toloiei, M.R. Arvan, “Research on the Cross-Coupling of a Two Axes Gimbal System with Dynamic Unbalance”, *International Journal of Advanced Robotic Systems*, vol. 10, no. 10, pp. 357-370, 2013.
- [5] X. Zhou, C. Yang, B. Zhao, L. Zhao and Z. Zhu, “A High- Precision Control Scheme Based on Active Disturbance Rejection Control for a Three-Axis Inertially Stabilized Platform for Aerial Remote Sensing Applications”, *Systems and Sensors in Geoscience Applications*, vol. 2018, pp. 1-9, 2018.
- [6] M.M. Abdo, A.R. Vali, A.R. Toloiei, M.R. Arvan, “Improving Two-Axes Gimbal Seeker Performance Using Cascade Control Approach”, *Journal of Aerospace Engineering*, vol. 229, no.1, pp. 38-55, 2015.
- [7] C. Bai, Z. Zhang, “A Least Mean Square Based Active Disturbance Rejection Control for an Inertially Stabilized Platform”, *Optik-International Journal for Light and Electron Optics*, vol. 174, pp. 609-622, 2018.
- [8] Y. Zou, X. Lei, “A Compound Control Method Based on the Adaptive Neural Network and Sliding Mode Control for Inertial Stable Platform”, *Neurocomputing*, vol. 155, pp. 286-294, 2015.

- [9] D.H Lee, D.Q. Tran, Y.B. Kim, S. Chakir “A Robust Double Active Control System Design for Disturbance Suppression of a Two-Axis Gimbal System”, *Electronics*, vol. 9, no. 10, 1638, 2020.
- [10] R. Jia, V.K. Nandikolla, G. Haggart, C. Volk, D. Tazartes, “System Performance of an Inertially Stabilized Gimbal Platform with Friction, Resonance and Vibration Effects”, *Journal of Nonlinear Dynamics*, vol. 95, no. 10, pp. 254-265, 2019.
- [11] Y. Wu, D. Yu, Z. Dong, “Robust Integral of Neural Network and Precision Motion Control of Electrical-Optical Gyro-Stabilized Platform with Unknown Input Dead-Zones”, *ISA Transactions*, vol. 95, pp. 254-265, 2019.
- [12] F. Yue, X. Lie, “Robust Adaptive Integral Backstepping Control for Opto-Electronic Tracking System Based on Modified LuGre Friction Model”, *ISA Transactions*, vol. 80, pp. 312-321, 2018.
- [13] X. Zhou, B. Zhao, W. Liu, H. Yue, R. Yu, Y. Zhao “A Compound Scheme on Parameters Identification and Adaptive Compensation of Nonlinear Friction Disturbance for the Aerial Inertially Stabilized Platform”, *ISA Transactions*, vol. 67, pp. 293-305, 2017.
- [14] J. Mao, J. Yang, W. Liu, S. Li, Q. Li, “Output Feedback Stabilization of Inertial Stabilized Platform with Unmatched Disturbances Using Sliding Mode Approach”, *IFAC-PapersOnLine*, vol. 50, no.1, pp. 5149-5154, 2017.
- [15] M. Zhang, H. Liu, H. Zhang, X. Miao, “A Hybrid Control Strategy for the Optoelectronic Stabilized Platform of a Seeker”, *Optik-International Journal for Light and Electron Optics*, vol. 181, pp. 1000-1012, 2019.
- [16] Y. Chen, H. Chu, T. Sun, L. Guo, F. Zhang, “Two-Axis Gimbal Platform Controller Design in Finite Time Application Occasions: LMI Approach”, *Optik*, vol. 158, pp. 831-841, 2018.

- [17] M.S. Sofla, M. Zareinejad, M. Parsa, H. Sheibani, "Integral Based Sliding Mode Stabilizing a Camera Platform Using Kalman Filter Attitude Estimation", *Mechatronics*, vol. 44, pp. 42-51, 2017.
- [18] M. Zhang, Y. Guan, W. Zhao, "Adaptive Super-twisting Sliding Mode Control for Stabilization Platform of Laser Seeker Based on Extended State Observer", *Optik-International Journal for Light and Electron Optics*, vol. 199, 163337, 2019.
- [19] A.K. Rue, "Precision Stabilization Systems", *IEEE Transactions on Aerospace and Electronic Systems*", vol. AES-10, no. 1, pp. 34-42, 1974.
- [20] B. Ekstrand, "Equations of Motion for a Two-Axes Gimbal System", *IEEE Transactions on Aerospace and Electronic Systems*", vol. 37, no.3, pp. 1083-1091, 2001.
- [21] MATLAB. (2020b), MathWorks. Accessed: September 22, 2020. [Online]. Available: <https://www.mathworks.com/products/matlab.html>
- [22] J. Mao, S.Li, Q. Li, J. Yang, "Design and Implementation of Continuous Finite-Time Sliding Mode Control for 2-DOF Inertially Stabilized Platform Subject to Multiple Disturbances", *ISA Transactions*, vol. 84, pp. 214-224, 2019.
- [23] F. Wang, R. Wang, E. Liu, W. Zhang, "Stabilization Control Method for Two-Axis Inertially Stabilized Platform Based on Active Disturbance Rejection Control with Noise Reduction Disturbance Observer", *IEEE Access*, vol. 7, pp. 99521-99529, 2019.
- [24] M. Baskin, K. Leblebicioglu, "Robust Control for Line-of-Stabilization of a Two-Axis Gimbal System", *Turkish Journal of Electrical Engineering & Computer Science*, vol. 25, no. 5, pp. 3839-3854, 2017.
- [25] B. Xiang, Q. Mu, "Gimbal Control of Inertially Stabilized Platform for Airborne Remote Sensing System based on Adaptive RBFNN Feedback Model", *IFAC Journal of Systems and Control*, vol. 16, no. 100148, 2021.

- [26] S. Wang, J. Xia, X. Wang, W. Yang, L. Wang, “Adaptive Neural Networks Control for MIMO Nonlinear Systems with Unmeasured States and Unmodeled Dynamics”, *Applied Mathematics and Computation*, vol. 408, article no. 126369, 2021.
- [27] M. Baskin, K. Leblebicioglu, “Combined System Identification and Robust Control of a Gimbal Platform”, *Turkish Journal of Electrical Engineering & Computer Science*, vol. 29, pp. 2247-2262, 2021.
- [28] O. Atesoglu, V. Nalbantoglu, B. Seymen, “Gyro-Bias Estimation Filter Design for the Stabilization Accuracy Enhancement of Two Axes Gimbaled Sighting Systems”, *IFAC Proceedings*, vol. 42, no. 2, pp. 5011-5017, 2016.
- [29] Simulink. (2020b), MathWorks. Accessed: September 22, 2020. [Online]. Available: <https://www.mathworks.com/products/simulink.html>
- [30] W. Schiehlen, “Multibody system dynamics: roots and perspectives”, *Multibody System Dynamics*, vol. 1, pp. 149-188, 2017.
- [31] P. Cui, D. Zhang, S. Yang, H. Li, “Friction Compensation Based on Time-Delay Control and Internal Model Control for a Gimbal System in Magnetically Suspended CMG”, *IEEE Transactions on Industrial Electronics*, vol. 64, no. 5, pp. 3798-3807, 2017.
- [32] K. A. J. Verbert, R. Toth, R. Babuska, “Adaptive Friction Compensation: A Globally Stable Approach”, *IEEE/ASME Transactions on Mechatronics*, vol. 21, no. 1, pp. 351-363, 2016.
- [33] C. Odabaş, Ö. Morgül, “Adaptive Friction Compensations for Mechanical Systems with Measurement Delay”, *Transactions of the Institute of Measurement and Control*, vol. 43, no. 8, pp. 1745-1759, 2021.
- [34] K. Guo, Y. Pang, H. Yu “Composite Learning Robot Control with Friction Compensation: A Neural Network-Based Approach”, *IEEE Transactions on Industrial Electronics*, vol. 66, no. 10, pp. 7841-7851, 2019.

- [35] J.Han “From PID to Active Disturbance Rejection Control”, *IEEE Transactions on Industrial Electronics*, vol. 56, no. 3, pp. 900-906, 2009.
- [36] Catia v5-3DX. (R2021), Dassault Systems. Available: <https://www.3ds.com/products-services/catia/products/>
- [37] J.A. Farrel, M. Polycarpou, M. Sharma, W. Dong, “Command Filtered Backstepping”, *IEEE Transactions on Automatic Control*, vol. 54, no. 6, pp. 1391-1395, 2009.
- [38] H.Z. Al Garni, A. Awasthi, “A Monte Carlo Approach Applied to Sensitivity Analysis of Criteria Impacts on Solar PV Site Selection”, in *Handbook of Probabilistic Models*, 1st ed., Oxford, UK: Butterworth-Heinemann, 2020, ch. 20, pp. 489-504.
- [39] A. Vickers, *What is p-value anyway? 34 Stories to Help You Actually Understand Statistics*, 1st ed. Boston: Addison-Wesley, 2010.
- [40] K. Tanaka, “An Approach to Stability Criteria of Neural-Network Control Systems”, *IEEE Transactions on Neural Networks*, vol. 7, no. 3, pp. 629-642, 1996.
- [41] Y. Fang, T.G Kincaid, “Stability Analysis of Dynamical Neural Networks”, *IEEE Transactions on Neural Networks*, vol. 7, no. 4, pp. 996-1006, 1996.

APPENDIX A

Table A.1: Elements of the cross-correlation matrix between \bar{d} and $\bar{\Delta}_{out}$

\ddots	a_{mx}	Ga_y	G_{ax}	G_{mz}	G_{mx}
T_a	-0.681	0.23	0.184	0.018	-0.631
T_e	-0.99	-0.045	0.1	0.088	0.032
F_{amx}	0.687	-0.118	-0.089	-0.21	0.697
F_{amy}	0.079	-0.12	0.147	-0.99	0.477
F_{amz}	-0.079	0.12	-0.147	0.99	-0.477
F_{abx}	-0.631	0.074	-0.25	0.25	-0.68
F_{aby}	-0.096	-0.425	-0.197	0.851	-0.321
F_{abz}	0.079	-0.12	0.147	-0.99	0.477
M_{amx}	0.079	-0.12	-0.147	-0.99	0.477
M_{amz}	0.688	-0.119	-0.087	-0.219	0.694
M_{abx}	-0.051	0.5	-0.081	0.9	-0.499
M_{aby}	-0.639	0.068	-0.245	0.2	-0.664

Table A.2: Elements of the p-value matrix between \bar{d} and $\bar{\Delta}_{out}$

$pval$	a_{mx}	Ga_y	Gax	Gmz	Gmx
T_a	5.9e-15	0.021	0.066	0.852	1.89e-12
T_e	1.58e-246	0.65	0.289	0.378	0.747
F_{amx}	2.89e-15	0.241	0.373	0.035	7.75e-16
F_{amy}	0.43	0.232	0.143	1.04e-85	5.07e-07
F_{amz}	0.43	0.232	0.143	1.04e-85	5.07e-07
F_{abx}	1.78e-12	0.46	0.012	0.009	6.86e-15
F_{aby}	0.337	1e-05	0.048	2.75e-29	0.001
F_{abz}	0.43	0.232	0.143	1.04e-85	5.07e-07
M_{amx}	0.43	0.232	0.143	1.04e-85	5.07e-07
M_{amz}	2.35e-15	0.235	0.389	0.027	1.1e-15
M_{abx}	0.61	1.05e-07	0.422	3.08e-37	1.21e-07
M_{aby}	8.26e-13	0.497	0.013	0.045	4.94e-14

Table A.3: Elements of the cross-correlation matrix between \bar{b} and $\bar{\Delta}_{out}$

\cdot	b_a	b_e
T_a	1	-0.036
T_e	-0.036	1
F_{amx}	-0.051	0.008
F_{amy}	0.051	-0.008
F_{amz}	0.051	-0.008
F_{abx}	0.051	-0.008
F_{aby}	-0.051	0.008
F_{abz}	-0.051	0.008
M_{amx}	-0.051	0.008
M_{amz}	-9.16e-18	2.15e-17
M_{abx}	0.051	-0.008
M_{aby}	-0.121	0.043

Table A.4: Elements of the p-value matrix between \bar{b} and $\bar{\Delta}_{out}$

<i>pval</i>	<i>b_a</i>	<i>b_e</i>
<i>T_a</i>	0	0.72
<i>T_e</i>	0.72	0
<i>F_{amx}</i>	0.6	0.93
<i>F_{amy}</i>	0.6	0.93
<i>F_{amz}</i>	0.6	0.93
<i>F_{abx}</i>	0.6	0.93
<i>F_{aby}</i>	0.6	0.93
<i>F_{abz}</i>	0.6	0.93
<i>M_{amx}</i>	0.6	0.93
<i>M_{amz}</i>	1	1
<i>M_{abx}</i>	0.6	0.93
<i>M_{aby}</i>	0.23	0.67

Table A.5: Elements of the cross-correlation matrix between \bar{j} and $\bar{\Delta}_{out}$

\ddots	J_{axy}	J_{axz}	J_{ayz}	J_{mxy}	J_{mxz}	J_{myz}
T_a	0.133	0.014	0.016	-0.226	-0.978	-0.078
T_e	-0.103	-0.018	-0.059	0.024	1	0.095
F_{amx}	-0.016	-0.058	0.12	0.093	0.077	0.006
F_{amy}	0.016	0.058	-0.12	-0.093	-0.077	-0.006
F_{amz}	0.016	0.058	-0.12	-0.093	-0.077	-0.006
F_{abx}	0.016	0.058	-0.12	-0.093	-0.077	-0.006
F_{aby}	-0.016	-0.058	0.12	0.093	0.077	0.006
F_{abz}	-0.016	-0.058	0.12	0.093	0.077	0.006
M_{amx}	-0.128	0.082	-0.059	-0.329	0.386	0.944
M_{amz}	-0.128	0.082	-0.059	-0.329	0.386	0.944
M_{abx}	0.212	-0.058	-0.775	0.046	-0.196	-0.587
M_{aby}	0.067	0.747	0.045	-0.015	-0.677	0.01

Table A.6: Elements of the p-value matrix between \bar{j} and $\bar{\Delta}_{out}$

<i>pval</i>	<i>J_{axy}</i>	<i>J_{axz}</i>	<i>J_{ayz}</i>	<i>J_{mxy}</i>	<i>J_{mxz}</i>	<i>J_{myz}</i>
<i>T_a</i>	0.184	0.887	0.871	0.023	2.89e-69	0.435
<i>T_e</i>	0.306	0.855	0.554	0.808	0	0.345
<i>F_{amx}</i>	0.87	0.563	0.232	0.356	0.441	0.951
<i>F_{amy}</i>	0.87	0.563	0.232	0.356	0.441	0.951
<i>F_{amz}</i>	0.87	0.563	0.232	0.356	0.441	0.951
<i>F_{abx}</i>	0.87	0.563	0.232	0.356	0.441	0.951
<i>F_{aby}</i>	0.87	0.563	0.232	0.356	0.441	0.951
<i>F_{abz}</i>	0.87	0.563	0.232	0.356	0.441	0.951
<i>M_{amx}</i>	0.203	0.414	0.555	0.0008	7.16e-05	3.91e-49
<i>M_{amz}</i>	0.203	0.414	0.555	0.0008	7.16e-05	3.91e-49
<i>M_{abx}</i>	0.033	0.562	4e-21	0.643	0.049	1.26e-10
<i>M_{aby}</i>	0.507	4e-19	0.655	0.88	9.7e-15	0.919

APPENDIX B

Table B.1: PID coefficient set 1

	<i>Tracking Loop Azimuth</i>	<i>Tracking Loop Elevation</i>	<i>Stabilization Loop Azimuth</i>	<i>Stabilization Loop Elevation</i>
K_p	100	80	20	20
K_i	1	1	1	1
K_d	1	1	1	1

Table B.2: PID coefficient set 2

	<i>Tracking Loop Azimuth</i>	<i>Tracking Loop Elevation</i>	<i>Stabilization Loop Azimuth</i>	<i>Stabilization Loop Elevation</i>
K_p	100	40	5	5
K_i	1	1	1	1
K_d	1	1	1	1

Table B.3: ADRC with ESO coefficients

	<i>Azimuth</i>	<i>Elevation</i>
r	60	60
k_1	350	300
k_2	40	30
β_{01}	500	500
β_{02}	5000000	5000000
β_{03}	1	1
b_0	0.12	0.15

Table B.4: PID coefficient set used in xPC Target for the Example 1

	<i>Tracking Loop Azimuth</i>	<i>Tracking Loop Elevation</i>	<i>Stabilization Loop Azimuth</i>	<i>Stabilization Loop Elevation</i>
<i>K_p</i>	10	10	20	20
<i>K_i</i>	10	20	10	10
<i>K_d</i>	1	1	0	0

Table B.5: PID coefficient set used in xPC Target for the Example 2

	<i>Tracking Loop Azimuth</i>	<i>Tracking Loop Elevation</i>	<i>Stabilization Loop Azimuth</i>	<i>Stabilization Loop Elevation</i>
<i>K_p</i>	20	25	20	20
<i>K_i</i>	10	40	10	10
<i>K_d</i>	0.5	1	0	0

APPENDIX C

Detailed explanation regarding Chapter 6, Section 6.5 is given here. Derivation of the idea behind Method 3 is provided below.

Let's assume that the structures of *Real* and *Model Plants* are given as in Figs. C.1 and C.2. *Real Plant* has the parameters J_1, b_1, k_1 and there is the disturbance torque T_d . *Model Plant* has the parameters J, b, k and it assumes that the disturbance torque T_d is equal to zero. $\ddot{\theta}, \ddot{\theta}'$ are the acceleration, $\dot{\theta}, \dot{\theta}'$ are the velocity and θ, θ' are the position.

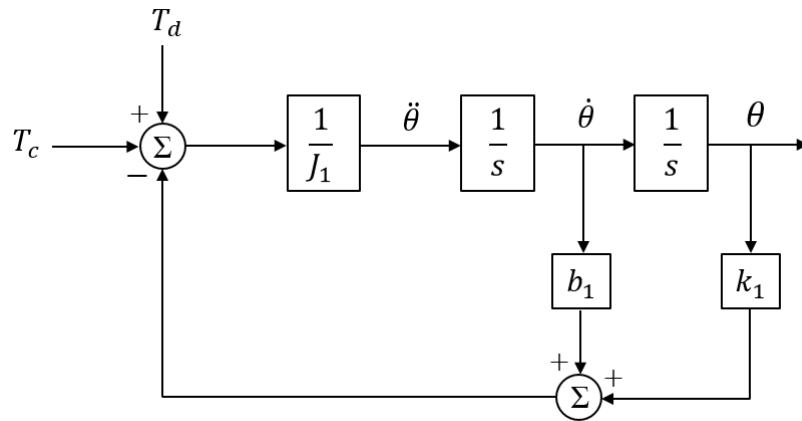


Figure C.1: Block diagram of the *Real Plant*

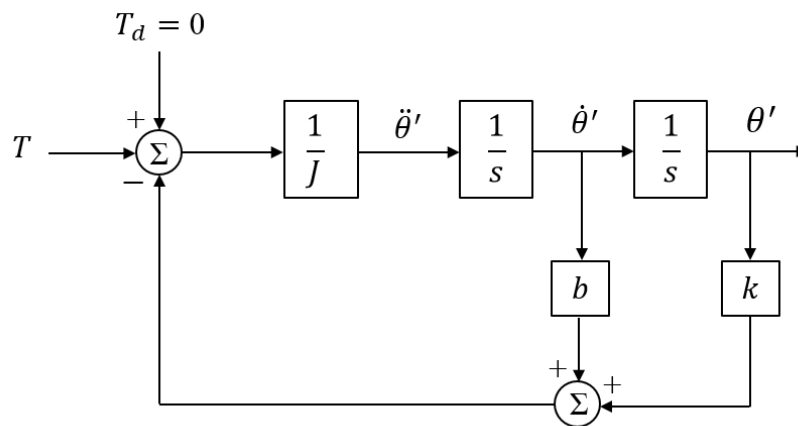


Figure C.2: Block diagram of the *Model Plant*

Open loop block diagram of the system composed of *Inverse Model Plant* and *Forward Real Plant* is given in Fig. C.3. It is similar to what is proposed in Chapter 3, Section 3.1, Fig. 3.2. As different from the Fig. 3.2, there is no motor dynamics block in between *Inverse* and *Forward Models* and the reference position and velocity are provided from the outputs of the *Real Plant*.

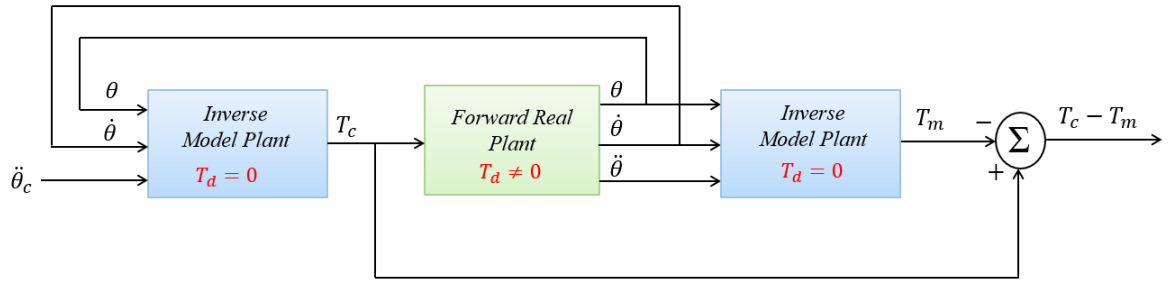


Figure C.3: Block diagram of the *Inverse Model Plant* and the *Forward Real Plant*

$\ddot{\theta}_c$ is the reference acceleration for the *Inverse Model Plant* and T_c is the output of the *Inverse Model Plant* (Eqn. C.1). $\ddot{\theta}$, $\dot{\theta}$ and θ are the outputs of the *Forward Real Plant*, they are used as the inputs of the second *Inverse Model Plant* block (Eqn. C.2).

$$T_c = J\ddot{\theta}_c + b\dot{\theta} + k\theta \quad (C.1)$$

$$T_c + T_d = J_1\ddot{\theta} + b_1\dot{\theta} + k_1\theta \quad (C.2)$$

By combining Eqns. C.1 and C.2 together, we end up with Eqn. C.3.

$$J\ddot{\theta}_c + b\dot{\theta} + k\theta = J_1\ddot{\theta} + b_1\dot{\theta} + k_1\theta - T_d \quad (C.3)$$

Eqn. C.4 is the slightly modified version of the Eqn. C.3.

$$J\ddot{\theta}_c - J\ddot{\theta} = (J_1 - J)\ddot{\theta} + (b_1 - b)\dot{\theta} + (k_1 - k)\theta - T_d \quad (\text{C.4})$$

T_m is the output of the second *Inverse Model Plant* (Eqn. C.5).

$$T_m = J\ddot{\theta} + b\dot{\theta} + k\theta \quad (\text{C.5})$$

For an ideal system with no disturbances present in the *Real Plant*, T_m should be equal to T_c . The difference between T_c and T_m is the disturbance torque that needs to be compensated and it is given in Eqn. C.6. The aim of Method 3 is to make T_m equal to T_c by providing the required compensation with acceleration.

$$T_c - T_m = J\ddot{\theta}_c - J\ddot{\theta} \quad (\text{C.6})$$

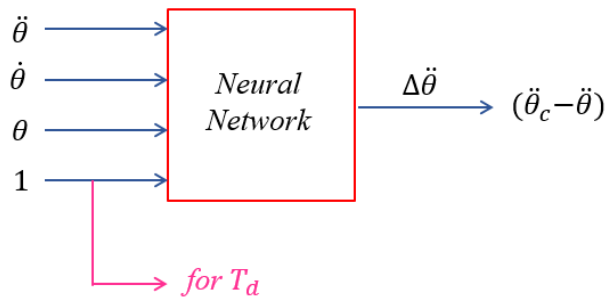
If we put Eqn. C.6 back in Eqn. C.4, we will end up with Eqn. C.7.

$$T_c - T_m = (J_1 - J)\ddot{\theta} + (b_1 - b)\dot{\theta} + (k_1 - k)\theta - T_d \quad (\text{C.7})$$

$$\ddot{\theta}_c - \ddot{\theta} = \Delta\ddot{\theta} = \frac{(J_1 - J)}{J}\ddot{\theta} + \frac{(b_1 - b)}{J}\dot{\theta} + \frac{(k_1 - k)}{J}\theta - \frac{T_d}{J}$$

Eqns. C.6 and C.7 show that the disturbance torque ($T_c - T_m$) is equal to acceleration difference. The following conclusion is reached: in order to eliminate the disturbance torque, we should first calculate $\ddot{\theta}_c - \ddot{\theta}$, for example, by using a NN having inputs, $\ddot{\theta}$, $\dot{\theta}$, θ , 1 and the output $\Delta\ddot{\theta}$. Next, by adding the output of the NN to $\ddot{\theta}$, the difference, $\ddot{\theta}_c - \ddot{\theta}$, can be forced to zero. The input-output relationship of the proposed NN structure is given in Fig. C.4.

Design a NN \Rightarrow



$$\Delta\ddot{\theta} = A\ddot{\theta} + B\dot{\theta} + C\theta + D$$

NN will approximate A, B, C, D

Figure C.4: Input-output relationship of the proposed NN

Another alternative for the NN structure that can be used in Method 3 is given in Fig. C.5.

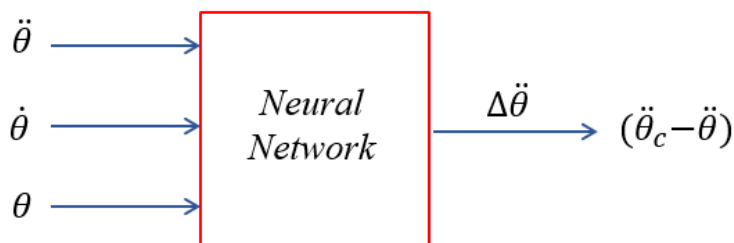


Figure C.5: Input-output relationship of the alternative NN

For the block diagram in Fig. C.2, suppose that the reference velocity and position for the *Inverse Model Plant* are provided directly as $\dot{\theta}_c$ and θ_c . We can propose two more NN structures for this situation as given in Fig. C.6. More possibilities can be integrated with Method 3 (i.e., with or without the constant 1 input).

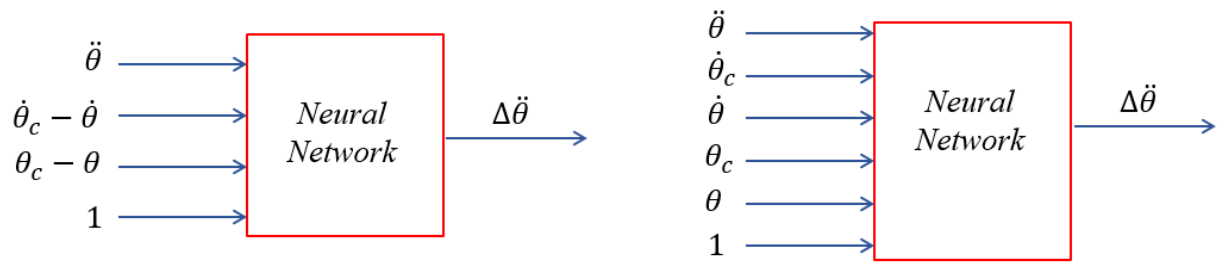


Figure C.6: NN alternatives with $\dot{\theta}_c$ and θ_c

Note that, while working with the physical system using xPC Target for the implementation of Method 3, it is important to use a reliable derivative operator to measure $\dot{\theta}$.